

# **MEMS BASED ULTRASONIC GAS SENSOR WITH UNIVERSAL SENSING CAPABILITY**

A THESIS SUBMITTED TO  
THE GRADUATE SCHOOL OF ENGINEERING AND SCIENCE  
OF BILKENT UNIVERSITY  
IN PARTIAL FULFILLMENT OF THE REQUIREMENTS FOR  
THE DEGREE OF  
MASTER OF SCIENCE  
IN  
ELECTRICAL AND ELECTRONICS ENGINEERING

By  
Derin Erkan  
September 2023

MEMS based ultrasonic gas sensor with universal sensing capability

By Derin Erkan

September 2023

We certify that we have read this thesis and that in our opinion it is fully adequate, in scope and in quality, as a thesis for the degree of Master of Science.

---

Erdiñç Tatar(Advisor)

---

Abdullah Atalar

---

Kıvanç Azgın

Approved for the Graduate School of Engineering and Science:

---

Orhan Arıkan  
Director of the Graduate School

## ABSTRACT

# MEMS BASED ULTRASONIC GAS SENSOR WITH UNIVERSAL SENSING CAPABILITY

Derin Erkan

M.S. in Electrical and Electronics Engineering

Advisor: Erding Tatar

September 2023

Gas sensors are a critical technology for life safety, process control, and most recently air quality measurements. Currently utilized gas sensing technologies need to be tailored to each specific gas, using either a chemically reactive substrate or an optical detector sensitive to certain gas types, providing very good selectivity at the expense of flexibility. In contrast, acoustic sensors promise a potentially universal method of gas sensing with lower selectivity, by measuring the speed of sound in a resonant cavity and inferring the gas content. In this work, a proof of concept for a MEMS based acoustic gas sensor is proposed. A horizontal cavity allows for a compact design, compared to vertical designs shown in the literature. Fabrication is simplified compared to existing CMUT/PMUT designs by using electrically tunable in-plane resonators as transducers. Fabrication of the designed sensor is carried out using an in-house developed SOI-MEMS process, while acoustic cavities are fabricated from silicon. During operation, one resonator excites the cavity while the other resonator measures the response. Frequency sweeps of the resonators while varying the tuning allows full characterization of device response. Overlaying sweeps at different tuning parameters reveals the cavity response, while testing with no cavity rules out parasitic effects. Both speed of sound and quality factor are observed, which can be used to improve selectivity in gas mixtures. The proof of concept device is tested in ambient air, measuring the speed of sound in air as 342 m/s, consistent with the literature and with external measurements.

*Keywords:* MEMS, acoustic resonance, acoustic coupling, gas sensors.

## ÖZET

# MEMS TABANLI EVRENSEL ÖLÇÜM KABİLİYETİNE SAHİP ULTRASONİK GAZ SENSÖRÜ

Derin Erkan

Elektrik Elektronik Mühendisliği, Yüksek Lisans

Tez Danışmanı: Erdinç Tatar

Eylül 2023

Gaz sensörleri can güvenliği, süreç denetimi ve hava kalitesi ölçümlerinde kilit bir teknolojidir. Günümüzde kullanılan sensör teknolojilerinin çoğu, belli bir gazı ölçmek için özel tasarlanmalıdır, örneğin kimyasal olarak aktif tabakalar veya belli gazları ölçebilen optik sensörler kullanılmaktadır. Bu sensörler esneklik pahasına çok iyi hassasiyet sağlamaktadır. Akustik sensörler ise daha düşük hassasiyette evrensel bir ölçüm tekniği vaat etmektedir. Bilinen bir oyukta rezonans kullanılarak ses hızı ölçülür ve gaz derişimi tahmin edilir. Bu çalışmada, MEMS tabanlı bir akustik gaz sensörü kavram kanıtlama aşamasında gösterilmektedir. Literatürdeki dikey oyuklara kıyasla daha az yer kaplayan yatay bir oyuk kullanılmıştır. Halihazırda var olan CMUT/PMUT teknolojisine nazaran çevirgeç olarak elektriksel olarak akort edilebilir ve düzlem içi titreşen rezonatörler tercih edilerek üretim sadeleştirilmiştir. Tasarlanan sensör özgün bir SOI-MEMS süreci kullanarak imal edilmiştir, akustik oyuk ise silisyumdan üretilmiştir. İşlev sırasında bir rezonatör oyuğu titreştirirken diğer rezonatör tepkiyi denetlemektedir. Rezonatörlerin akortmanı değiştirilirken frekans taraması yapılarak cihaz tepkisinin özellikleri saptanmıştır. Farklı rezonatör akortmanlarıyla alınan ölçümler üst üste yerleştirildiğinde oyuğun tepkisi görülebilmektedir. Oyuksuz yapılan testler ise parazitik etkilerin elenmesini sağlamaktadır. Cihazın uygunluğu hava içinde test edilmiştir. Literatürle ve dış ölçümlerle tutarlı bir şekilde havadaki ses hızı 342 m/s olarak ölçülmüştür. Kalite faktörünün de ölçülebilmesinin gaz karışımlarında hassasiyeti arttırabileceği öngörülmektedir.

*Anahtar sözcükler:* MEMS, akustik rezonans, akustik bağlaşım, gaz sensörleri.

## Acknowledgement

First of all, I would like to thank my advisor Erdinç Tatar for the opportunity that he has given me to study in this incredible field. It is thanks to his guidance and wisdom I now feel ready to continue my work as an engineer, expanding to new horizons in my career. I would further like to thank my thesis jury members Abdullah Atalar and Kıvanç Azgın for looking over my thesis in detail, giving me fresh insight on the work that I present here.

This project was supported by Marie Curie grant under the project "SmartGas". I am thankful for their aid, without which this project would be impossible to realize. Furthermore, I would like to thank everyone among the UNAM and Electrical and Electronics Department staff for their innumerable support to this thesis.

I am grateful to my friends at the Bilkent EEE graduate program, Baha Erim Uzunoglu, Can Soygür, Sadık Yağız Yetim, Tolga Veske, Ahmet Alp Derin and many more, who helped me in my lab work and also kept me sane during the hardest parts of my studies. I would also like to thank my closest friends, Barkın Kürümoğlu, Irmak Özdemir, Deniz Özdemir, Elif Aygün, Pelin Baysal, Evrim Mete, Sezin İsmailoğlu, and many more, for standing by my side all this time. Thank you to all of you from the bottom of my heart for calling me your friend. It is hard to overstate my gratitude to my parents, Boğaç and Tülay Özyurt Erkan, without their unending support it would be impossible for me to stand where I do today. They pushed me to do my best work and guided me through the toughest decisions in life. Thank you for everything, I hope to make you proud with each passing day throughout my life.

Finally, I dedicate this thesis to my grandfather, Hakkı Özyurt. He always believed in me from when I was a little baby to when I have become an engineer today. I miss him dearly and I hope that when he is watching all of us from above, that he is proud of what I have achieved.

# Contents

- 1 Introduction** **1**
  - 1.1 Motivation . . . . . 1
  - 1.2 Current Gas Sensing Technologies . . . . . 2
  - 1.3 Acoustic Gas Sensors . . . . . 5
  - 1.4 Proposed Acoustic Gas Sensor with In-Plane Resonators . . . . . 7
  - 1.5 Chapter Organization . . . . . 8
  
- 2 Theory of Operation** **9**
  - 2.1 Acoustic Cavity . . . . . 9
  - 2.2 Resonator Design . . . . . 12
    - 2.2.1 Mechanical Properties . . . . . 12
    - 2.2.2 Drive Electrodes . . . . . 17
    - 2.2.3 Sense Electrodes . . . . . 19
    - 2.2.4 Tuning Electrodes . . . . . 21

- 2.3 Overall Sensor . . . . . 28
  
- 3 MEMS Fabrication 31**

  - 3.1 Sensor Die . . . . . 32
    - 3.1.1 Metal Layer . . . . . 32
    - 3.1.2 Device Layer . . . . . 33
    - 3.1.3 Die Release . . . . . 38
  - 3.2 Cavity . . . . . 43
  - 3.3 Post-fabrication processing . . . . . 49

  
- 4 Experimental Procedure 51**

  - 4.1 Frontend Electronics . . . . . 54
    - 4.1.1 Signal Switches . . . . . 56
    - 4.1.2 Differential Buffer . . . . . 57
    - 4.1.3 Sense Amplifier . . . . . 58
    - 4.1.4 Instrumentation Amplifier . . . . . 60
  - 4.2 Experiment Procedure . . . . . 61

  
- 5 Experimental Results 65**

  - 5.1 Results . . . . . 65
    - 5.1.1 N4P1 . . . . . 68

5.2 N1N1 . . . . . 75

5.3 Conclusion . . . . . 81

5.4 Future Work . . . . . 81

**A DRIE Process Parameters 88**

**B Acoustic Cavity Resist Coating Procedure 89**

**C Family of Curves Code 90**

# List of Figures

1.1	Diagram of non-dispersive infrared sensor operation. The target gas has an absorptive peak in the infrared range. As the gas concentration increases, less infrared light can be transmitted between source and detector. . . . .	3
1.2	Diagram of gas sensor using gas sensitive material. Target gas molecules interact chemically with the active material, causing either a current or voltage to be generated, or a change in substrate resistance. All of these can be detected with the readout electronics.	4
1.3	Acoustic gas sensor with a spherical cavity [1]. The source excites the cavity with ultrasound and the detector measures the amplitude within the cavity. The resonant mode is highlighted using green arrows. . . . .	6
1.4	Diagram of CMUT based gas sensor [2]. Acoustic resonant mode is highlighted using green arrows. . . . .	7
1.5	Diagram showing high level view of acoustic gas sensor system. .	7
2.1	Diagram of acoustic cavity showing relevant dimensions. Resonant mode is highlighted in green. . . . .	10

2.2	Side view of the cavity showing the direction of resonance. Particle velocity within the cavity in $L_x$ direction is shown at resonance. . . . .	12
2.3	A broad overview of a single acoustic resonator, showing the moving structure and each electrode that acts upon it. Only one half of the resonator is shown, the structure is symmetrical along the line A-A'. The proof mass vibrates vertically. . . . .	13
2.4	Close-up of a single suspension element, showing the measurements of each beam within the element. . . . .	14
2.5	FEM output of eigenfrequency simulation. One half of symmetric resonator is shown, while displacement is exaggerated for visual clarity. . . . .	16
2.6	Close-up of resonator showing drive electrodes on either side. Fingers on the drive electrode mesh with fingers on the proof mass. . . . .	17
2.7	Diagram of comb drive actuators showing direction of travel and relevant dimensions. . . . .	18
2.8	Close-up of resonator showing the center section, where sense electrodes are placed. . . . .	19
2.9	Close-up of parallel plate resonator showing sense actuator. Only half of the actuator is shown, the device is symmetrical along the line A-A'. . . . .	20
2.10	Diagram of parallel plate electrodes . . . . .	20
2.11	Close up of parallel plate resonator showing tuning electrodes. . . . .	21
2.12	Close up of comb drive resonator showing tuning electrodes. . . . .	22
2.13	Diagram of length tapered comb actuator showing the relevant dimensions and the tapering effect. . . . .	23

2.14 Finite element model of length tapered comb tuning electrodes, showing the electric potential within the space. . . . . 25

2.15 Capacitance of one set of tapered combs with respect to displacement, calculated using FEA. . . . . 25

2.16 Change in capacitance with respect to displacement of tapered combs, calculated using FEA. . . . . 25

2.17 Finite element model of parallel plate tuning electrodes, showing the electric potential within the space. . . . . 26

2.18 Capacitance of one set of parallel plates with respect to displacement, calculated using FEA. . . . . 27

2.19 Change in capacitance with respect to displacement of tapered combs, calculated using FEA. . . . . 27

2.20 Diagram of sensor system. . . . . 28

2.21 Diagram of transducers on sensor die showing physical layout. . . 29

3.1 Diagram showing the general steps to the fabrication procedure. . . 31

3.2 Wafer after gold coating . . . . . 33

3.3 Example of dummy wafer used to test DRIE. Although etch depth is close to being acceptable, especially in narrower trenches the sidewall profile is clearly getting distorted by the etch process. It is likely that the accelerated ions striking the bottom of the trench are being deflected back and striking the sidewalls as the trench gets deeper. . . . . 35

3.4 Example of dummy wafer used to test DRIE. As with Figure 3.3, the sidewall is sloping outwards, adversely affecting the thinner suspension and proof mass. . . . . 36

3.5 Example of dummy wafer used to test DRIE. Sidewall profile is not parallel, although there is some improvement. The changes made to the etch recipe to improve sidewall profile have slowed down the process, causing the trenches to be etched less than what is needed. Even with an 15 $\mu$ m wafer, it is clear that the bottom will not always be reached. . . . . 36

3.6 Optical microscope photo of dummy wafer, zoomed in on test structures. The number indicates the width of each trench in  $\mu$ m. 37

3.7 SEM image of dummy wafer, showing cross section of etched features. 37

3.8 Underside of a proof mass showing remnants of sacrificial oxide from the release etch process. . . . . 39

3.9 Portion of the final device die shown under SEM. . . . . 41

3.10 Optical microscope photo of sensor die. . . . . 42

3.11 CAD model of 3D printed cavities showing a range of inner dimensions . . . . . 44

3.12 First iteration of 3D printed cavities with large handle on back side 44

3.13 Second iteration of 3D printed cavities, printed directly with no support structures . . . . . 44

3.14 Single silicon cavity viewed through an optical microscope. . . . . 45

3.15 Wafer of silicon cavities after dicing. . . . . 46

3.16 Benefit of offset cavities on selection of resonators within the sensor die. . . . . 47

3.17 Probe station test setup showing Keithley 2400 SMU being used to test for shorts. . . . . 49

3.18 Readout board which is used with the probe station. . . . . 50

4.1 High-level diagram of experiment setup. . . . . 52

4.2 3D render of unpopulated gas sensor daughterboard. . . . . 53

4.3 Completed sensor dice ready for testing. . . . . 53

4.4 Close-up photo of PCB showing daughterboard attached on top. . 55

4.5 Photo of overall test setup including test PCB. . . . . 55

4.6 High-level schematic of single resonator with associated readout electronics. . . . . 56

4.7 Schematic of multiplexing switches, showing signal connections to source and detector transducers. Tune voltage connections are made directly and not shown here. . . . . 57

4.8 Schematic of differential buffer amplifier. . . . . 57

4.9 Schematic of sense amplifier showing both resistive and capacitive feedback. Circuit topology changes based on which component dominates the resulting impedance. . . . . 58

4.10 Schematic of sense amplifier with noise sources highlighted. . . . . 59

4.11 Schematic of instrumentation amplifier circuit. . . . . 61

4.12 Tuning path showing the voltage applied to each resonator with respect to ground. . . . . 63

4.13 Arduino based speed of sound measurement setup. . . . . 64

5.1 Example sweep result from die N4P1 showing an uncompensated result as well as the electrical feedthrough that is measured separately. . . . . 67

5.2 Sweep result from die N4P1 with electrical feedthrough subtracted. 67

5.3 Tuning curve of N4P1 resonators, showing the . . . . . 68

5.4 Individual frequency response of both resonators at the point of maximum coupling . . . . . 69

5.5 Overlaid plots of detector response while source tuning is varied shows coupling in more detail. . . . . 70

5.6 Response of detector resonator with source driven, with and without the acoustic cavity. . . . . 70

5.7 Excerpt of family of curves for N4P1 with no acoustic cavity. . . . 72

5.8 Excerpt of family of curves for N4P1 with acoustic cavity attached. 72

5.9 Heatmaps of N4P1 response. . . . . 72

5.10 Family of curves showing full tuning range and uncapped response. 73

5.11 Family of curves showing full tuning range and capped response. . 74

5.12 Diagram of N1N1 die showing the two resonator types. . . . . 75

5.13 Tuning curve of N1N1’s source transducer showing cavity selection. 76

5.14	Excerpt of measured response with no acoustic cavity. . . . .	76
5.15	Excerpt of measured response with acoustic cavity. . . . .	77
5.16	Inferred tuning curves for both resonators within N1N1. . . . .	77
5.17	Heatmap of peak detector amplitudes within N1N1. . . . .	78
5.18	Inferred acoustic cavity frequency response based on N1N1 response.	79
5.19	Family of curves showing full tuning range and capped response. .	80

# List of Tables

2.1	Table of adiabatic indices and molecular mass for selected gases. . . . .	11
2.2	Spring constants and theoretical beam lengths for each target resonant frequency. . . . .	15
2.3	Table of selected resonant frequencies for each sensor die. . . . .	29
3.1	Fabricated cavity dimensions and corresponding resonant frequencies at $c_{gas} = 345\text{m/s}$ . . . . .	48
4.1	Calculation of notable noise sources within sense amplifier circuit. . . . .	60
A.1	Process parameters used in the DRIE processing step . . . . .	88

# Chapter 1

## Introduction

### 1.1 Motivation

The first gas sensor, the proverbial "canary in the coal mine" was discovered in the 19th century. In coal mines, harmful gases seep through walls, causing explosions or poisoning miners, at concentrations lower than that which could be detected by smell alone. The response was to bring canaries in cages down the mine shafts. These birds, being more sensitive to these gases, would faint before conditions became deadly, allowing the miners to take the necessary precautions. After using canaries, the next innovation came in the form of the Davy lamp. This lamp was not only safe in flammable atmospheres, but it was also a rudimentary gas detector. When calibrated in a well-ventilated environment, the height of the flame could indicate the presence of methane (the flame would be longer) or oxygen (shorter). Many lamps of this type being manufactured with graduated scales to measure the flame height mean that they can be considered the first man-made gas sensor [3].

During most of the 20th century, various electrical gas sensing technologies, as well as other chemical gas detectors were developed and commercialized. During this time, the primary application for gas sensing was for safety. A significant

amount of gas sensors were designed to detect harmful gases, like  $H_2S$ , methane, or carbon monoxide. These sensors require high selectivity and sensitivity to be usable in a safety context. However, in the 21st century, in particular following the wake of the COVID-19 pandemic, environmental monitoring has also become an important application of gas sensors [4]. These sensors are intended to measure low concentrations of gases such as carbon dioxide and volatile organic compounds (VOC), which are not directly harmful to human health. However, they provide a quantitative indication of air quality and the need for ventilation, especially within indoor spaces. Combined with Internet of Things based sensor networks, a new emphasis is placed on lower cost sensors, where the previous desire for reliability to ensure safety has been supplanted with a desire to place as many sensors as possible, with greater tolerance on each individual sensor's performance. The acoustic gas sensor technology presented in this thesis is a significant step in this direction, with the proposed technology providing a versatile and easily fabricated method of gas sensing.

## 1.2 Current Gas Sensing Technologies

Commercially utilized gas sensors can generally be divided into two categories. The first category is optical sensing, where the gas is passed into a chamber with a light source and detector contained within. The most common type of sensor in this category is non-dispersive infrared (NDIR), shown in Figure 1.1. The infrared source can be either a laser, or a broadband source such as an incandescent light bulb. For this type of gas sensor, typically 2 to  $20\mu\text{m}$  band is used [5]. As the gas concentration in the chamber changes, this absorption spectrum of the gas will cause a change in the amount of light that makes it to the detector. This way, the gas concentration can be measured.

This type of gas sensor is notable for very good selectivity and sensitivity, and it is not readily affected by humidity or temperature changes in the environment, as the absorption spectra of gases is not affected significantly by temperature, and water vapor is not especially absorptive in infrared. Typically, NDIR method is

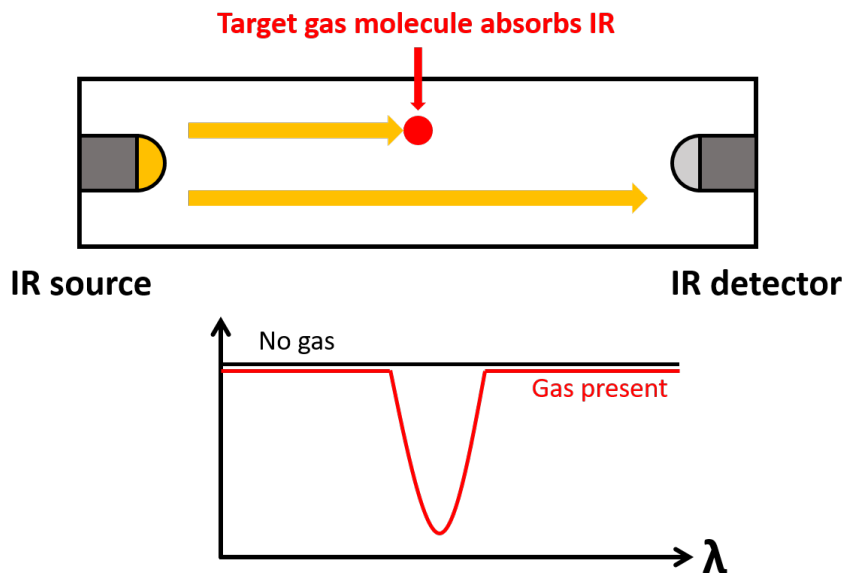


Figure 1.1: Diagram of non-dispersive infrared sensor operation. The target gas has an absorptive peak in the infrared range. As the gas concentration increases, less infrared light can be transmitted between source and detector.

used to measure concentration of gases such as  $CO_2$  and methane [5] [6]. For other gases such as  $NO_x$ , ultraviolet sources can also be used instead of infrared. The gases which can be measured by this technique have the common property of fluorescing under infrared, which can be detected with a photomultiplier tube.

The other category of gas sensor that is commercially utilized is reliant on gas sensitive materials interacting with the gas directly, shown in Figure 1.2 In this category, there are a large number of technologies being used. Generally, the unknown gas is allowed to flow over a substrate made of the gas sensitive material. When molecules of the desired gas type are present, these molecules cause a chemical reaction with the substrate. This then causes some electrical property of the substrate to change: some voltage or potential can be generated, or the resistance of the substrate may change. With an appropriate readout circuit, this often minuscule change is detected and turned into a measurement of the target gas.

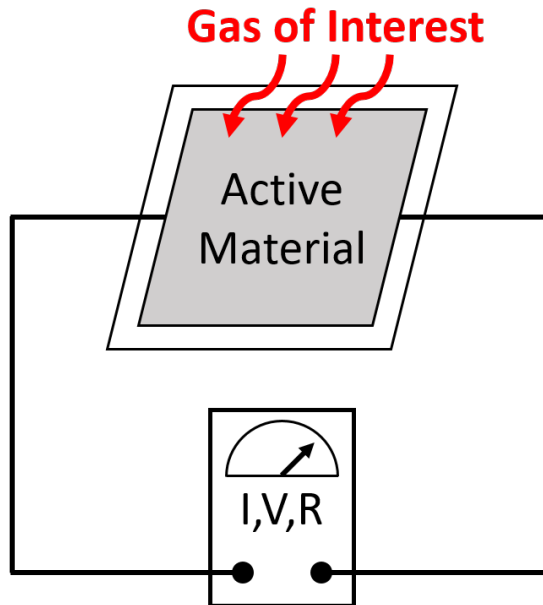


Figure 1.2: Diagram of gas sensor using gas sensitive material. Target gas molecules interact chemically with the active material, causing either a current or voltage to be generated, or a change in substrate resistance. All of these can be detected with the readout electronics.

Some examples of sensitive material based gas sensors include metal oxide semiconductor based sensors, solid electrolyte based sensors, and catalytic sensors [7]. Semiconductor gas sensors rely on a metal oxide crystal such as  $SnO_2$ , into which gas particles can diffuse. The effect is modelled as a double Schottky barrier which causes a varying resistance with gas concentration. Solid electrolyte gas sensors and catalytic sensors both operate by entering a chemical reaction with the gas being measured, and measuring a resulting potential difference due to ionic behavior [8] [9]. Solid electrolyte sensors are typically used to measure oxygen concentration, while catalytic sensors can be used to measure hydrocarbon and volatile organic compound (VOC) concentrations. Furthermore, many of these sensors have also been miniaturized using MEMS techniques in the literature, depositing the gas sensitive material onto a smaller substrate [10] [11] [12].

## 1.3 Acoustic Gas Sensors

Another category of gas sensor that is encountered is the acoustic gas sensor. This type of sensor generally relies on an acoustic cavity fitted with an acoustic source, typically ultrasonic, and a matching detector. By driving the cavity to resonance and measuring the properties of the resonance, an inference can be made as to the type of gas within the cavity. This type also includes the sensor which is presented in this thesis, and further details on the overall mode of operation are given in Chapter 2.

One area where acoustic gas sensors are utilized is for precise measurement of gas mixtures for calibration of other sensor types. The nature of acoustic sensing means that the measurement is dependent on only the properties of the gas and the cavity dimensions, which allows for a high precision if the cavity dimensions can be controlled accurately. Such a sensor is encountered in [1], developed by the National Bureau of Standards (now NIST), shown in Figure 1.3. This sensor is implemented as a 12.7mm diameter sphere made of steel, with openings for transducers and a gas vent, and the resonant mode is shown to have very high Q between 2000 and 10000. In addition, the spherical shape allows an accurate analytical model of the resonance to be calculated, including the disturbances introduced by the non-ideal ports. By using this precise geometry, the speed of sound within the gas is shown to be measurable to 0.02% error, however it is suggested that improvement of the fabrication process can reduce this figure to 0.0005% error [1]. Another similar device is demonstrated in [13], referred to as a Greenspan viscometer [14] [15], which is implemented using two cylindrical cavities coupled by a high aspect ratio tube. By designing the geometry to isolate the fundamental resonant mode from other modes, a high accuracy measurement can be made. Here a 0.03% error is found for speed of sound, and a further measurement of gas viscosity is shown with a maximum error of 0.5% [16].

The next area of innovation for acoustic gas sensors has been, as with many other sensor technologies, miniaturization. MEMS technology allows for smaller cavities and transducers to be fabricated, which allow these sensors to satisfy

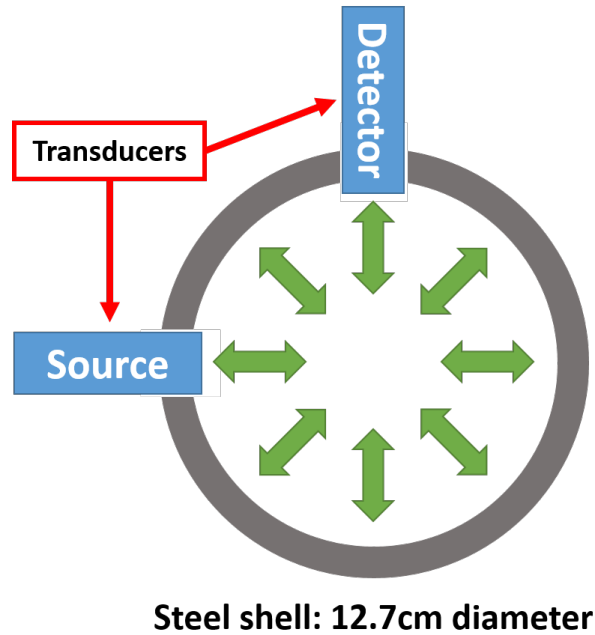


Figure 1.3: Acoustic gas sensor with a spherical cavity [1]. The source excites the cavity with ultrasound and the detector measures the amplitude within the cavity. The resonant mode is highlighted using green arrows.

niche applications where the physically large examples have previously been unsuitable. In fact, beyond simply miniaturizing large scale acoustic sensors, MEMS based sensors can also displace other sensor technologies like the optical sensors mentioned in Section 1.2. One method of using MEMS to detect gases is an adsorptive sensor. This involves a MEMS structure that is coated with a chemically active compound. When this structure is driven to its mechanical resonance, its mass will vary based on gas adsorption into the chemically active coating. Measuring the resonant frequency gives the mass adsorbed into the substrate [17] [18] [19]. By selecting an appropriate coating, highly selective sensors are achievable. [20]

Another acoustic sensor relies on a MEMS cavity, using a CMUT array as a combined sensor and detector, shown in [2][21]. A diagram of this sensor is shown in Figure 1.4. The cavity is excited vertically and the resonance frequency is measured by plotting the electrical impedance of the CMUT array with respect to frequency, which is related to the acoustic impedance of the cavity. This

technique demonstrates an ability to detect  $CO_2$  concentrations to within 10-20 ppm [2], as well as highlighting some areas for improvement, i.e humidity and temperature sensitivity which can be compensated externally.

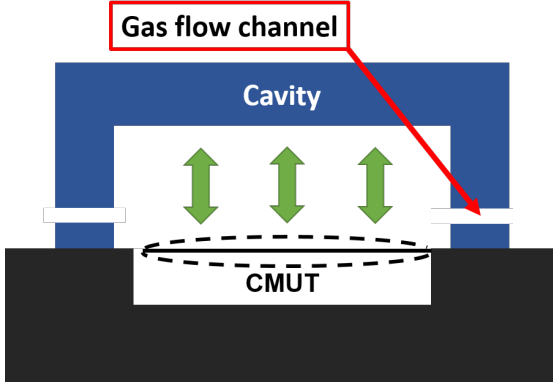


Figure 1.4: Diagram of CMUT based gas sensor [2]. Acoustic resonant mode is highlighted using green arrows.

### 1.4 Proposed Acoustic Gas Sensor with In-Plane Resonators

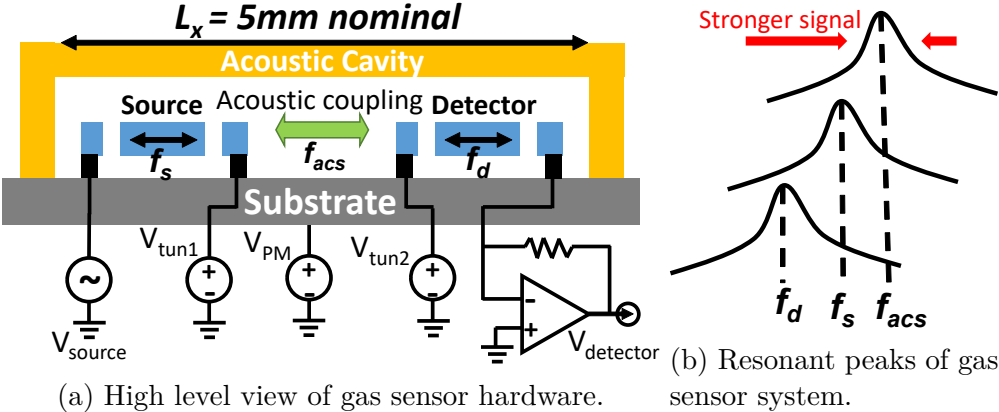


Figure 1.5: Diagram showing high level view of acoustic gas sensor system.

In this thesis, an acoustic gas sensor implemented using MEMS in-plane resonators is envisioned. Compared to the fabrication of CMUT cells [22], in-plane resonators are simpler to fabricate. The details of this sensor’s operation are explored in Chapter 2, however Figure 1.5 shows a superficial overview of the sensor

system. Two resonators are used within the acoustic cavity, with one acting as a source and the other acting as a detector. The cavity's horizontal resonant mode, highlighted with a green arrow, is driven by the source resonator while the mechanical resonant frequency is adjusted through a DC tuning voltage. The detector resonator is used to pick up the signal in the acoustic cavity, and another DC tuning voltage adjusts its mechanical resonant frequency. When all three resonant frequencies match, as shown in Figure 1.5b, the highest signal amplitude is observed. From this observation, the cavity's acoustic resonant frequency  $f_{acs}$  is determined and the gas concentration can be calculated.

## 1.5 Chapter Organization

This thesis includes the design of the sensor elements, as well as fabrication of a proof-of-concept device and testing carried out in order to verify the viability of the proposed architecture. In Chapter 2, the operation of the proposed sensor is described in detail. Analytical expressions for the in-plane resonators and the acoustic cavity response are given, and finite element simulations verify the mechanical movement of the resonators. Chapter 3 describes the fabrication process which is developed in house at Bilkent UNAM facilities. The setup for the experimentation process is shown in Chapter 4. Finally, in Chapter 5, experimental results are given and an overall summary is presented.

# Chapter 2

## Theory of Operation

The gas sensor system consists of an acoustic cavity with known dimensions, and two resonators which weakly interact with this acoustic cavity. In this chapter, the properties of the acoustic cavity, as well as the mechanical properties of the resonators are described. In addition, the electrical properties of the actuators used on the resonators are also shown.

### 2.1 Acoustic Cavity

The acoustic cavity is effectively the sensing element of the system. This cavity is driven to resonance by an acoustic transducer in order to measure its resonant frequency, which gives information about the gas contained within. A rectangular acoustic cavity is designed in order to match the rectangular shape of the sensor die. The fabricated structure forms all but one walls of the cavity and the final wall is formed by the surface of the sensor die in the assembled sensor. The resonant frequency of a rectangular cavity is given by Equation 2.1 [23]:

$$f_{lmn} = \frac{c_{gas}}{2} \sqrt{(l/L_x)^2 + (m/L_y)^2 + (n/L_z)^2} \quad (2.1)$$

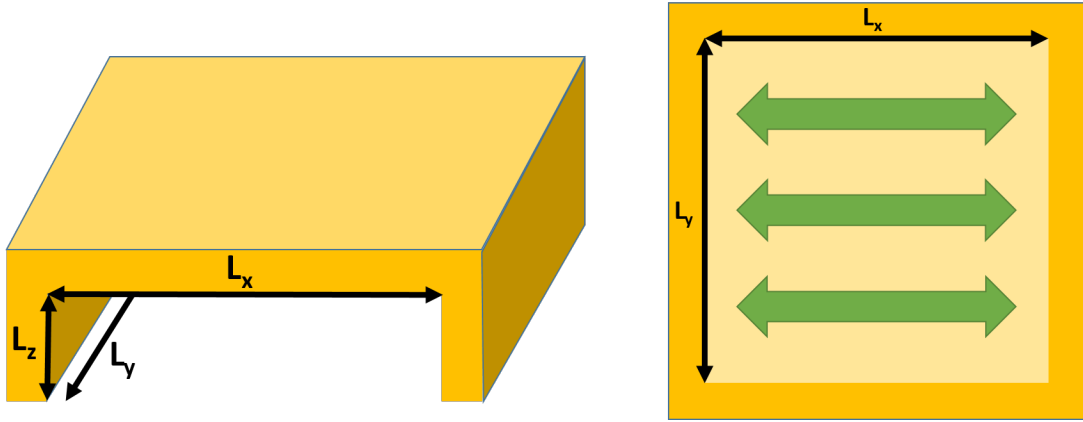


Figure 2.1: Diagram of acoustic cavity showing relevant dimensions. Resonant mode is highlighted in green.

where  $L_x$ ,  $L_y$ ,  $L_z$  represent the cavity dimensions, shown in Figure 2.1 and  $l, m, n$  are positive integers. The speed of sound  $c_{gas}$  is further given by 2.2

$$c_{gas} = \sqrt{\frac{\gamma \cdot k \cdot T}{m}} \quad (2.2)$$

where  $\gamma$  is the adiabatic index of the gas inside the cavity,  $k$  is Boltzmann's constant,  $T$  is the temperature in Kelvin, and  $m$  is the mean molecular mass of gas particles in kilograms. The adiabatic index, also called the specific heat ratio, takes on a unique value for each gas. Some typical values for adiabatic index and molecular mass are given in Table 2.1 [24], with all values measured at 300 K.

It is also important to note that  $c_{gas}$  does not show any dependence with pressure. At very high or very low pressures, the speed of sound changes as the adiabatic index shifts or the gas exits its viscous flow regime. However, at pressures close to atmospheric pressure, the acoustic resonance remains unaffected by pressure. As pressure increases, the gas density increases, but the bulk modulus (equivalent to spring constant) also increases, canceling each other out.

Table 2.1: Table of adiabatic indices and molecular mass for selected gases.

Gas	Adiabatic Index	Molecular Mass (g/mol)
Air	1.4	28.966 [24]
Argon	1.67	39.948
Carbon Dioxide	1.27	44.009
Nitrogen	1.4	28.014

Due to the difference in adiabatic index and mean molecular mass, a change in gas concentration within the cavity will also cause a shift in the resonant frequency of the acoustic cavity. While designing the device, air at a temperature of 300K is assumed, for which a  $c_{gas}$  of 345 m/s can be calculated. For simplicity of the design, the  $l, m, n = 1, 0, 0$  resonant mode (first longitudinal mode [23]) is selected. The wave shape of this mode is shown in Figure 2.2. The wave front travels longitudinally through the cavity, parallel to the resonators underneath. In addition to the in-plane structure of the resonators, this ensures that the resonant frequency is determined mainly by the distance between the side walls of the cavity, which means that variations in the depth of the cavity and the shape of the resonators will disturb the resonant mode as little as possible.

Based on the previously made assumptions regarding gas content and temperature, the cavity dimensions were selected as 5 mm length and 5mm width which gives an approximate resonant frequency of 34 kHz. This frequency and dimension was selected in order to increase the tuning range of the MEMS resonators as described in Section 2.2. During fabrication, a number of different sized cavities with constant widths of 5 mm and varying lengths between 3.9 mm and 5 mm are also planned in order to account for process variations affecting the resonators. The cavity width is held constant to avoid touching the moving structure within the die. The cavity depth is not determined as a critical dimension, however an approximate depth of  $100\mu\text{m}$  is targeted.

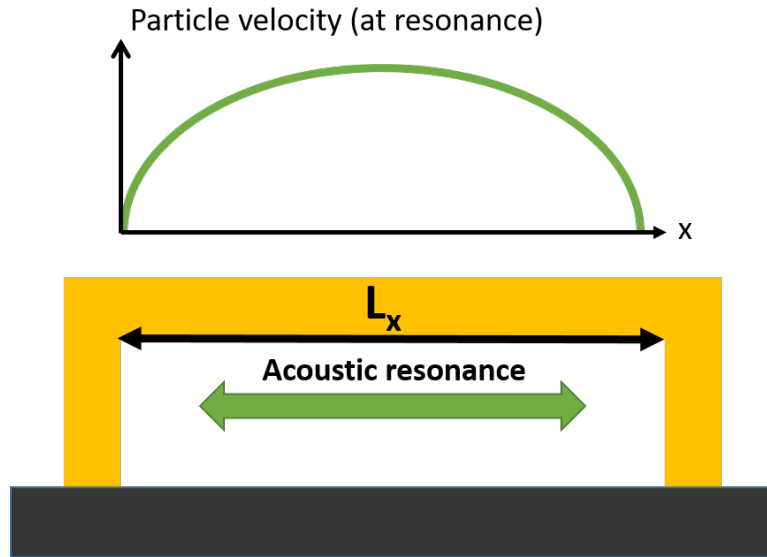


Figure 2.2: Side view of the cavity showing the direction of resonance. Particle velocity within the cavity in  $L_x$  direction is shown at resonance.

## 2.2 Resonator Design

The resonator is an acoustic transducer that is used to excite the acoustic cavity. In order to excite the (1,0,0) acoustic mode as described in Section 2.1, the resonators are designed to be long and slender, and the moving structure (also referred to as a proof mass) vibrates perpendicular to its long edge. As shown in Figure 2.3, the resonator consists of a moving structure, supported by six beams. Electrostatic actuators are placed along the long edge of the resonator.

### 2.2.1 Mechanical Properties

To model each sensor, a spring-mass-damper system is assumed. Such a model has a second order frequency response, representing the resonance in an accurate manner. The response of such a system is defined by the differential equation given in Equation 2.3, where  $m$  is the mass,  $b$  is the damping factor,  $k$  is the spring constant, and  $F(t)$  is the forcing function:

$$m\ddot{x}(t) + b\dot{x}(t) + kx(t) = F(t) \quad (2.3)$$

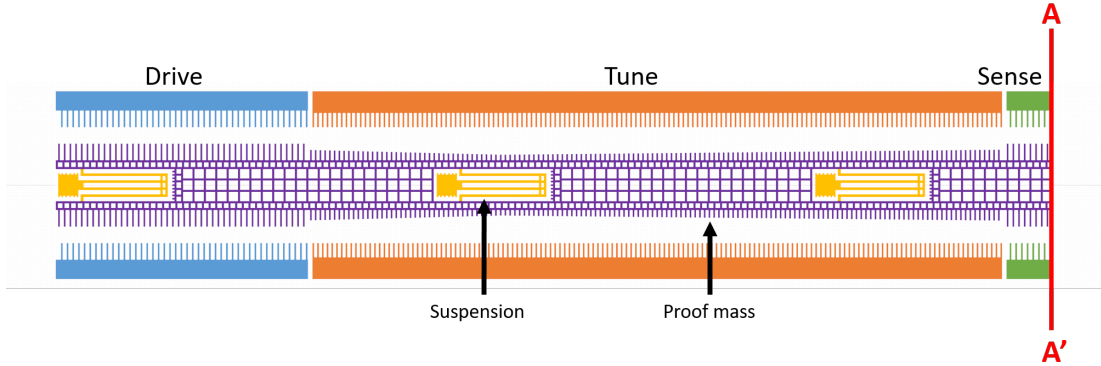


Figure 2.3: A broad overview of a single acoustic resonator, showing the moving structure and each electrode that acts upon it. Only one half of the resonator is shown, the structure is symmetrical along the line A-A'. The proof mass vibrates vertically.

The resonant frequency  $\omega_0$  and quality factor  $Q$  can then be calculated from this equation, as given in 2.4 2.5

$$\omega_0 = \sqrt{\frac{k}{m} - \frac{b^2}{2m^2}} \simeq \sqrt{\frac{k}{m}} \quad (2.4)$$

$$Q = \omega_0 \frac{m}{b} \quad (2.5)$$

The resonant factor can be calculated directly from the physical measurements of the transducer, since the mass and the spring constant of the system is directly dependent on the properties of the silicon wafer. Although there is a dependence on the damping as well, it is neglected during the design procedure. In addition, the proof mass is assumed to be entirely stiff and the suspension is assumed to be massless. The mass of the structure is found using the Area and Density Calculator in Cadence Virtuoso, which reports an area of  $195184\mu\text{m}^2$ . This area can then be multiplied by the device layer thickness and the density of silicon to find the mass:

$$m = A \times t_{\text{devicelayer}} \times \rho_{\text{silicon}} = 195184 \times 10^{-12} \times 15 \times 10^{-6} \times 2330 = 6.82\mu\text{g} \quad (2.6)$$

$m$  = mass,  $A$  = proof mass area,  $t_{\text{devicelayer}}$  = device layer thickness,  $\rho_{\text{silicon}}$  = density of silicon

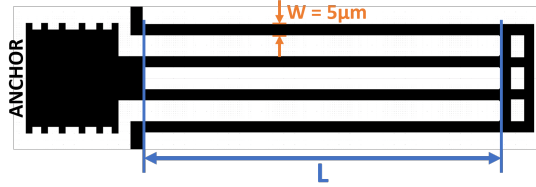


Figure 2.4: Close-up of a single suspension element, showing the measurements of each beam within the element.

As shown in Figure 2.4, each folded beam is actually made up of two springs in parallel, and the structure is folded in half to take up less space. The free end of the beam only moves in the vertical direction. In addition to its compact footprint, this design also has the advantage of being soft in only one direction. The two springs act in parallel when moving in the intended direction, however for torsional or horizontal movement the deflection on each spring is no longer identical, and the structure becomes much more stiff. The overall spring constant is found by the spring constant of each individual folded beam, divided by the number of beams. To find the spring constant of each individual beam, Equation 2.7 gives the spring constant of a single beam in the clamped-guided case, applicable with the assumption that the proof mass moves vertically.

$$k = \frac{24EI}{L^3} = \frac{EW^3h}{L^3} \quad (2.7)$$

$k$  = spring constant,  $E$  = Young's modulus,  $I$  = moment of inertia of the beam,  $L$  = length of the beam,  $W$  = width of the beam,  $h$  = height of the beam

The width of each beam is fixed at  $5\mu\text{m}$  and the Young's modulus of <100> silicon is taken as 130GPa. The height of the beam is equal to the thickness of the device layer, which is  $15\mu\text{m}$ . The length of the beam is a variable which can be tuned during the design process to reach a target resonant frequency. The two outer beams and the two inner beams act in parallel, and these pairs are then combined in series, which means the overall spring constant is equal to that of a single beam. Then, the overall spring constant is six times that of an individual beam.

Using the mass that was previously calculated and Equation 2.7, an analytical estimate of the resonant frequency can be found by entering the values into Equation 2.4. Table 2.2 shows a number of beam lengths and their corresponding resonant frequencies that are found in this manner. The resonator’s frequency should always be higher than the acoustic resonant frequency. This ensures that they can be matched to one another, since the tuning (described in 2.2.4) can only lower the frequency.

Table 2.2: Spring constants and theoretical beam lengths for each target resonant frequency.

L (m)	k (single beam)	k (total)	$f_0$ (Hz)
203.3E-6	29.03	174.18	31800
195.9E-6	32.41	194.45	33600
189.2E-6	35.98	215.85	35400
183.1E-6	39.73	238.36	37200
177.4E-6	43.66	261.98	39000
172.1E-6	47.79	286.72	40800
167.3E-6	52.10	312.58	42600
162.7E-6	56.59	339.55	44400
158.4E-6	61.27	367.64	46200

The quality factor reported for MEMS resonators in similar SOI-MEMS processes are typically very high, ranging from around 10000 [25] to 30000 [26] and potentially beyond. However, this quality factor can only be observed in a vacuum environment, where the primary loss mechanism is by energy coupled into the substrate (anchor loss[27]). In a gas environment, the quality factor observed drops rapidly as the gas pressure increases towards atmospheric pressure, and the primary loss mechanism is damping by atmospheric drag [28] [29]. For example, in the literature a drop from 10000 to 1000 is observed when pressure increases to 10kPa, with a trend showing it will reach 100 at atmospheric pressure [25]. Since the designed transducer is intended to operate in an atmospheric environment, its internal damping is assumed to be negligible and thus is not calculated.

After the theoretical beam lengths are calculated, the design is then imported into COMSOL Multiphysics in order to carry out a finite element (FEA) simulation of the resonator structure. In this simulation, the stationary electrodes

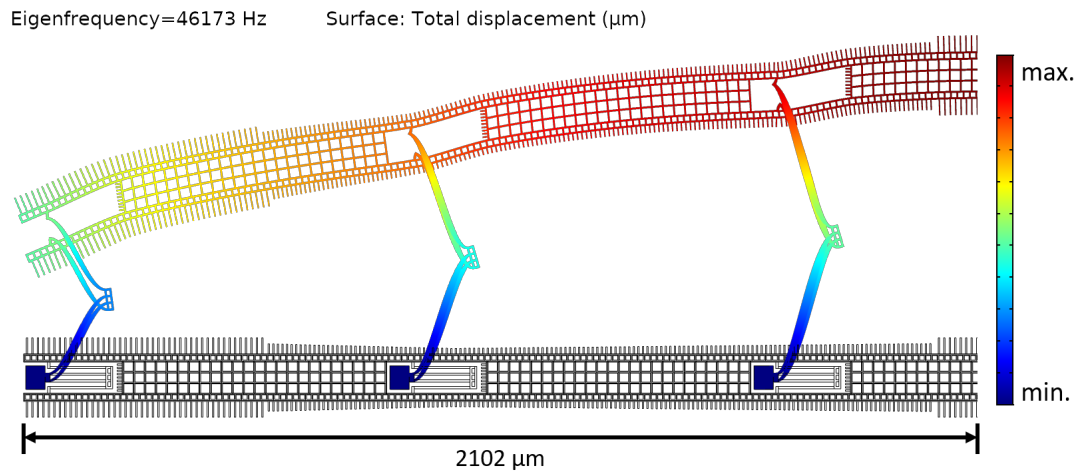


Figure 2.5: FEM output of eigenfrequency simulation. One half of symmetric resonator is shown, while displacement is exaggerated for visual clarity.

are not included and only one half of the transducer is simulated: a symmetry constraint is applied to the middle of the beam so that the simulator can show the behavior of the full resonator. This ensures that less degrees of freedom (mesh elements) will be sufficient to simulate the device, reducing compute time and memory requirements. The moving electrodes on the resonator have a minimal effect on the stiffness of the structure, so they can also be replaced with a single rectangle that adds an identical mass, if the mesh count needs to be reduced further. The material is selected as  $\langle 100 \rangle$  oriented isotropic silicon, matching the wafer, and the anchors are modelled as silicon dioxide squares, with  $2\mu\text{m}$  thickness to match the real device.

To observe the transducer's response in the frequency domain, the "Eigenfrequency" study type is used. This study shows the transducer at resonance, with the plot showing the relative displacement of each part of the transducer. Additionally, the resonance frequency of the transducer is calculated automatically and displayed. Furthermore, more complex resonant modes than the fundamental can be observed, which are difficult to estimate analytically. It is important that higher order resonances are isolated from the fundamental mode to make sure the cavity is driven as cleanly as possible. An example simulation result is shown in Figure 2.5

The largest non-ideality encountered is readily apparent: the moving structure is not completely stiff. When calculating the theoretical resonance frequency of the transducer, in Equation 2.4, it was assumed that the proof mass was perfectly stiff and the beams were perfectly massless, however this is not actually the case. This means that the resonance frequency will be shifted downwards, since the effective beam stiffness is reduced. To reach the desired resonance frequency for each transducer, the beam lengths are tuned iteratively. By solving Eqns. 2.7 and 2.4 together, it is seen that  $f_0 \propto l^{\frac{2}{3}}$ . In a spreadsheet, the target frequency, the actual frequency and the current beam length is recorded. Based on the frequency deviation, a new beam length is recommended, and the FEM model is amended. By iterating this process, the desired resonant frequency is reached despite the non-idealities. The resonant frequency will also be affected by process variations during fabrication, and by the damping introduced by the gas environment, however a good estimate is obtained by this method.

### 2.2.2 Drive Electrodes

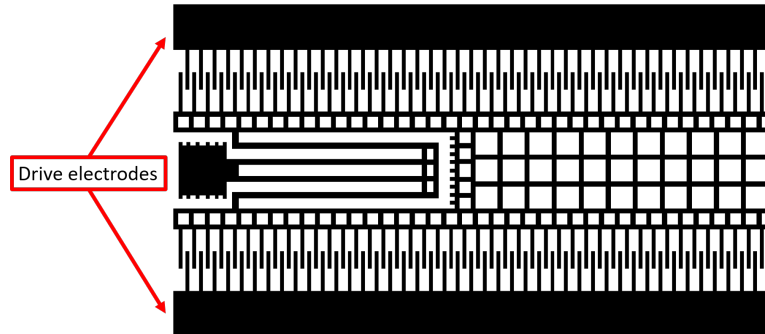


Figure 2.6: Close-up of resonator showing drive electrodes on either side. Fingers on the drive electrode mesh with fingers on the proof mass.

The drive electrodes are implemented using comb-drive actuators located on the ends of the proof mass, as shown in Figure 2.6. Comb drive actuators are weaker compared to parallel plate actuators, however they are necessary in this application. One problem with parallel plate actuators is non-linearity at higher

displacements, since the applied force is proportional to the square of the displacement. The second problem is stability, originating from the nonlinear response. Parallel plate actuators at high displacement have a tendency to pull-in beyond a certain force, potentially becoming stuck in the process. Since high displacement is needed for high SNR in this sensor design, a comb drive is always used for the drive actuator. The force applied by an electrostatic actuator is given by Equation 2.8. In the case of a comb drive actuator,  $\frac{dC}{dx}$  is found by Equation 2.9. Figure 2.7 shows the relevant dimensions.

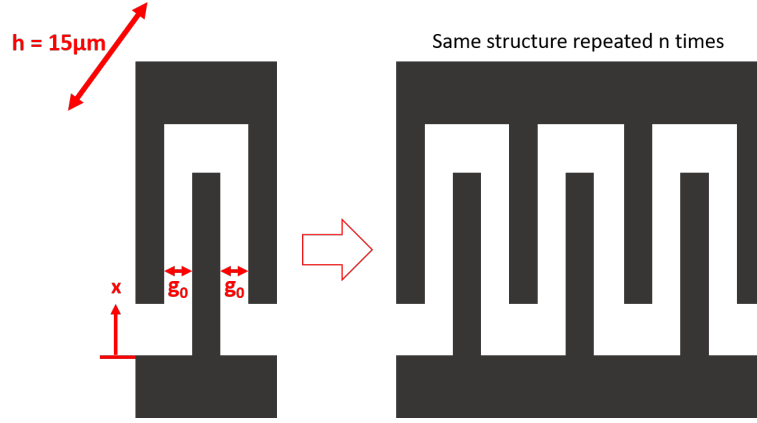


Figure 2.7: Diagram of comb drive actuators showing direction of travel and relevant dimensions.

$$F = \frac{-1}{2} V^2 \frac{dC}{dx} \quad (2.8)$$

The voltage across the drive electrodes is equal to  $V_d + V_{pm}$  where  $V_d$  is the AC voltage applied to the stator and  $V_{pm}$  is the DC bias voltage applied to the proof mass.

$$\frac{dC}{dx} = \frac{2\epsilon_0 \cdot h \cdot n}{g_0} \quad (2.9)$$

By inserting  $\frac{dC}{dx}$  into Equation 2.8 and linearizing around  $V_d = 0$ , Equation 2.10 is obtained. Furthermore, since both ends of the proof mass are subjected to identical  $V_{pm}$ , the constant force term becomes eliminated, while the differentially applied  $V_d$  remains to apply a net force.

$$F = V_{pm} V_d \cdot \frac{2\epsilon_0 \cdot h \cdot n}{g_0} \quad (2.10)$$

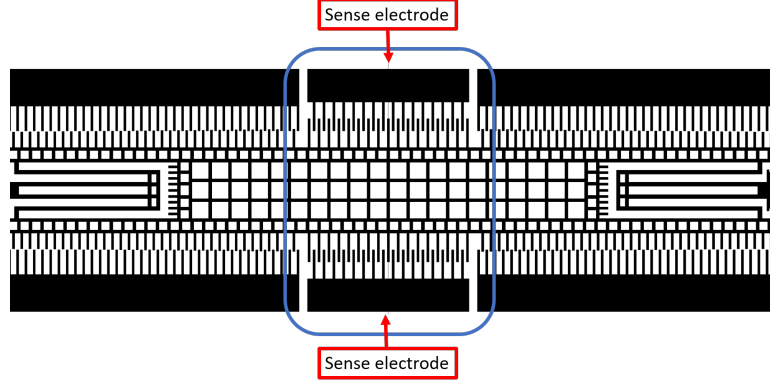


Figure 2.8: Close-up of resonator showing the center section, where sense electrodes are placed.

Each actuator has 44 sets of fingers, and there are a total of four actuators driving each resonator. Therefore, the total force can be calculated as  $15.576 \cdot V_{pm} \text{ nN/V}^2$ .  $V_{pm}$  is left as an unknown because its value can be changed during testing, however a typical value of 40-60V is preferred. Increasing  $V_{pm}$  increases the gain of every actuator, however beyond a certain threshold arcing can occur which will damage the device.

### 2.2.3 Sense Electrodes

For the sense electrodes, two varieties of electrode are used to pick off the output signal. The first variant is a comb drive actuator, shown in Figure 2.8. These are located on the middle of the beam, where the largest displacement occurs in the moving structure, in order to obtain the largest possible signal at the output. Unlike the drive actuator, the sense electrode only has 16 sets of fingers on each side, for a total of 32. The electrical sensitivity of the sense actuator can be derived from the relation  $Q = CV$ . The stator is read out by a transimpedance amplifier, described in detail in Section 4.1.3, which keeps the stator potential at virtual ground. Therefore, as seen in Equation 2.11, any change in capacitance results in a proportional amount of output charge, which is amplified by the readout electronics.

$$\frac{dQ}{dx} = \frac{dC}{dx} V_{pm} = \frac{2\epsilon_0 \cdot h \cdot n}{g_0} V_{pm} \quad (2.11)$$

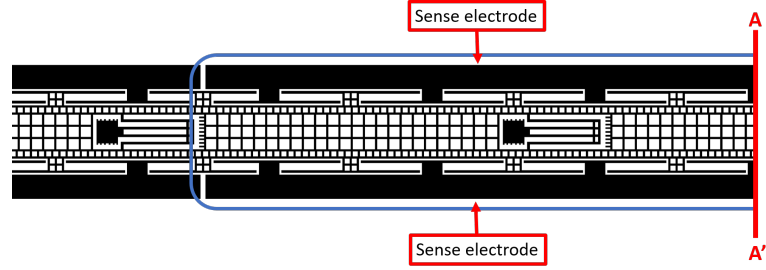


Figure 2.9: Close-up of parallel plate resonator showing sense actuator. Only half of the actuator is shown, the device is symmetrical along the line A-A'.

The sensitivity of the comb drive sense electrode can thus be calculated as  $2.832 \cdot V_{pm} nC/V \cdot m$ , again leaving  $V_{pm}$  as an unknown to be substituted in.

The second variant of the sense electrode is a parallel plate actuator shown in Figure 2.9. This style of sense electrode is susceptible to the same shortcomings described in Section 2.2.2 and for this reason they are only used on the detector resonators (shown in more detail in Section 2.3). The detector resonator is not driven in operation, which means the displacement of the resonator is much lower, allowing the output to be mostly linear. The sensitivity of this electrode is found using Equation 2.12.

$$\frac{dQ}{dx} = \frac{dC}{dx} V_{pm} = \frac{-\epsilon_0 \cdot A}{d^2} V_{pm} \quad (2.12)$$

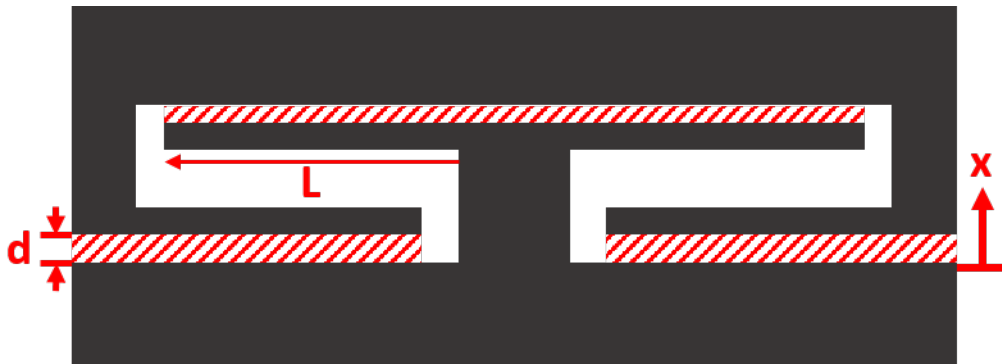


Figure 2.10: Diagram of parallel plate electrodes

In this equation  $A$  is the area exposed on the parallel plates. Figure 2.10 shows the parts that are included in this calculation. Considering a layer thickness of  $15\mu\text{m}$  and a total length of  $6972\mu\text{m}$ ,  $A$  is found as  $104580\mu\text{m}^2$ , while  $d = 4\mu\text{m}$ . Therefore the sensitivity of the parallel plate sense electrode can be calculated as

$57.87 \cdot V_{pm} nC/V \cdot m$ , allowing a significant increase in sensitivity to be attained compared to the comb drive.

## 2.2.4 Tuning Electrodes

The tuning electrodes are critical to the operation of the resonators. The acoustic cavity dimensions can not be changed after fabrication, and an impractical level of process optimization is required to make cavity and resonator match perfectly. Therefore, the resonators' frequency must be tunable in order to match every resonant system involved in this sensor. The tuning electrodes apply a force on the moving structure which is proportional to its displacement like a mechanical spring, adding a negative spring constant  $k_e$  to the system. Based on Equation 2.4, this will cause the resonant frequency to shift downwards.

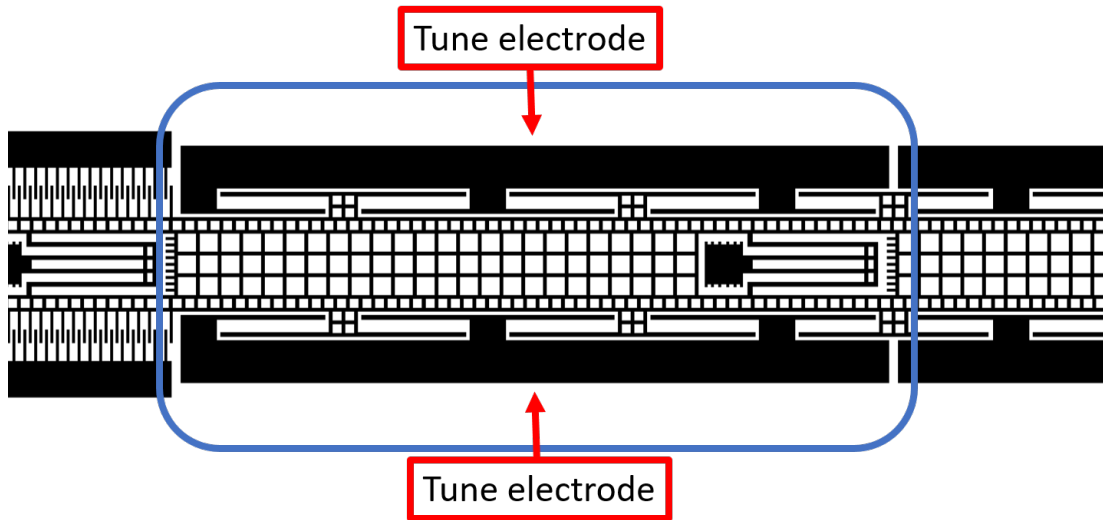


Figure 2.11: Close up of parallel plate resonator showing tuning electrodes.

As with the sense electrodes, there are also two variants of the tuning actuators. For the detector resonator, where a low displacement is needed, a parallel plate version shown in Figure 2.11 is used. For the parallel plate case, the force is determined by Equation 2.13 the spring constant is given by Equation 2.14, where  $x_0$  refers to the gap when the proof mass is centered.

$$F = \frac{1}{2} \frac{\delta C}{\delta x} V_{DC}^2 \quad (2.13)$$

$$k_e = \frac{dF}{dx} = \frac{\delta}{\delta x} \frac{1}{2} \frac{-\epsilon A}{(d-x)^2} V_{DC}^2 \simeq \frac{\epsilon A}{d^3} V_{DC}^2 \quad (2.14)$$

The geometry of the parallel plate tuning electrodes are similar to those of the parallel plate sense electrodes, however the area of the capacitor is smaller,  $A = 82170\mu\text{m}^2$ , while  $d = 4\mu\text{m}$  as before. Therefore  $k_e = 11.36V_{dc}^2\text{mN} \cdot \text{V}^2/\text{m}$ . In practice, two sets of electrodes act on the proof mass, and therefore  $k_e = -22.72V_{dc}^2\text{mN} \cdot \text{V}^2/\text{m}$

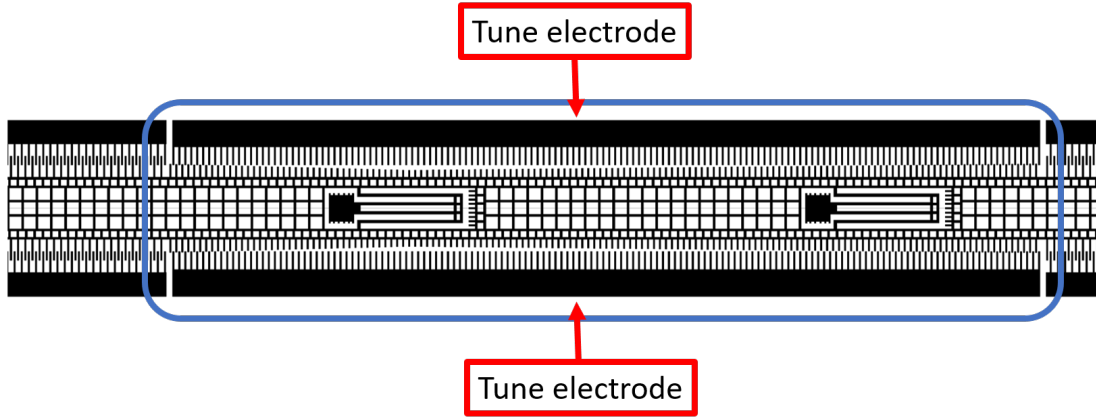


Figure 2.12: Close up of comb drive resonator showing tuning electrodes.

The other variant of tuning actuator that is used is a length tapered comb actuator, shown in Figure 2.12. The advantage of this electrode geometry is that  $k_e$  is independent of the displacement, allowing for linear tuning. This condition applies when at least one but not all of the tapered fingers are interacting with the constant length fingers. The length tapering, shown in Figure 2.13 causes more fingers to interact with increasing displacement, which means that the capacitance increases parabolically, and therefore  $\frac{\delta C}{\delta x}$  increases linearly, as given in Equation 2.15[30]. When  $\frac{\delta F}{\delta x}$  is calculated, only a constant term remains, which is  $k_e$  (Equation 2.16).

$$\frac{\delta C}{\delta x} = \frac{\epsilon_0 h}{g_0 \Delta L} x \quad (2.15)$$

where  $h$  is layer height,  $g_0$  is the gap between the fingers, and  $\Delta L$  is the length difference between adjacent fingers.

$$k_e = \frac{-\epsilon_0 h}{g_0 \Delta L} \quad (2.16)$$

In the design,  $g_0 = 2\mu\text{m}$ . Each electrode actually has two sections, one with  $\Delta L = 0.25\mu\text{m}$  and another with  $\Delta L = 0.1\mu\text{m}$ . To compensate this structure,  $\Delta L$

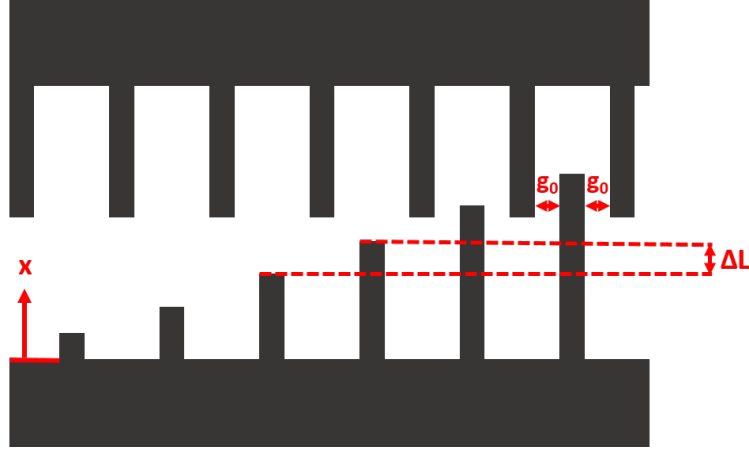


Figure 2.13: Diagram of length tapered comb actuator showing the relevant dimensions and the tapering effect.

is taken as  $0.1\mu\text{m}$  and a multiplication factor of 2.8 is added to include the effect of the other section. Therefore,  $k_e = -1.859V_{dc}^2\text{mN} \cdot \text{V}^2/\text{m}$ , and considering the second set of electrodes,  $k_e = -3.718V_{dc}^2\text{mN} \cdot \text{V}^2/\text{m}$

In order to verify the operation of the tuning electrodes, FEA simulation is used. The model is constructed with only one tuning electrode surrounded by air. A constant potential is applied to each electrode and the FEA software is set up to derive the capacitance between the electrodes based on the accumulated charge. In addition, a parametric sweep is set up to calculate the capacitance for multiple values of displacement. Although at least some of the fingers need to be inside the opposing comb to achieve the linear spring constant, the simulation is set up with a displacement of  $0\mu\text{m}$  corresponding to the longest finger being just outside of the comb. Figure 2.14 shows the model with an overlaid color map indicating the electrical potential. The measured capacitance for each value of displacement is shown in Figure 2.15. From this capacitance, the change in capacitance per distance is calculated for each point and plotted in Figure 2.16. As previously demonstrated in Equation 2.16, the spring constant is proportional to the rate of change of capacitance. A linear trendline is added, showing a correlation coefficient of 0.99 with the measured data.  $k_e$  can be found from the slope of the trendline, with a multiplication by 2 needed to account for the number of sets of tune electrodes on the device:  $k_e = -2.8V_{dc}^2\text{mN} \cdot \text{V}^2/\text{m}$ . Some

nonlinearity is observed at high displacement, this is because all of the tapered fingers are already in engagement at this point and at this point the actuator behaves like a regular comb drive actuator. Due to this nonlinearity and fringing fields around the finger tips, there is some deviation between the FEA simulated spring constant and the calculated spring constant.

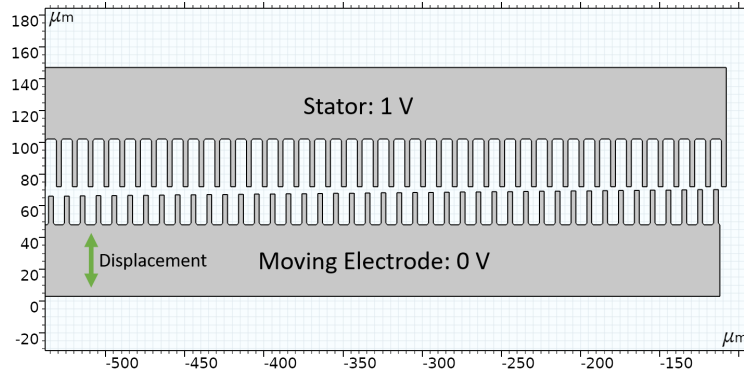


Figure 2.14: Finite element model of length tapered comb tuning electrodes, showing the electric potential within the space.

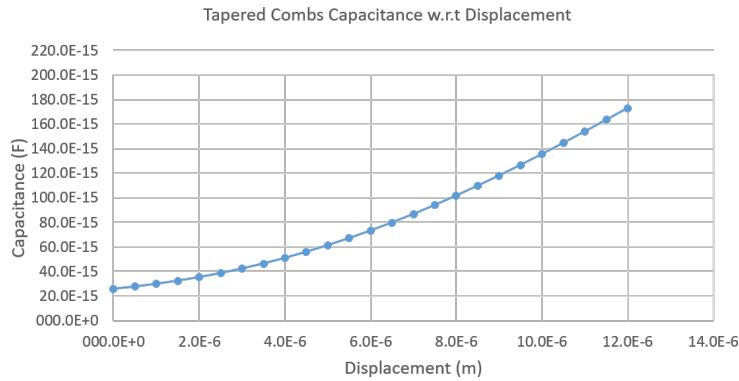


Figure 2.15: Capacitance of one set of tapered combs with respect to displacement, calculated using FEA.

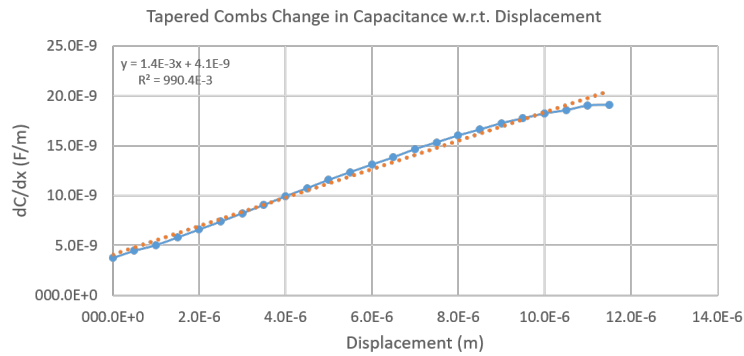


Figure 2.16: Change in capacitance with respect to displacement of tapered combs, calculated using FEA.

In addition, the parallel plate tuning electrodes are also simulated using the same method. The model with overlaid potential distribution is shown in Figure 2.17. For this model, a displacement of  $0\mu\text{m}$  is taken to be the resting position of the proof mass. Figure 2.18 shows the capacitance measured at each displacement value, while Figure 2.19 shows  $\frac{dC}{dx}$  for each of the same points. It can be seen that the electrical spring constant, which is proportional to  $\frac{dC}{dx}$ , quickly increases with displacement, which can counteract the mechanical spring constant and cause instability. With the assumption that the proof mass remains near its center point,  $k_e$  is measured near zero. Taking into account all four tuning electrodes,  $k_e = -23.6V_{dc}^2\text{mN} \cdot \text{V}^2/\text{m}$ .

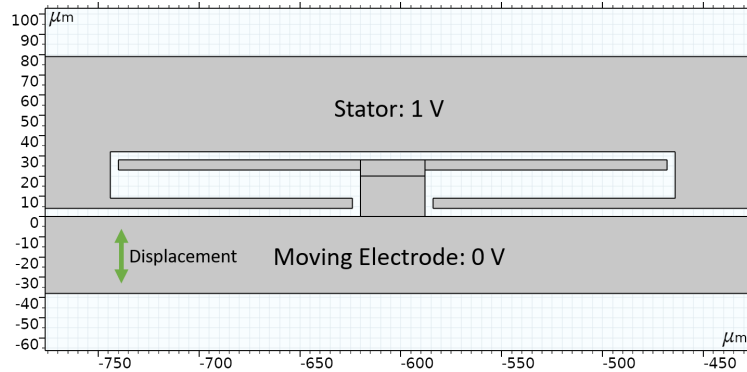


Figure 2.17: Finite element model of parallel plate tuning electrodes, showing the electric potential within the space.

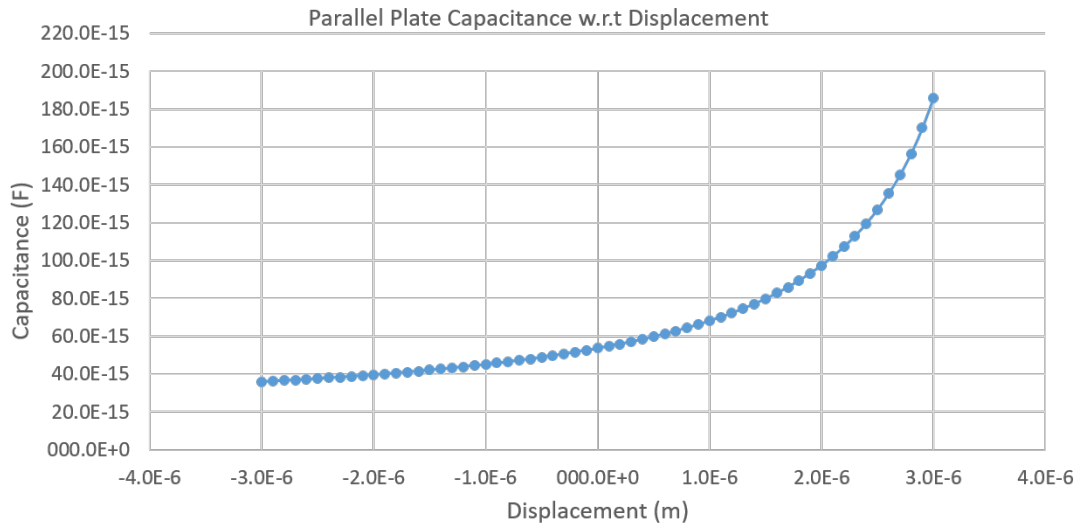


Figure 2.18: Capacitance of one set of parallel plates with respect to displacement, calculated using FEA.

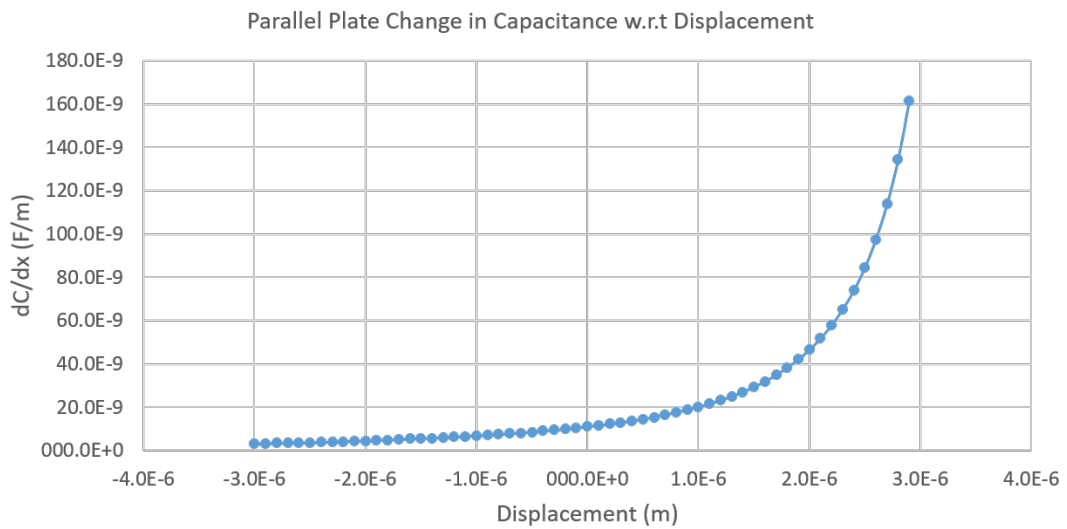


Figure 2.19: Change in capacitance with respect to displacement of tapered combs, calculated using FEA.

## 2.3 Overall Sensor

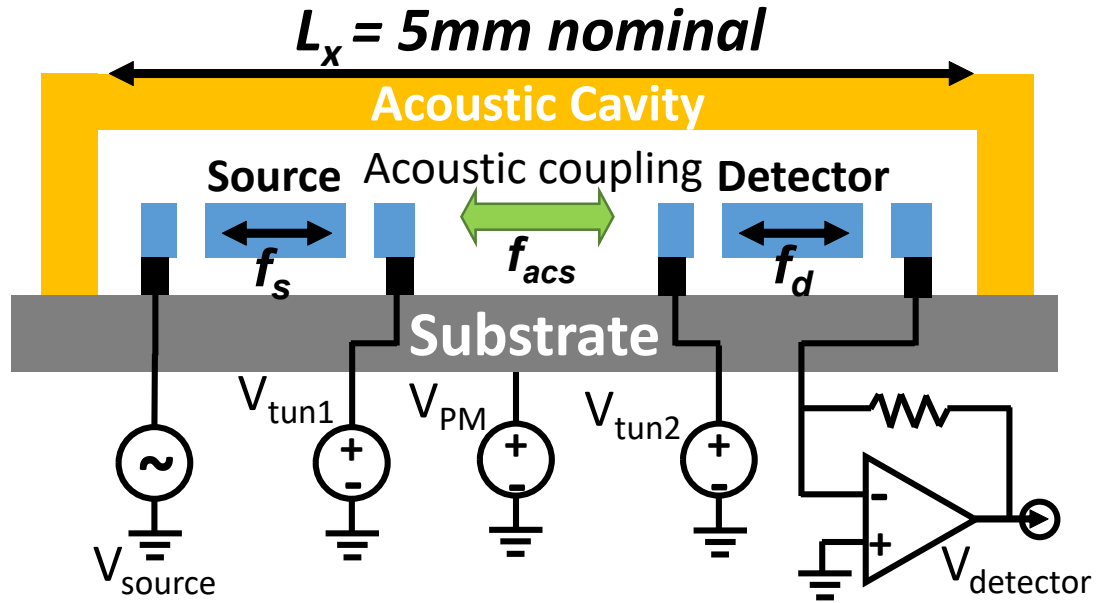


Figure 2.20: Diagram of sensor system.

In Figure 2.20, the placement of the acoustic cavity over the resonators is shown. The resonators are inside the plane of the silicon wafer, forming one wall of the acoustic cavity, and therefore their coupling to the acoustic cavity can be considered very small. Due to the small degree of coupling between resonator motion and gas particle motion, the acoustic resonance is considered not to be disturbed by the presence of the resonators. Although the exact mechanism of coupling is not examined in this work, the shape of the proof mass, with many gaps in the structure placed to facilitate the fabrication process, the drag coefficient of the proof mass is estimated to be very high. Therefore, an viscous friction based coupling, where resonator velocity influences particle velocity within the gas, can be considered likely.

As shown in Figure 2.21, the sensor die is designed with a total of six resonators on each die. These resonators are arranged as three pairs of source and detector resonators in order to cover a wider frequency range. Based on the electrical softening made available with the tuning electrodes described in Section 2.2.4, the tuning range of each transducer is determined as 1.8 kHz in the worst

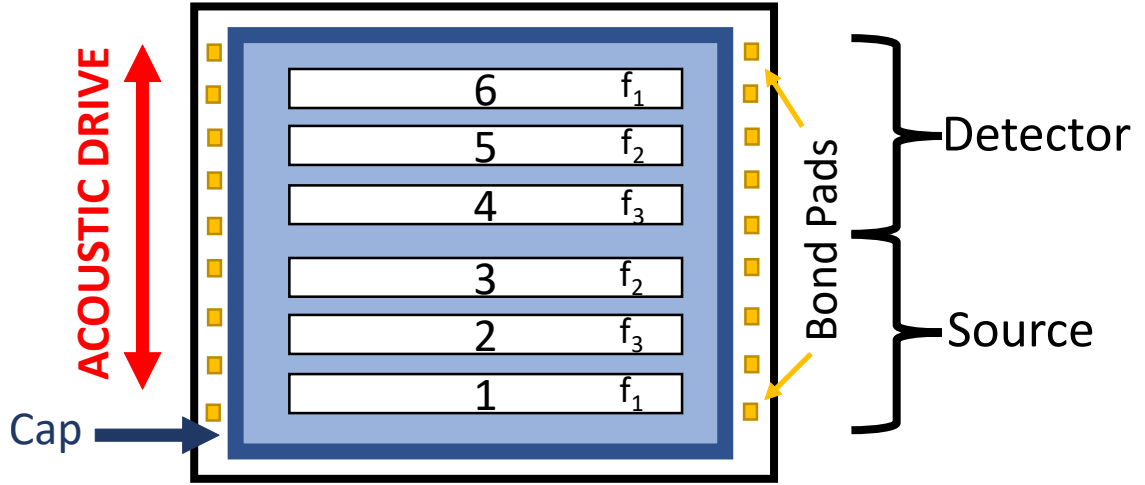


Figure 2.21: Diagram of transducers on sensor die showing physical layout.

case, with a tuning voltage of 100 V. This is determined to be insufficient to cover potential process variations since the fabrication process is developed from scratch. Therefore, each pair of resonators are selected with a resonant frequency approximately 1.8 kHz apart. In addition, multiple sets of different frequencies are selected in order to further maximize the available options. Table 2.3 shows the different die frequencies that are selected. On both of the dice where parallel plate transducers are used, the parallel plate resonators were set at 39000 Hz, 42000 Hz and 46000 Hz due to their wider tuning range, and the table indicates the resonant frequencies of the source resonators, which are implemented using the comb drive design.

Table 2.3: Table of selected resonant frequencies for each sensor die.

Device	Frequency 1 (Hz)	Frequency 2 (Hz)	Frequency 3 (Hz)
Comb 1	31800	33600	35400
Comb 2	37200	39000	40800
Comb 3	42600	44400	46200
Parallel Plate 1	37200	39000	40800
Parallel Plate 2	42600	44400	46200

In summary, the proposed gas sensor consists of an acoustic cavity with a rectangular shape, that is excited in its (1,0,0) resonant mode along its x axis. The

x dimension of the cavity and the speed of sound of the gas within determines the resonant frequency. With known dimensions, a measurement of resonant frequency can thus be used to derive the resonant frequency. The cavity is excited using a weak coupling from two in-plane mechanical resonators. One resonator drives the cavity while the other resonator listens for the response. These resonators are electrically tunable to match the cavity response.

# Chapter 3

## MEMS Fabrication

The designed gas sensor is fabricated using an in-house developed MEMS process. In this chapter, the details of the fabrication process are given, and the development of the process is described. In general, the process steps are as follows:

1. Metal coating and patterning bond pads, Section 3.1.1
2. Device layer DRIE etch, Section 3.1.2
3. Release etch of sacrificial oxide, Section 3.1.3
4. Fabrication of acoustic cavity, Section 3.2

The general process flow is shown in Figure 3.1.

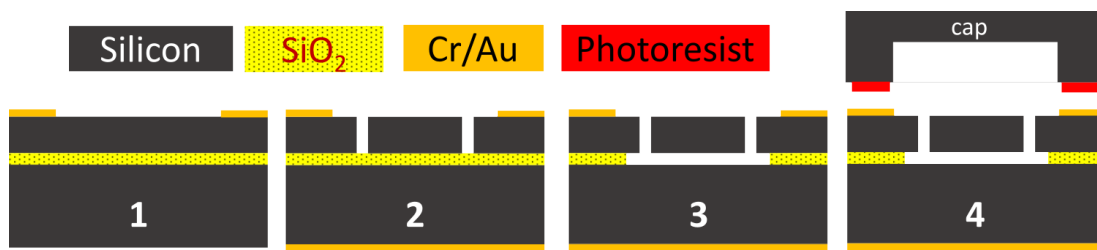


Figure 3.1: Diagram showing the general steps to the fabrication procedure.

## 3.1 Sensor Die

### 3.1.1 Metal Layer

The fabrication of the sensor die is carried out on a silicon SOI wafer with a  $525\mu\text{m}$  thick handle layer, a  $2\mu\text{m}$  thick insulating oxide layer and a  $15\mu\text{m}$  thick device layer. The wafer is first cleaned using piranha solution and buffered oxide etch (BOE) to remove any contaminants as well native oxide which forms on the wafer in storage. After this initial cleaning process, the cleanliness of the wafer is further maintained by washing in acetone, isopropyl alcohol (IPA) and deionized water. A thermal evaporator is used to coat the wafer with approximately 8nm of chrome as an adhesion layer and  $0.5\mu\text{m}$  of gold. The thickness of the gold layer is not critical, because it will only be used for wire bonding pads. The interconnect within the die is then carried out exclusively with silicon.

After coating the wafer, HMDS and Microchemicals AZ 5214 photoresist (Ulm, Germany) are spin coated onto the wafer. Using the EVG 620 mask aligner system (St. Florian, Austria), the photoresist is patterned with the metal mask. To avoid sticking to the mask, soft contact mode is used, since this step is not as critical. Using dummy silicon wafers, the correct exposure power is determined experimentally. After lithography, AZ 400K developer at 1:4 dilution with deionized water is used in order to develop the photoresist. The development process typically takes between one and two minutes, however the ultimate development time is determined by observation to make sure all features are developed correctly.

Following the patterning process, a two step wet etch is performed to remove the unwanted metal. First, the wafer is submerged in aqua regia, using 2:3:1 ratio of water, 37% hydrochloric acid, and 70% nitric acid respectively, in order to etch the gold layer. After rinsing with deionized water, the wafer is then etched once more using TechniEtch CR01 (Ulm, Germany) chrome etchant solution to remove the now exposed chrome layer. Once this wet etch process is completed, the photoresist layer is stripped using Microchemicals AZ 100 remover solution.

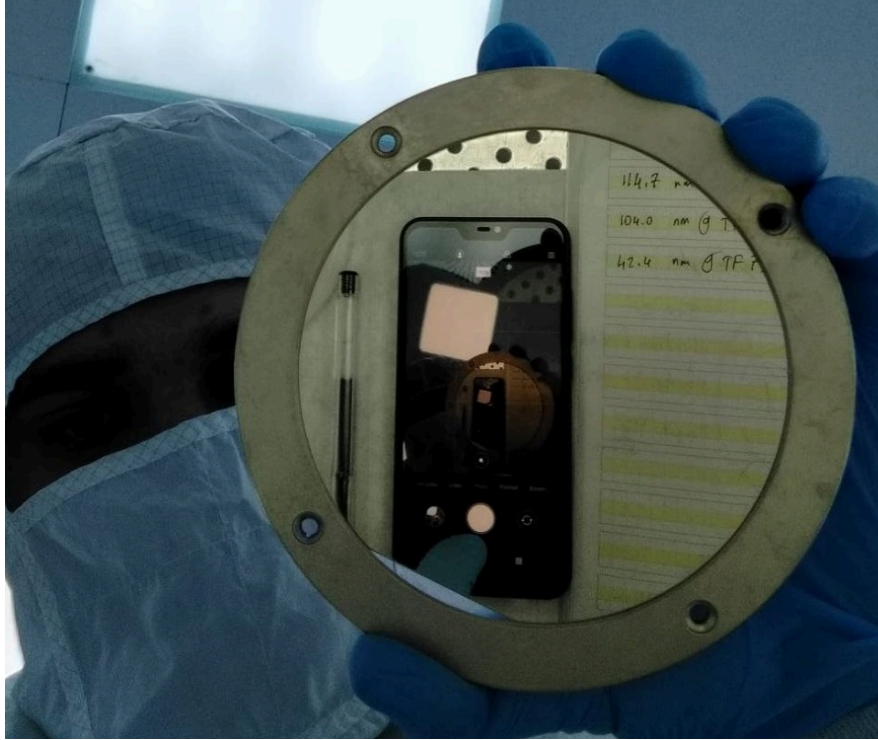


Figure 3.2: Wafer after gold coating

The wafer is then turned over and the back side is also coated with a gold layer, using the same procedure as the front side. The chrome thickness is kept the same, however the gold layer is coated to approximately  $1\mu\text{m}$  thickness. This back side coating is intended to connect the handle layer to a known voltage. If this layer is left unconnected, its voltage will be undefined, potentially applying unpredictable forces onto the proof mass.

### 3.1.2 Device Layer

The second part of the fabrication process uses another mask to form the moving structure. The wafer is spin coated with HMDS and Microchemicals AZ 5214E photoresist at 4000 rpm for 60 seconds to form a  $1.4\mu\text{m}$  layer, followed by a  $110^\circ\text{C}$  soft bake. Using the mask aligner, the device layer pattern is exposed onto the wafer. This layer has much finer details, with a minimum feature size of  $2\mu\text{m}$ ,

compared to the metal layer with the smallest feature in excess of  $50\mu\text{m}$ . To gain increased resolution, the vacuum and hard contact mode is used.

The development is carried out using 1:4 diluted AZ 400K developer. Although the development time is expected to be around 1-2 minutes like before, the AZ 5214E resist used took much longer to develop, with more than 17 minutes spent in the developer solution. During this time, the features were routinely inspected under a microscope to confirm the completion of the development process. This discrepancy is presumed to be due to decomposition in storage of the photoresist in UNAM, however since the patterning step is completed successfully, the cause of the discrepancy is not investigated further.

The device layer is formed using the DRIE process. A STS Multiplex inductively coupled plasma (ICP) machine (Newport, UK) is used. In the deposition cycle  $C_4F_8$  plasma is introduced to coat the exposed silicon with a polymer layer. Then in the etch cycle  $SF_6$  and oxygen plasma is introduced which etches silicon. A DC and low frequency RF source is used to accelerate ions downward, causing an anisotropic etch. Using this technique, high aspect ratio trenches are obtained.

The etch recipe for this process was developed by modifying an existing DRIE recipe available in the ICP machine. Dummy silicon wafers are patterned, etched, and scribed. Using a scanning electron microscope (SEM), the cross section is viewed and the etch recipe is modified based on the measured cross section. The wafer includes test dice for this purpose, with features of different sizes that reveal common etch problems. A test die is shown under an optical microscope in Figure 3.6, highlighting the test features from another perspective. SEM micrographs of some etch problems are shown in Figure 3.3 and Figure 3.4. Using the SEM as a reference, the DRIE recipe is adjusted until an acceptable result is obtained. Figure 3.5 shows the improvement made to the etch recipe. The sidewall profile can slope due to an imbalance of gas flow or RF power between etch and deposition cycles. Another reason for sloping sidewall is excessive power, causing ions to be deflected from the trench floor, which then strike the sidewall and etch it away.

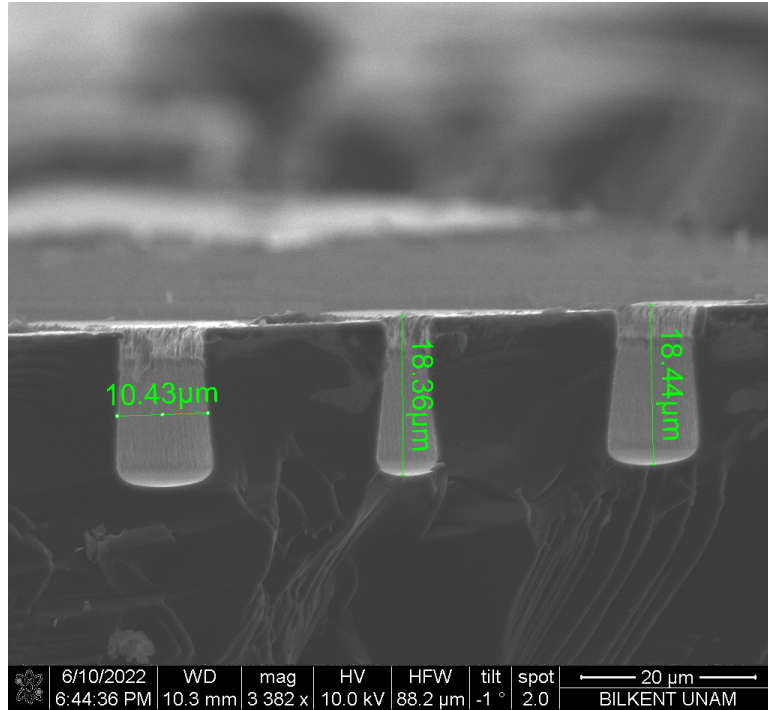


Figure 3.3: Example of dummy wafer used to test DRIE. Although etch depth is close to being acceptable, especially in narrower trenches the sidewall profile is clearly getting distorted by the etch process. It is likely that the accelerated ions striking the bottom of the trench are being deflected back and striking the sidewalls as the trench gets deeper.

One solution to this sloping sidewall problem is to reduce the etch power, although this also increases the etch time to unacceptable levels. Instead, the ICP machine has a second low frequency RF source for this task. The main RF power is delivered using a 13.56 MHz inductive coupling loop, while the low frequency RF source delivers 380 kHz directly to the platen holding the sample. This RF source has the effect of reducing the needed DC bias and main RF power to bring ions to the trench floor, improving the sidewall profile.

Although the SOI device layer has a thickness of  $15\mu\text{m}$ , a target depth of  $20\mu\text{m}$  is chosen to ensure the completion of the process. Figure 3.7 shows a SEM image of a dummy wafer showing a successful etch. The oxide layer is not readily etched by the  $SF_6$  plasma, which means that the etch process will stop naturally when this layer is exposed on a SOI wafer. The final DRIE parameters are given in Table A.1.

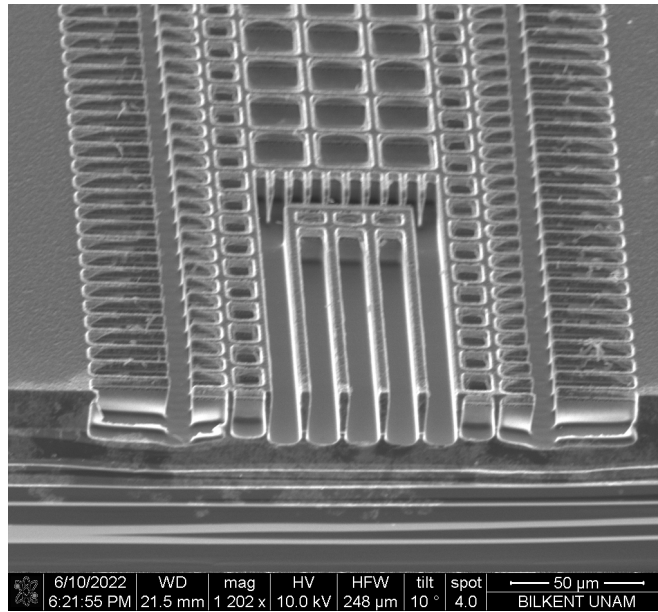


Figure 3.4: Example of dummy wafer used to test DRIE. As with Figure 3.3, the sidewall is sloping outwards, adversely affecting the thinner suspension and proof mass.

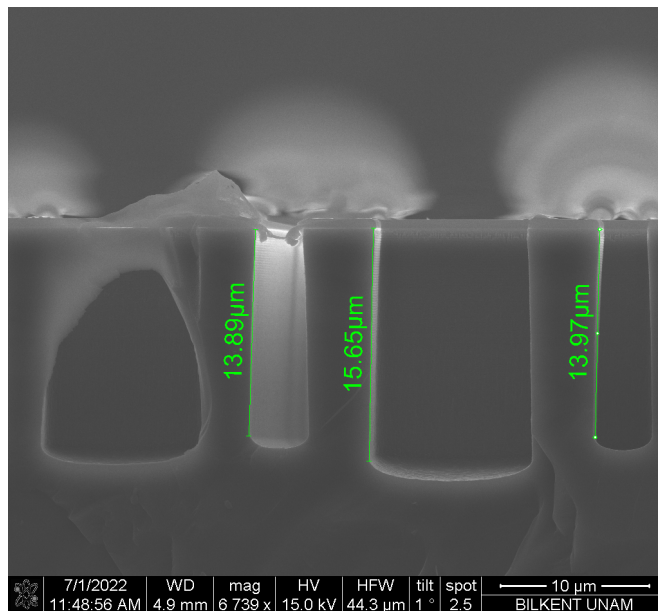


Figure 3.5: Example of dummy wafer used to test DRIE. Sidewall profile is not parallel, although there is some improvement. The changes made to the etch recipe to improve sidewall profile have slowed down the process, causing the trenches to be etched less than what is needed. Even with an 15 $\mu$ m wafer, it is clear that the bottom will not always be reached.

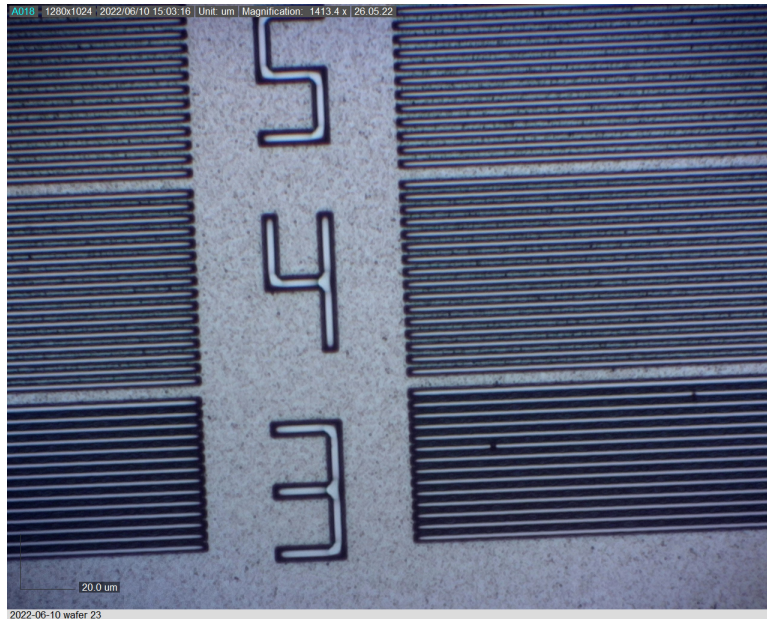


Figure 3.6: Optical microscope photo of dummy wafer, zoomed in on test structures. The number indicates the width of each trench in  $\mu\text{m}$ .

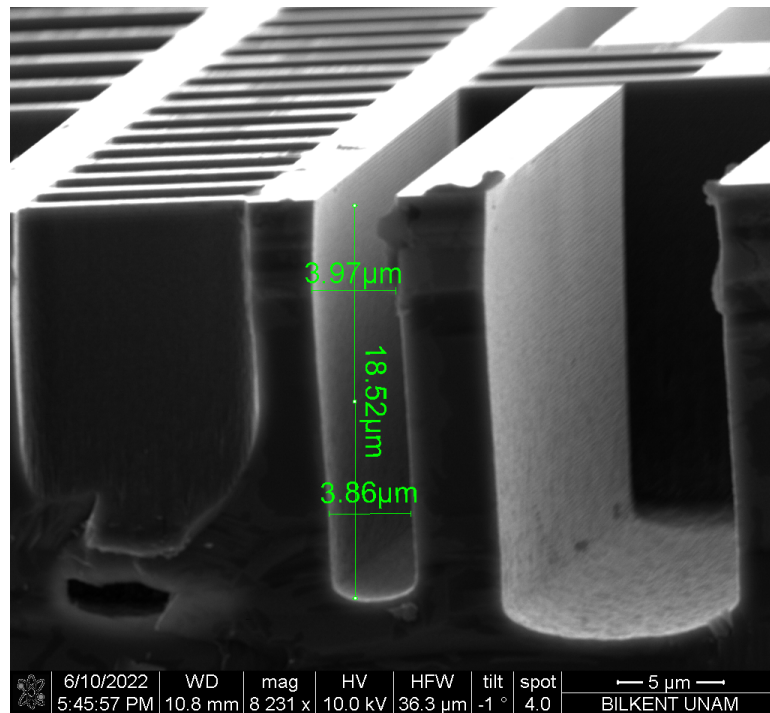


Figure 3.7: SEM image of dummy wafer, showing cross section of etched features.

### 3.1.3 Die Release

With both device and metal layers fully formed, the wafer is sawn into individual dice using a DISCO DAD 3220 (Tokyo, Japan) dicing saw. The dice are not functional at this point, since the moving structure is still held in place by the oxide layer below. To obtain usable dice, a release etch must be performed. In order to minimize losses due to contamination or an incorrect release process, only two or three dice are processed at a time. The selected dice are washed with acetone, isopropyl alcohol, and deionized water to remove the majority of the photoresist left over from the DRIE step, and piranha solution is used to clean any remaining residue. The piranha step is needed because the DRIE process chemically degrades the photoresist, leaving a residue that is not easily removed with solvent cleaning. The dice are then wet etched in hydrofluoric acid (HF) to remove the oxide layer holding the moving structure. The HF is selective towards the oxide layer, leaving the device layer unharmed. In order to allow for a wide tolerance in etch time, the anchors of the moving structure are designed to be tolerant of undercut during this step. Concentrated HF etches  $SiO_2$  at 2330 nm/min [31], so the etch is left to proceed for 6 minutes. Features on the device layer which are narrower than  $28\mu\text{m}$  are released, while larger features have oxide remaining underneath, serving as an anchor layer. Buffered oxide etch (BOE) solution can also be used for this step, however the etch rate is found to be insufficient, leading to the use of concentrated HF. After the release etch, the dice are left in deionized water overnight to rinse the dice and make sure that no HF droplets are trapped between the device layer and the handle layer. Upon carrying out the release etch on the first batch of dice, one die is taken apart to examine the etch result. Common sticky tape is used to pull off the proof mass from the die, and an optical microscope is used to look at the underside. Figure 3.8 shows the underside of such a proof mass. Some sacrificial oxide is shown to have remained on the device, however it is etched sufficiently that it can start to move. In any case, upon this observation the etch time is increased to 6.5 minutes to make sure that all of the sacrificial oxide is removed. The anchors are designed with a wide tolerance so that they are unaffected by the resulting undercut.

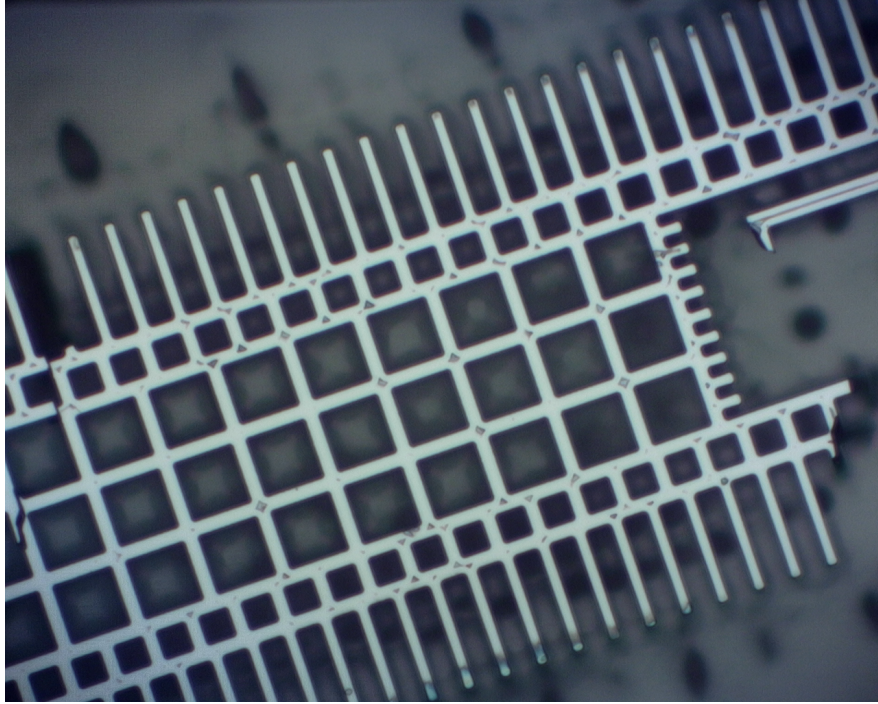


Figure 3.8: Underside of a proof mass showing remnants of sacrificial oxide from the release etch process.

The released dice at this point are fragile and must be treated with special care. At the surface level, it appears trivial to dry the dice and continue on with testing, however stiction presents itself as one of the largest issues at this process step. Due to the geometry of the resonators, there exists many long cantilevered structures which can be bent downward by surface tension. Removing the sample from water and allowing it to dry on a hotplate is found to cause collapse of the moving structures, as the suspended silicon is pulled down towards the handle layer by surface tension, and the two layers are stuck together when the water in between is fully evaporated. Once stuck, a large surface tension force and electrostatic forces work together to make it impractical to separate the two layers. In order to recover dice stuck in this manner, exposure to vacuum and heating to  $200^{\circ}\text{C}$  is attempted to drive out any remaining water without success. In addition, pushing the proof mass with a probe needle is also attempted. This method can sometimes release the proof mass, however in most cases the forces involved are sufficient to cause damage before the structure is released.

This stiction behavior is also encountered with other solvents which have lower surface tension, such as n-hexane, methanol, isopropanol and acetone. Compared to many MEMS devices encountered in the literature, this sensor's structure is exceptionally sensitive to this effect, which leaves two solutions. The first solution is to use HF vapor to carry out the release etch instead of liquid HF, in order to keep the die dry from the start. This solution is preferable due to its simplicity, however a specialized etcher is needed to contain the hazardous vapors and such an etcher was not available. In the second solution, which was the chosen option, the dice are dried using a Tousimis Automegasamdri 915B (Rockville, MD, USA) critical point dryer (CPD). In the CPD, the sample is initially loaded into an ethanol filled chamber. Liquid  $CO_2$  at high pressure is introduced and the ethanol is slowly drained from the chamber until only liquid  $CO_2$  remains. Alcohols such as ethanol are preferred due to its high miscibility with liquid  $CO_2$ , which is not observed in water or other solvents. By increasing the pressure and temperature past the critical point of  $CO_2$  at  $31^\circ C$  and  $72.8 \text{ atm}$ , a supercritical fluid with no surface tension is now achieved in the chamber. Finally, when the chamber is vented, the samples are dry with no stiction effects observed. When loading the CPD, the dice are passed from a water bath through acetone, isopropanol and ethanol baths, to prevent any sudden change of surface tension when going from water directly to ethanol. After the machine is loaded and started, the process is fully automatic and can run unattended.

After the dice are removed from the CPD, they are inspected using an optical microscope for defects or any collapsed structures. Collapsed structures can be detected by observing the moving structure and stator electrodes. When the structure is properly released, both sides will come into focus at the same time. When the structure is collapsed, it will not be in focus at the same time as the stator, which can be easily detected at high magnifications where the focal plane of the microscope becomes very narrow. Dice that are properly released are taken out of the cleanroom for post-fabrication processing as described in Section 3.3.

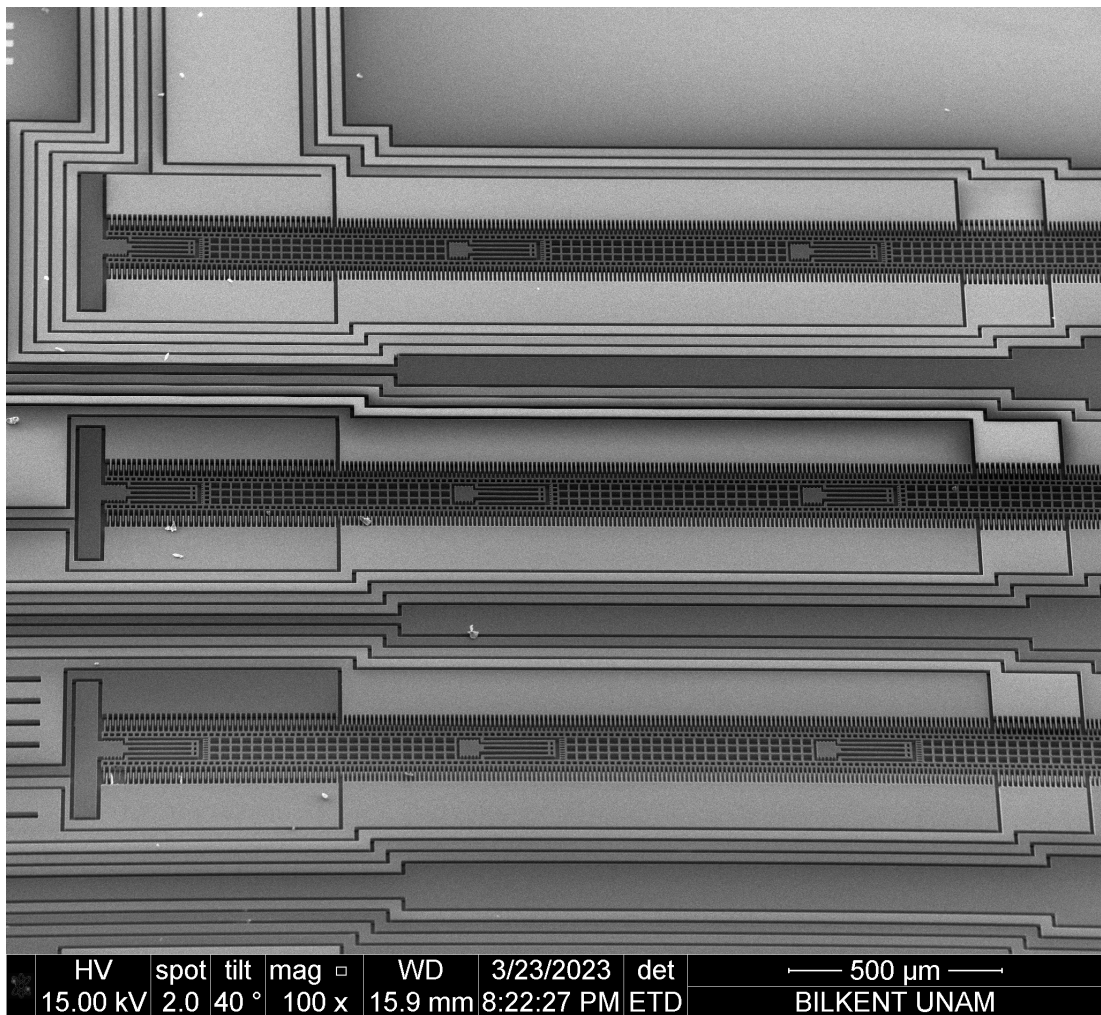


Figure 3.9: Portion of the final device die shown under SEM.

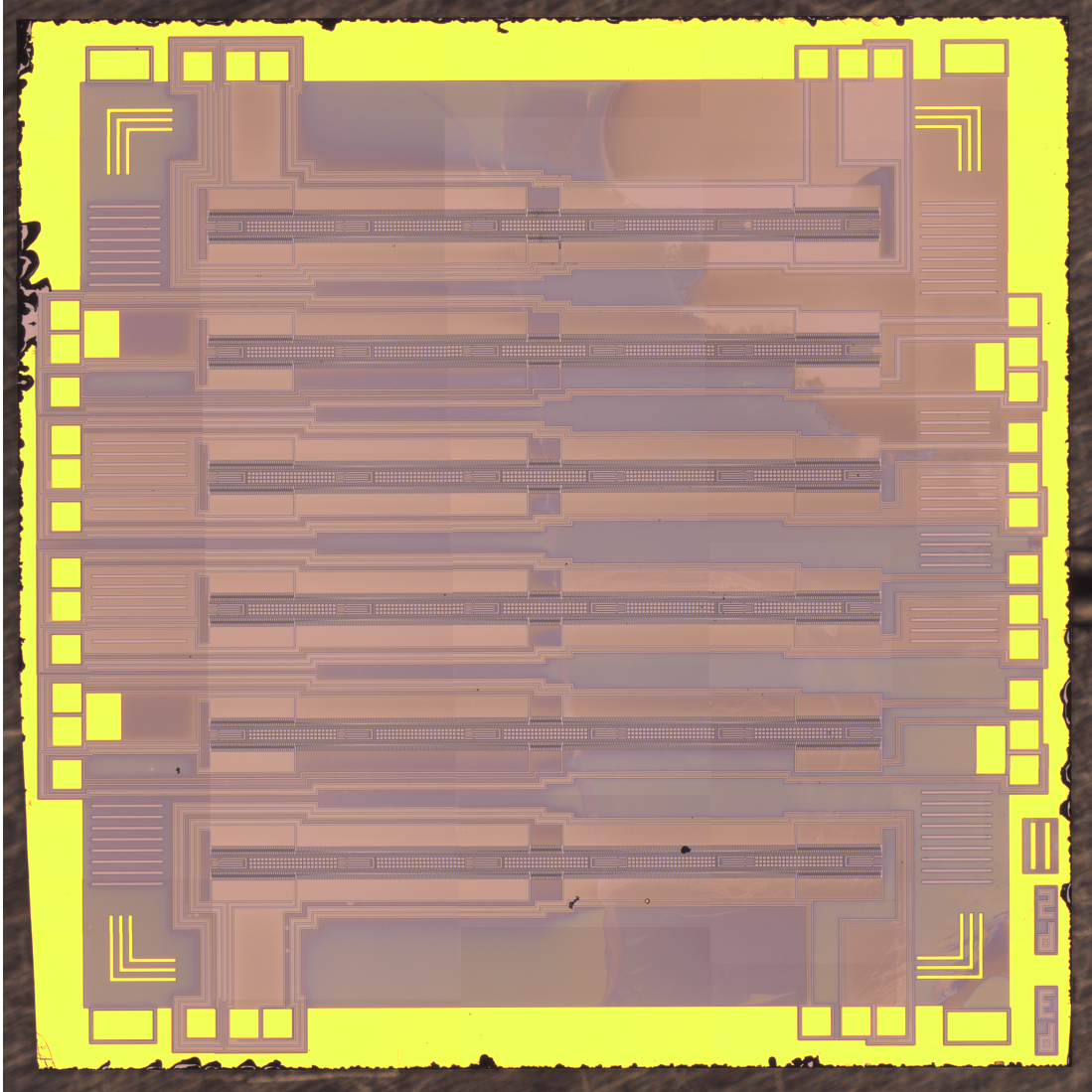


Figure 3.10: Optical microscope photo of sensor die.

## 3.2 Cavity

Two different methods are used in order to fabricate the acoustic cavity. The first few cavities are fabricated using resin 3D printing. For this method, the cavity is modelled in 3D using OpenSCAD. The cavity is formed with a square shape where the outside width is 5.3mm. This width is dictated by alignment markers, which are patterned onto the die metal layer. The inner width is nominally 5mm, giving a minimum wall thickness of 0.15mm, however the inner width can be shrunk further to change the resonant frequency of the cavity. The cavity depth is fixed at 0.5mm. The finalized 3D model can be seen in Figure 3.11 The actual printing of the cavity is outsourced to UMRAM facilities, where a suitable 3D printer is available. Stereolithography (SLA) printing is preferred over fused deposition modeling (FDM) because of the smaller features that can be resolved and the higher stiffness of the resin material that is used. The first cavities are printed with a large handle on the back for support during printing, shown in Figure 3.12, however this is found not only to be unnecessary, but also removing the handle from the cavity is found to be difficult using hand tools. Therefore the cavities that are used on working sensor dice are printed directly with no support material included, which is shown in Figure 3.13. The Z height of the overall sensor after these cavities are attached to the sensor die means that the ceramic LCC package lid cannot be closed directly over the sensor. Therefore, a CNC milled aluminum lid is used, which allows for taller dice to be placed into the package.

The second type of cavity that is used is fabricated by etching from a silicon wafer. 380 $\mu$ m thick wafers are used to ensure that the overall sensor stackup can fit into the ceramic LCC package while still allowing the original lid to be closed over the package. Similar to the fabrication of the sensor die, the wafers are first cleaned with acetone, isopropyl alcohol and water. For these wafers piranha cleaning is not used. Then, the wafers are coated with Microchemicals AZ 4533 resist, using the procedure detailed in Appendix B. This photoresist is formulated with a high viscosity, allowing two layers of resist to be coated, giving a film thickness of 7.6 $\mu$ m [32]. This resist layer needs to be thick for two reasons. First,

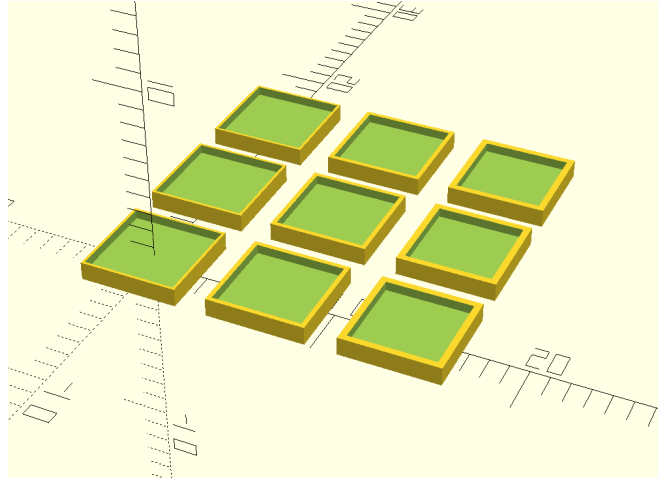


Figure 3.11: CAD model of 3D printed cavities showing a range of inner dimensions

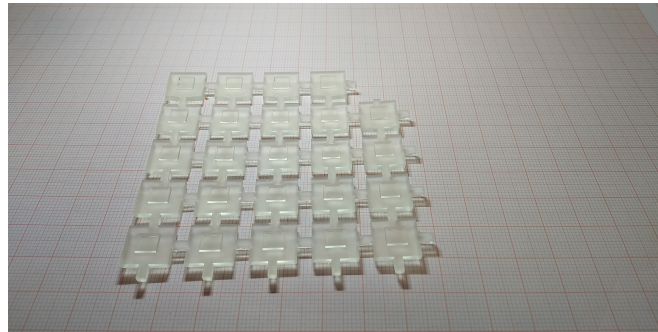


Figure 3.12: First iteration of 3D printed cavities with large handle on back side

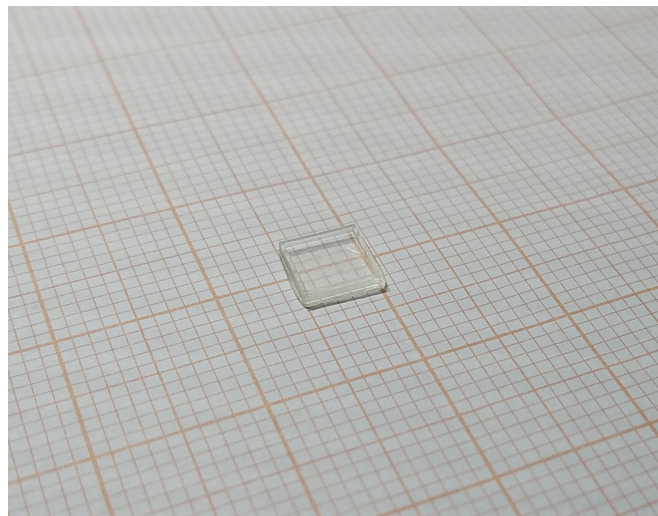


Figure 3.13: Second iteration of 3D printed cavities, printed directly with no support structures

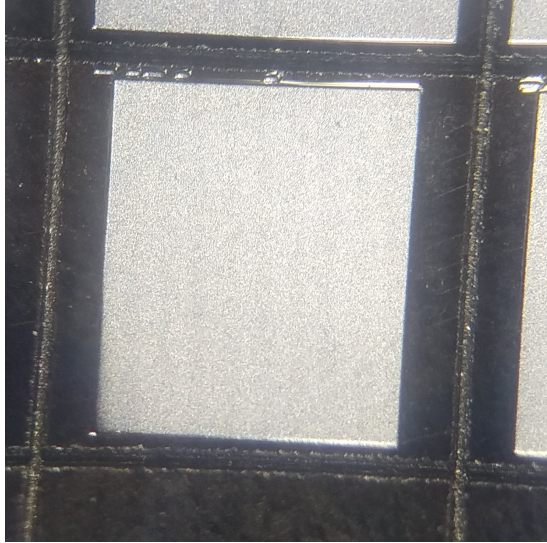


Figure 3.14: Single silicon cavity viewed through an optical microscope.

the small amount of  $O_2$  plasma in the ICP slowly erodes the resist layer during long etch processes. This can typically be solved with a metal hard mask [33], however, an insulating layer will also be needed after processing is complete. The resist is not stripped after etching and also serves as an insulator between the cavity and the sensor die.

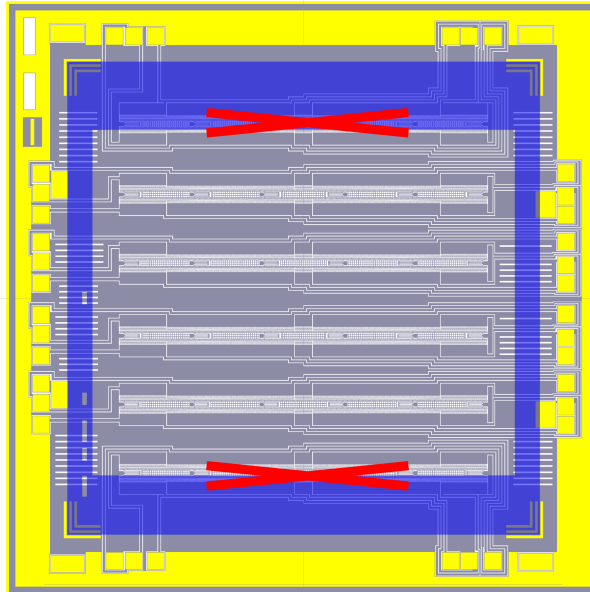
On a single wafer, many cavities with different cavity lengths are drawn. This allows for manual selection of the appropriate cavity frequency for any particular die despite any process variations. The mask is exposed with soft contact, since the smallest features are on the millimeter scale. The cavity is etched using a DRIE process similar to that used in the device layer, however the number of etch and deposition cycles are increased to 100 and the power levels are increased to compensate for the greater area. Overall, an approximately  $100\mu\text{m}$  deep cavity. The depth is measured with an optical microscope using the same technique described in Section 3.1.2. The focus knob of the optical microscope in the cleanroom has graduations on the handle, where each tick moves the focal plane by  $4\mu\text{m}$ , so the height can be estimated by counting the number of ticks necessary to bring the target into focus. Finally, the individual dice are separated with a dicing saw.



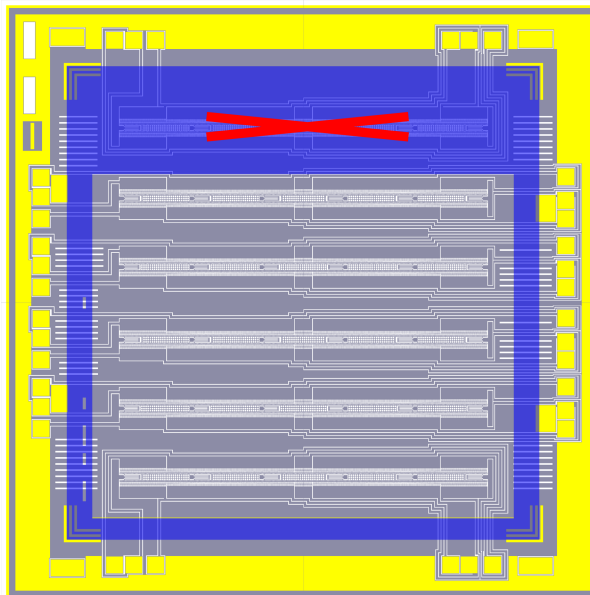
Figure 3.15: Wafer of silicon cavities after dicing.

Table 3.1 shows the sizes of the cavities which are fabricated, along with their theoretical resonant frequencies in room temperature air (assuming  $c_{gas} = 345\text{m/s}$ ). The outer dimensions are held constant as a 5.3mm square. The inner width is held constant at 5mm, and the length is changed according to the table. As the cavity length gets smaller, the walls of the cavity begin to interfere with the resonators, physically blocking them, as shown in Figure 3.16a. In the table, the cavities marked "offset" compensate for this problem by shifting the cavity within the die, such that only one resonator is blocked, as shown in Figure 3.16b. This allows for all three pairs of resonators to be selected and used, while sacrificing one unused resonator.

Figure 3.16: Benefit of offset cavities on selection of resonators within the sensor die.



(a) Symmetrical acoustic cavity superimposed onto sensor die. Two resonators are blocked by the cavity wall.



(b) Offset acoustic cavity superimposed onto sensor die. By shifting the cavity within the die, only one resonator is blocked.

Table 3.1: Fabricated cavity dimensions and corresponding resonant frequencies at  $c_{gas} = 345\text{m/s}$ .

Cavity length (mm)	$f_0$ (kHz)	Cavity length (mm)	$f_0$ (kHz)
5.0	34.500	4.2	41.071
4.9	35.204	4.1 (offset)	42.073
4.8	35.938	4.0 (offset)	43.125
4.7	36.702	3.9	44.231
4.6	37.500	3.8	45.395
4.5 (offset)	38.333	3.7	46.622
4.4 (offset)	39.205	3.6	47.917
4.3	40.116	3.5	49.286



Figure 3.17: Probe station test setup showing Keithley 2400 SMU being used to test for shorts.

### 3.3 Post-fabrication processing

The dice which are successfully released are taken out of the cleanroom and tested electrically in the probe station. Here, due to the limited number of probes, only one resonator can be tested at a time. For each resonator, the impedance between stator electrodes and the proof mass is first measured. Ideally, this should be a complete open circuit, however if the die is contaminated by dust or some other chemical residue, this can cause a short circuit between the proof mass and the stator. If impedance of less than  $10\text{M}\Omega$  is measured, this is assumed as a short in this instance. For very low impedances, the proof mass voltage can be present on the terminals causing damage to the frontend circuitry. Higher impedances will not cause a catastrophic failure but can saturate the charge amplifiers in the frontend with a constant DC current flow. When a short is detected, a Keithley 2400 source-measure unit (Cleveland, Ohio, USA) is used to pass a controlled current through the device to burn out whatever is in between the electrodes.

Devices which pass the short test are then tested for movement of each resonator. A separate PCB containing the front-end circuitry for just one resonator 3.18 (explained in detail in Chapter 4) is attached to the probes, and the Zurich

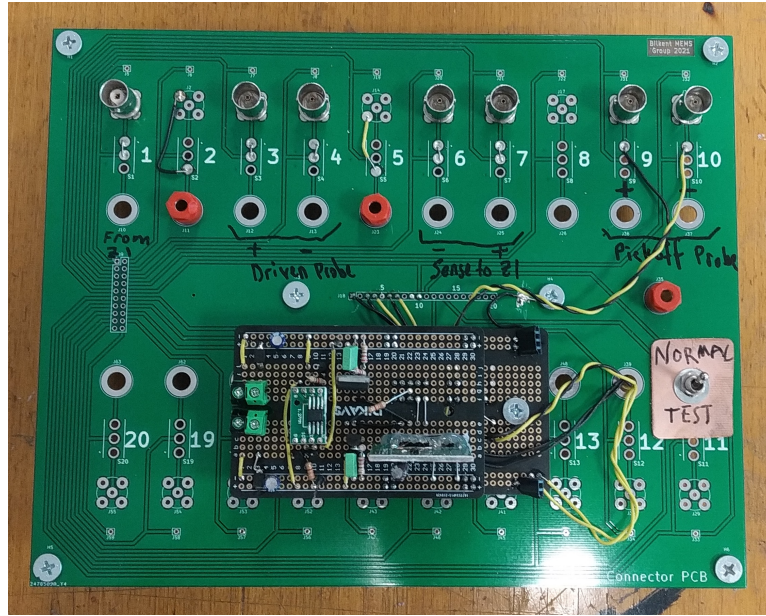


Figure 3.18: Readout board which is used with the probe station.

Instruments HF2LI (Zurich, Switzerland) is used to run frequency sweeps for each resonator. These frequency sweeps can reveal further defects in the dice, such as stuck resonators (which appear as no response) or dysfunctional stator electrodes (which affect the shape of the resonant peak, since the resonators are only driven from one end). In addition, this process reveals the resonant frequencies which are available in the die. Out of the resonators available, a pair is selected in order to get the best possible response. Using the resonant frequency of this pair, an appropriate acoustic cavity is then selected, which will be attached to the sensor die later in the process. A table of available cavity sizes with their frequency response in room temperature air is given in Table 3.1.

# Chapter 4

## Experimental Procedure

In this chapter, the overall system used for testing the fabricated devices are shown. This includes the readout electronics and the instruments which interface to them. In addition, the general procedure for experiments which are carried out in this thesis are described.

The gas sensor system operates using a set of source and detector resonators. Both resonators need to be controlled independently, tuning them to the appropriate frequency determined by the acoustic cavity. As previously shown in Figure 1.5b, the point where all three transfer functions overlap will yield the greatest amplitude. By continually tuning the resonators to follow this peak, the acoustic response of the cavity can be measured. Observing the point of peak response also increases the amplitude of the return signal, which serves to improve SNR. Figure 4.1 shows the overall block diagram of the gas sensor system, including the readout electronics.

The sensor dice which pass through the initial test procedure are taken out of the probe station and attached to a LCC-44 ceramic package. A silver-filled conductive epoxy is used to attach the sensor die in order to make an electrical connection to the handle layer. The sensor die is then wire bonded to the ceramic

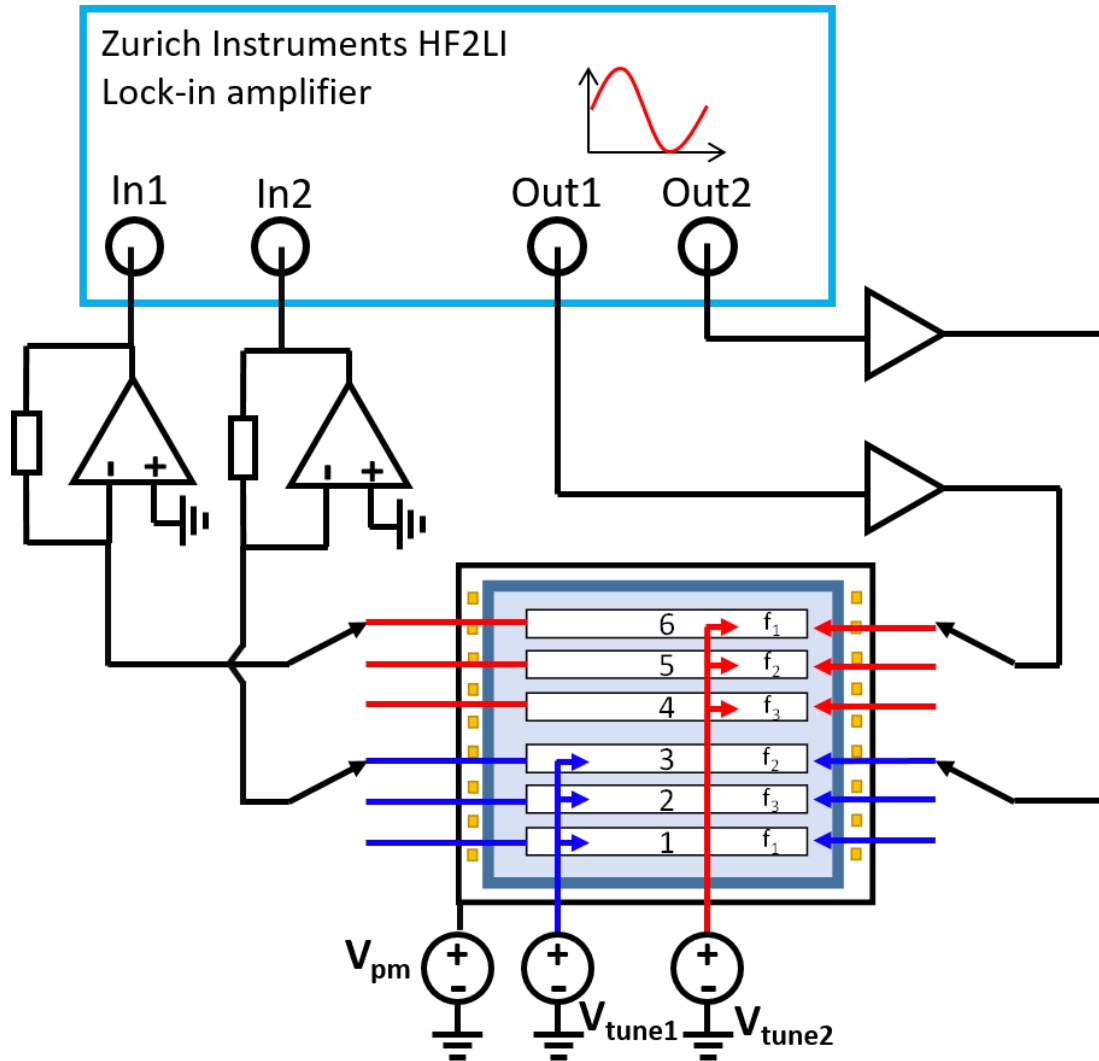


Figure 4.1: High-level diagram of experiment setup.

package, with an additional wire bond from the package floor to the  $V_{PM}$  terminal. The wire bonded package is then soldered to a custom daughterboard PCB (Figure 4.2), which allows sensors on the main PCB to be swapped. A heater is patterned underneath the sensor package for future testing of temperature coefficients, however this feature is not used within this work. Finally, the selected acoustic cavity is manually placed on top of the sensor die. Alignment markers are located on the sensor die to position the cavity correctly. Once the cavity is placed, an insulating silicone based epoxy is used to bond the cavity to the sensor die by placing two drops of epoxy on either end. This ensures that epoxy

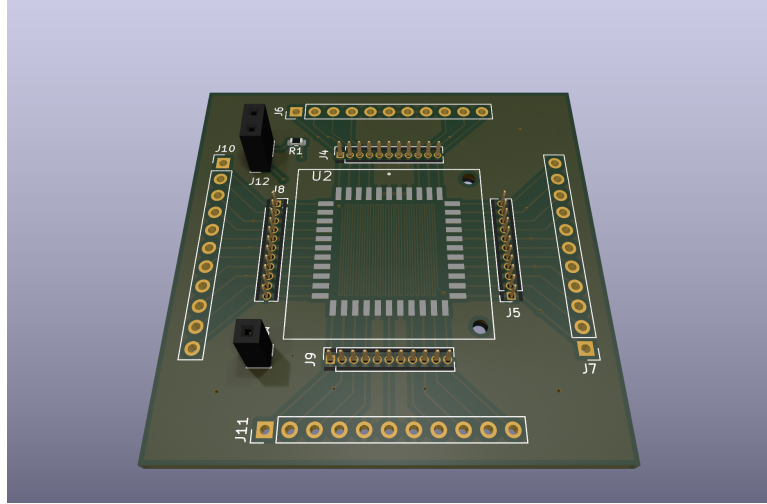
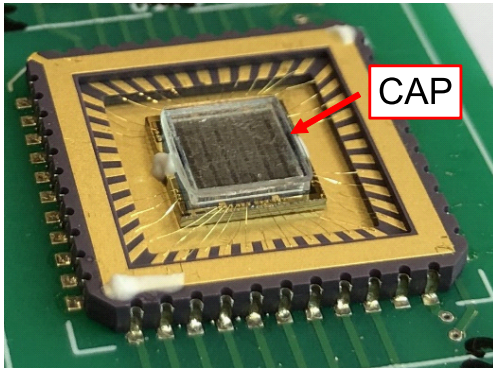
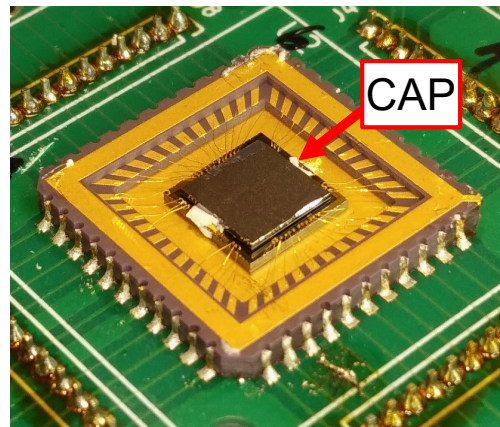


Figure 4.2: 3D render of unpopulated gas sensor daughterboard.

will not touch any of the moving structures, and also allows the test gas to flow in and out through the sides. After the cavity is attached, the sensor is ready for testing, as can be seen in Figure 4.3.



(a) 3D printed cavity.



(b) Silicon cavity.

Figure 4.3: Completed sensor dice ready for testing.

The gas sensor is implemented using off-the-shelf instruments, with the majority of the functionality provided by a Zurich Instruments HF2LI (Zurich, Switzerland) lock-in amplifier . Within this instrument, an oscillator drives the source resonator with an AC signal, and the return signal from both the source and

detector resonators are demodulated using the same oscillator. A DC signal corresponding to the peak amplitude is thus obtained. Additionally, a Keithley 2400 (Cleveland, OH, USA) source-measure unit provides a constant  $V_{pm}$  to the sensor, and two channels of a Keysight N6705A (Loveland, CO, USA) power analyzer are used to provide the tuning voltage to each resonator. These instruments are controlled by Python code, interfacing to the HF2LI over USB and the other instruments over GPIB. This software automatically controls each instrument to run the desired experiment without user intervention.

In order to interface these instruments to the gas sensor die, a custom front-end PCB is designed. Figure 4.4 shows this PCB, while the overall setup is shown in Figure 4.5. The daughterboard attaches onto this PCB. Switches are provided to select between the different resonators on the die, and the signals are routed to the frontend electronics on board. The individual components are described in detail in Section 4.1. In addition, a passive connector PCB is used to route signals onto a single ribbon cable which is used to connect to the main PCB.

## 4.1 Frontend Electronics

Figure 4.6 shows the circuitry needed to interface to each resonator. From an electrical perspective, the source and detector resonators can be considered equivalent. For both of these resonators, a differential buffer excites the drive electrodes, and a charge amplifier conditions the signal coming from the sense electrodes. This signal is then further amplified by an instrumentation amplifier with differential output. This signal returns to the lock-in amplifier to be demodulated. The tuning electrodes are not associated with any electronics on board, and are driven directly by the external DC sources. However, the tuning signals, as well as  $V_{pm}$ , are filtered to suppress AC interference, with a simple RC low-pass filter.

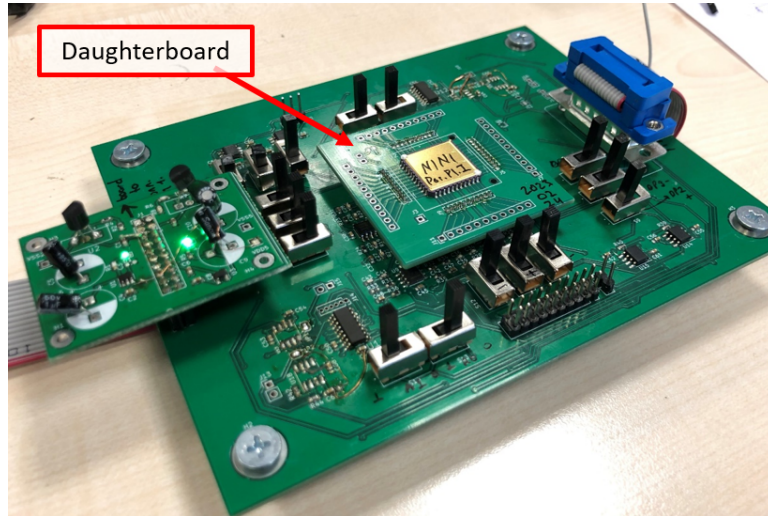


Figure 4.4: Close-up photo of PCB showing daughterboard attached on top.

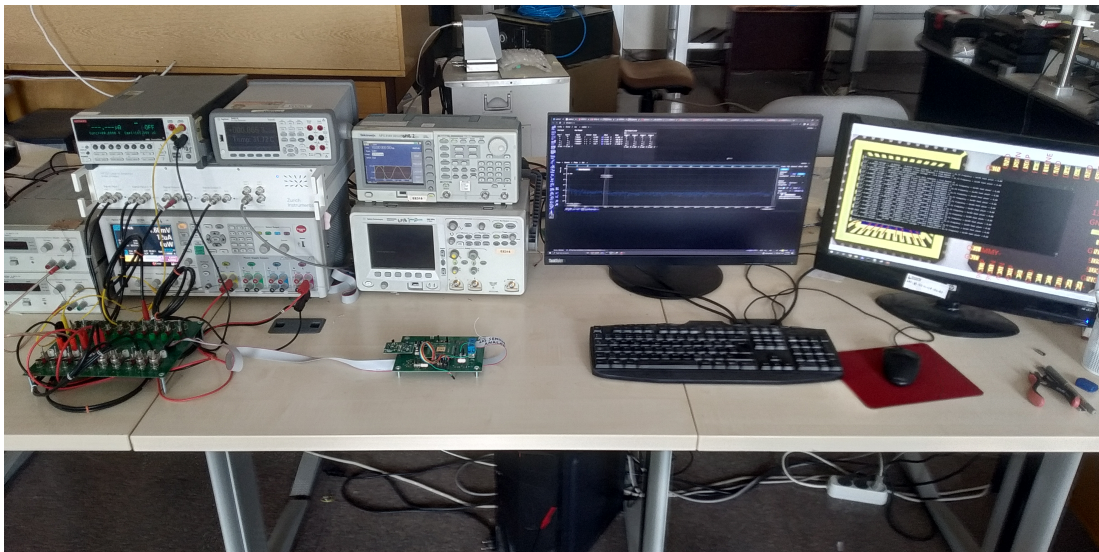


Figure 4.5: Photo of overall test setup including test PCB.

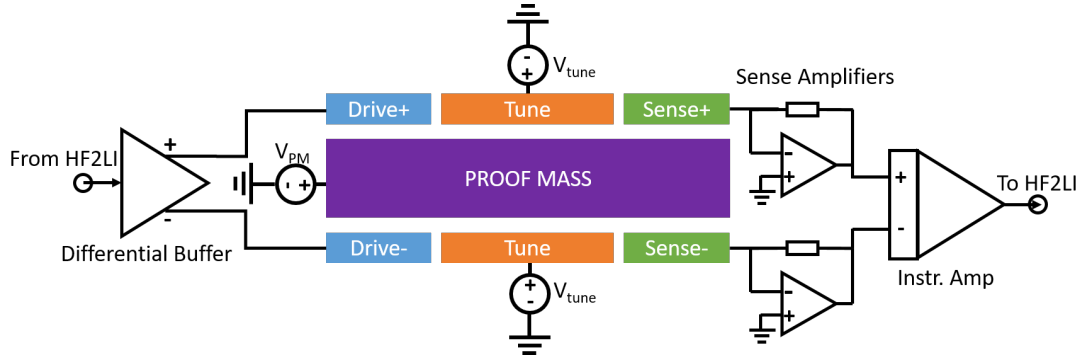


Figure 4.6: High-level schematic of single resonator with associated readout electronics.

### 4.1.1 Signal Switches

As described in Chapter 3, each die contains three matched pairs of resonators which are not needed simultaneously. Therefore, only two sets of drive amplifiers are added onto the PCB, and switches are used to select the appropriate resonators. On the source side, the buffer output is directly switched between each set of drive electrodes using a total of six SPDT mechanical switches, with unused drive electrodes being tied to  $V_{pm}$  to disable them. However, on the detector side, maintaining signal integrity mandates a different structure. The sense amplifier has a very high gain, and as will be described in 4.1.3, its noise is highly dependent on the parasitic capacitance at the input. Therefore, in order to keep the path from electrode to amplifier as short as possible, each receive transducer is given its own permanently connected pair of sense amplifiers. Six SPDT mechanical switches allow the drive electrodes of the detector, which are not necessary in normal operation, to be connected to the sense amplifier as well, for extra gain. A multiplexer is implemented at the output of these sense amplifiers, using two ADG1209 (Analog Devices) dual SP4T multiplexer ICs. Three differential pairs of signals are switched and the fourth input is left disconnected. The digital input for this IC is also provided using mechanical switches for manual adjustment.

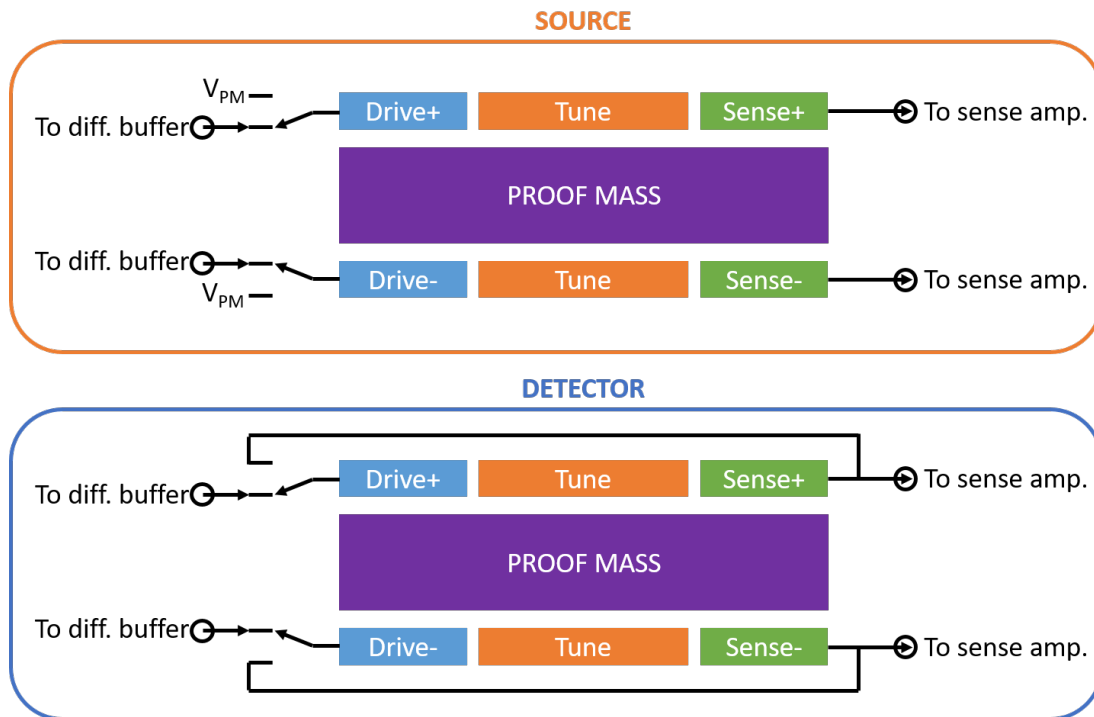


Figure 4.7: Schematic of multiplexing switches, showing signal connections to source and detector transducers. Tune voltage connections are made directly and not shown here.

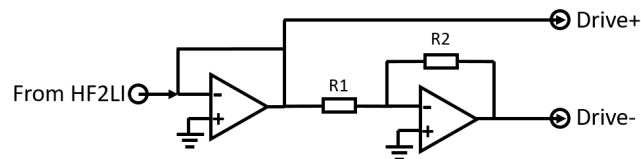


Figure 4.8: Schematic of differential buffer amplifier.

### 4.1.2 Differential Buffer

Figure 4.8 shows the differential buffer circuit for drive electrodes. The stimulus signal coming from the lock-in amplifier is single ended, however this must be converted to a differential signal in order to drive the resonator from both ends. For this purpose two op amps are used to buffer the signal at +1 and -1 gain respectively. In theory, the unity gain buffer could be eliminated without any loss in signal integrity. However, this op amp is included in order to protect the HF2LI's outputs against the high bias voltages present on die. In any situation

where this high voltage leaks onto the drive electrodes, the op amp will absorb the leakage current, and its ESD diodes will clamp the voltage, preventing it from appearing on the lock in amplifier's terminals under any circumstances. By setting all resistors to an identical value, an unity gain is obtained for both stages - in the real circuit  $1\text{k}\Omega$  is used. An optional  $50\Omega$  termination resistor is included on the PCB for the buffer input, however during testing of the electronics it was revealed not to be necessary. The differential buffer can be implemented using any one of many generic op amps with identical footprint. In the circuit the TL051 (Texas Instruments) is used.

### 4.1.3 Sense Amplifier

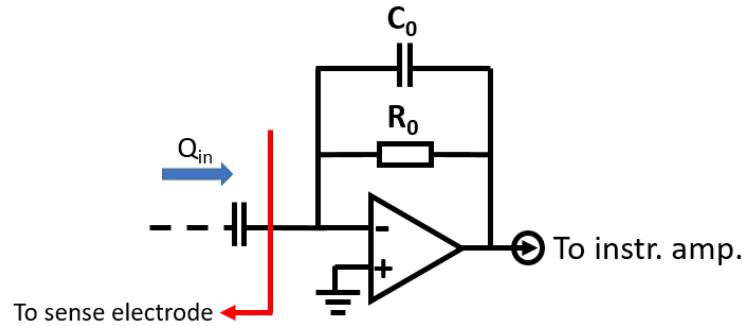


Figure 4.9: Schematic of sense amplifier showing both resistive and capacitive feedback. Circuit topology changes based on which component dominates the resulting impedance.

The sense amplifier converts the current coming from the sense electrodes into a voltage with a very high transimpedance gain. For this stage, two topologies can be considered. When the impedance of  $C_0$  is much larger than  $R_0$ , the total impedance is resistive, forming the typical transimpedance amplifier topology. Considering the capacitive source impedance of the sense electrodes, this topology can have gain variation with frequency. In addition, the transimpedance topology can become unstable at high gain, requiring a parallel capacitor to stabilize the circuit.

Instead of the transimpedance topology, the sense amplifiers are configured as a charge amplifier. In this topology, ideally  $R_0$  becomes infinite and the gain is determined by the impedance of  $C_0$ . This way, the gain and phase response of the amplifier remains largely constant, with the voltage gain being set as  $G_V = C_s/C_0$ . However, the more important gain term is charge gain. Incoming charge is integrated with a constant term of  $C_0^{-1}$ . Considering that the sense electrodes output charge proportional to the derivative of displacement, shown in Subsection 2.2.3, the output voltage becomes proportional to the net displacement of the proof mass. In a real circuit some  $R_0$  is also required in order to ensure unity gain at DC. This way, the op amp's offset voltage and input bias current will minimally influence the output. For  $C_0$ , 0.5pF is used, and for  $R_0$  300M $\Omega$  is used. Assuming that the circuit will operate at 34kHz, the impedance of  $C_0$  is 9.362M $\Omega$ . Since  $R_0$  is an order of magnitude larger, it can be considered negligible, indeed the corner frequency is  $f_c = \frac{1}{2\pi RC} = 1061\text{Hz}$ , far away from the frequency of interest.

The sense amplifier is implemented using an OPA2322 (Texas Instruments) op amp. This op amp has sufficient bandwidth and input bias current to have negligible effect on circuit performance. It is especially notable for its noise performance compared to similar op amps, with a voltage noise density of  $v_n = 7\text{nV}/\sqrt{\text{Hz}}$  and a current noise density of  $i_n = 0.6\text{fA}/\sqrt{\text{Hz}}$ , referred to input [34]. Based on these parameters, the noise of the sense amplifier circuit can be calculated. The primary noise sources are shown in Figure 4.10 and can be summarized as follows:

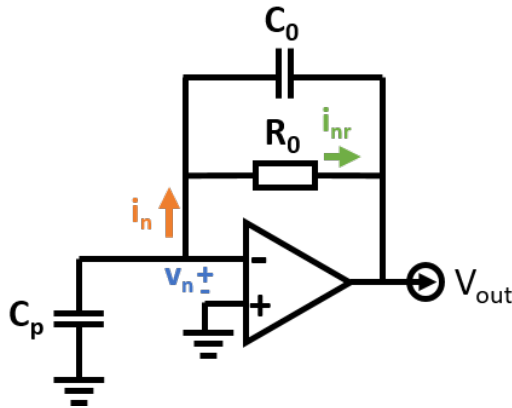


Figure 4.10: Schematic of sense amplifier with noise sources highlighted.

- The current noise of the op amp is amplified by  $C_0$ , converting it to a voltage.
- $C_0$  and the parasitic capacitance  $C_p$  form a non inverting amplifier stage, amplifying the voltage noise of the op amp by  $1 + \frac{C_p}{C_0}$ .
- The current noise of  $R_0$  is amplified by  $C_0$ , converting it to a voltage.

The equation for each noise source and its calculated contribution is given in Table 4.1, taking the frequency as 34 kHz as before. For the parasitic capacitance, an approximate value of 30pF is estimated, taking into account an approximate 20pF capacitance within the die to  $V_{pm}$ , as well as 3pF added by the ceramic package, with the rest of the estimated capacitance coming from PCB trace capacitance. Although noise performance is not as important in the proof of concept stage demonstrated in this work, a low noise front-end is important to increase the sensitivity of the sensor. With added noise, it becomes more difficult to find the peak amplitude, and noise can thus be directly translated into an erroneous measurement in a functional sensor.

Table 4.1: Calculation of notable noise sources within sense amplifier circuit.

Noise source	Equation	Contribution
Op amp $i_n$	$e_1 = \frac{i_n}{j\omega C}$	5.62nV/ $\sqrt{\text{Hz}}$
Op amp $v_n$	$e_2 = v_n \cdot \left(1 + \frac{C_p}{C_0}\right)$	518.5nV/ $\sqrt{\text{Hz}}$
$R_0 i_n$	$e_3 = \sqrt{\frac{4kT}{R}} \cdot \frac{1}{j\omega C}$	67.0nV/ $\sqrt{\text{Hz}}$
Total noise	$\sqrt{e_1^2 + e_2^2 + e_3^2}$	522.84nV/ $\sqrt{\text{Hz}}$

#### 4.1.4 Instrumentation Amplifier

As the signal passes out of the sense amplifiers and through the multiplexers, an AD8228 (Analog Devices) instrumentation amplifier is used to apply additional

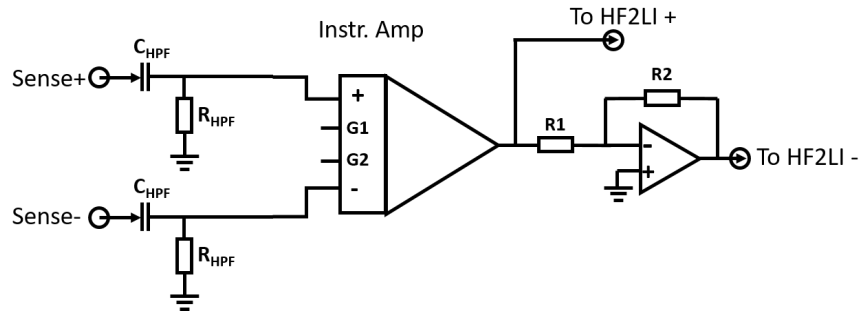


Figure 4.11: Schematic of instrumentation amplifier circuit.

gain to the signal. This amplifier provides a user settable gain of x10 or x100, in the current implementation x10 gain is selected by leaving the G1/G2 pins disconnected. After the instrumentation amplifier, the signal is converted from differential to single ended. Therefore, a second op amp TL051 is added in an unity gain inverter configuration to create a pseudo-differential signal, with  $R1 = R2 = 1k\Omega$ . Although the common mode rejection of the system is impaired in this way, the majority of the interference within this system is introduced in the cable going from the PCB to the lock-in amplifier, and this interference is readily rejected by the pseudo-differential signal obtained, therefore the loss in common mode rejection is not considered to be a major problem. A secondary benefit of the instrumentation amplifier stage is that the cable to the lock in amplifier is a capacitive load, and driving it with a secondary set of amplifiers more suited to the task prevents any issues with stability within the sense amplifier.

## 4.2 Experiment Procedure

In this work, every gas sensor that is fabricated is tested in an air environment, with humidity and temperature not being controlled. The primary sensing element within the described sensor is the acoustic cavity, therefore the main objective of the experiments carried out is to prove that the system is capable of measuring the acoustic properties of this cavity. By demonstrating that the acoustic cavity can be measured, a proof of concept is achieved. One source of

coupling that is not dependent on the acoustic cavity that could show a false result is mechanical coupling through the handle layer, while electrical feedthrough could also cause coupling between the source and detector resonators. Therefore, in order to show conclusively that the observed response is due to the acoustic cavity, each experiment is repeated twice, one with the acoustic cavity not attached, and another with the acoustic cavity attached. Each test is conducted in an ambient air environment, with a pressure of 1 atm.

The HF2LI has a built in frequency sweep mode which is used for all experiments. A frequency range is selected that includes the resonance peak and its tails, for example for a 34 kHz resonator 32 to 36 kHz would be swept. The instrument also allows multiple sweep results to be overlaid on top of one another. This feature is used for the first experiments that were carried out. The power supply voltages are varied by hand in order to set the tuning frequency, and for each pair of  $(V_{ts}, V_{td})$  one sweep result is recorded. At this point, the obtained sweep results show very small resonance peaks. It is observed that a large amount of electrical feedthrough is added to the measured result, obscuring the resonant peak. The feedthrough response can be isolated by setting  $V_{pm}$  to zero and running another sweep. This ensures that the transducers will be unable to move from the applied AC signal. From this sweep, it is observed that the feedthrough presents itself as a capacitive coupling effect, with magnitude proportional to frequency, which suggests parasitics outside the sensor die as the main culprit. In any case, the electrical feedthrough is subtracted from all of the previous sweep results in order to obtain a purely mechanical frequency response curve.

In order to obtain the acoustic resonance frequency, custom software written in Python is used to vary the tuning voltages and run a sweep at each step, recording the source and detector frequency response. The code for this tool is given in Appendix C. This tool generates a tuning path, shown in Figure 4.12.  $V_{pm}$  is set manually, as well as the AC signal applied to the source resonator, in order to permit customizations to the running experiment.  $V_{pm}$  is chosen as 60V, based on observations made during post-fabrication testing. It is discovered that many of the devices which are tested start to show an effect similar to dielectric breakdown as  $V_{pm}$  exceeds this value, likely due to a contaminant left

over from the fabrication process. In addition, as the difference between the tune voltages and  $V_{pm}$  starts to exceed 100 V, the risk of arcing increases, threatening catastrophic damage to the device.

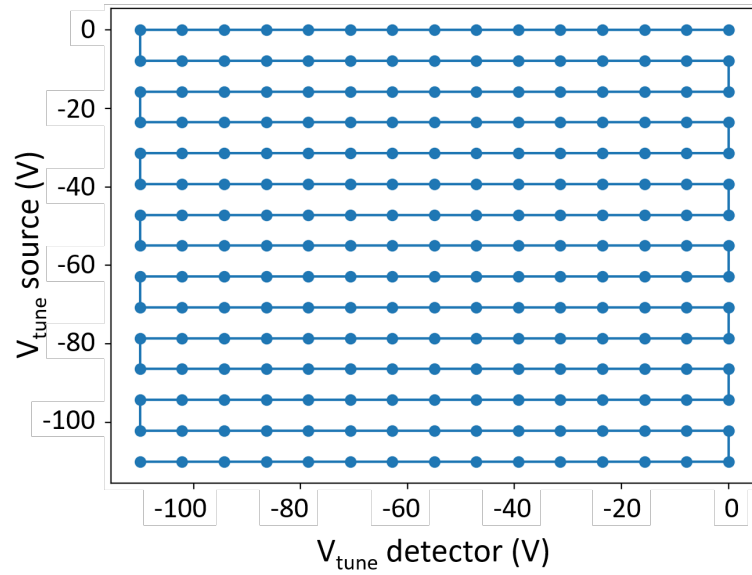


Figure 4.12: Tuning path showing the voltage applied to each resonator with respect to ground.

Finally, in order to verify the speed of sound measured within the device, a separate setup is needed to measure the speed of sound externally. For this, an Arduino based setup is constructed, shown in Figure 4.13. An off-the-shelf ultrasonic distance sensor is used to measure the distance within a metal enclosure with known dimensions. This ultrasonic sensor is calibrated to measure accurately when  $c_{gas} = 345m/s$  and deviations in the speed of sound from this value also cause deviations in the measured distance. By continually measuring the distance with this sensor, a comparison can be made between the known distance and the measured distance to get the actual speed of sound.

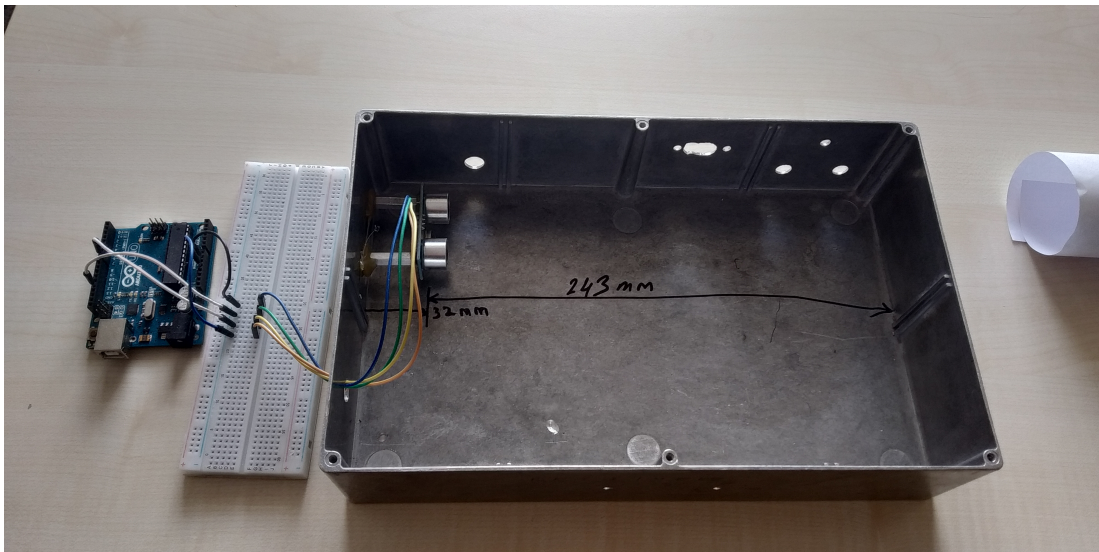


Figure 4.13: Arduino based speed of sound measurement setup.

To summarize, the experiment that is performed on these dice consists of a sequence of frequency sweeps over the same frequency range, while the tuning voltage applied to each resonator is changed. Therefore, an overall characterization of the system response can be obtained. The HF2LI lock in amplifier generates a stimulus signal which is buffered and applied to each device, and then the output is amplified by a readout circuit and returned to the lock in amplifier input. Custom Python code controls the process and automatically characterizes the device.

# Chapter 5

## Experimental Results

### 5.1 Results

In this chapter, the experimental procedure shown in the previous chapter is applied to the sensor dice and the results are provided. The obtained results are analyzed to make a conclusion as to the performance of the proof of concept. Finally, some further paths for subsequent study are detailed.

Two devices are examined in this thesis, which are selected by testing the best performing resonators on each die. It is important that a pair of resonators that are fully functional can be found to run the subsequent experiments under near-ideal conditions. These devices are identified by a unique code that is assigned to every die within the fabricated wafer based on its physical position. Using this coding system, the dice that are examined are called N1N1 and N4P1. N1N1 is of the first parallel plate type, meaning that the source resonators have a lower set of frequencies, and the detector resonators use the parallel plate actuators. In contrast, N4P1 is of the first comb actuator type, making it one of the simplest devices that were fabricated.

For both devices, it is necessary to take into account electrical feedthrough when analyzing the results. The electrical feedthrough is a known coupling effect and can be compensated by taking a measurement at  $V_{pm} = 0V$  and subtracting it from all other measurements. When working with uncompensated data, the electrical feedthrough means that any measurements based on the peak such as resonance frequency and quality factor will be inaccurate. An example sweep affected by electrical feedthrough is shown in Figure 5.1, while the same data with compensation is shown in Figure 5.2. All results presented in this thesis are shown with electrical feedthrough compensation already applied.

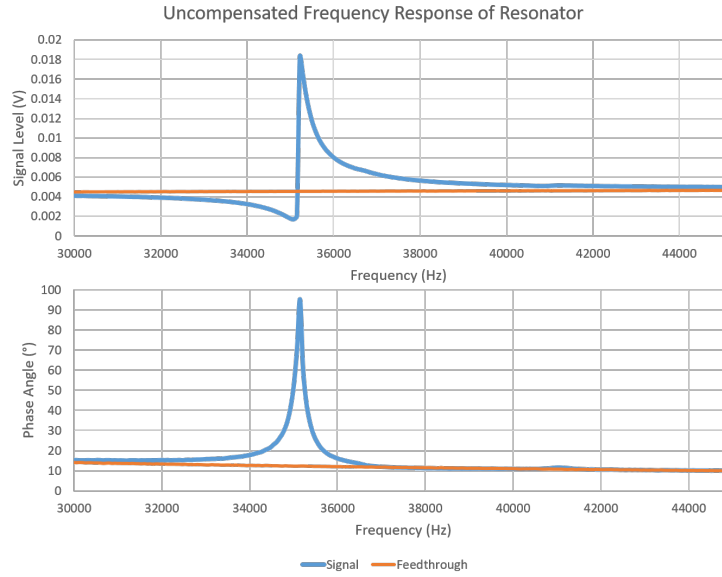


Figure 5.1: Example sweep result from die N4P1 showing an uncompensated result as well as the electrical feedthrough that is measured separately.

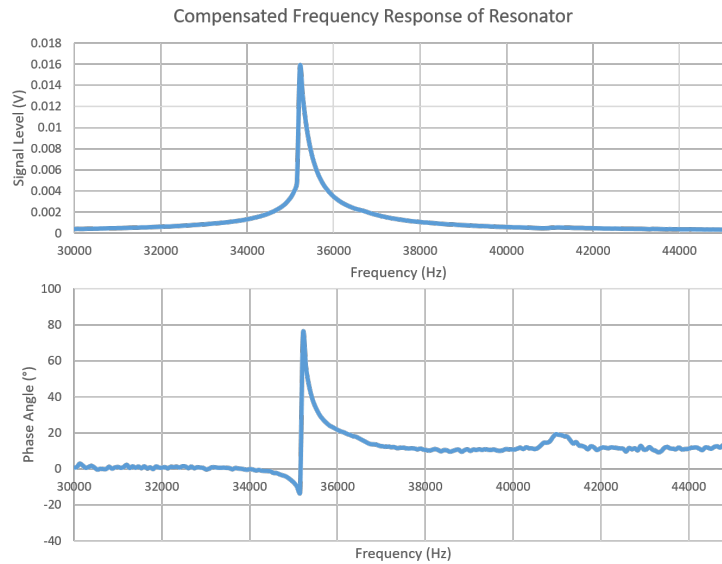


Figure 5.2: Sweep result from die N4P1 with electrical feedthrough subtracted.

### 5.1.1 N4P1

Due to its simpler construction, N4P1 is the first device that is tested. Based on the numbering scheme shown in Figure 2.21, resonators 3 and 5 are found to be the best functioning pair, with a resonant frequency of approximately 36.8 kHz. The nominal frequency for these resonators was determined as 33.6 kHz, showing that the fabrication process has introduced a significant frequency shift into the resonant frequencies of the devices. Before the family of curves test is applied, the tuning response of the resonators is examined, shown in Figure 5.3. The tuning curve is obtained by varying the tuning voltages by hand and recording the resonant frequency for each voltage. The tuning voltages on the x axis is shown as the voltage on the stator, meanwhile  $V_{pm}$  is held constant at 60 V. The tuning effect is dependent on the difference between these two voltages. Applying a 2nd order polynomial fit to the tuning curve reveals a  $R^2$  of 0.9976, showing that the theoretical  $V_{DC}^2$  dependence shown in Section 2.2.4 is accurate. The tuning range is determined as 1.8 kHz at 100 V tune voltage, also matching the theoretical results.

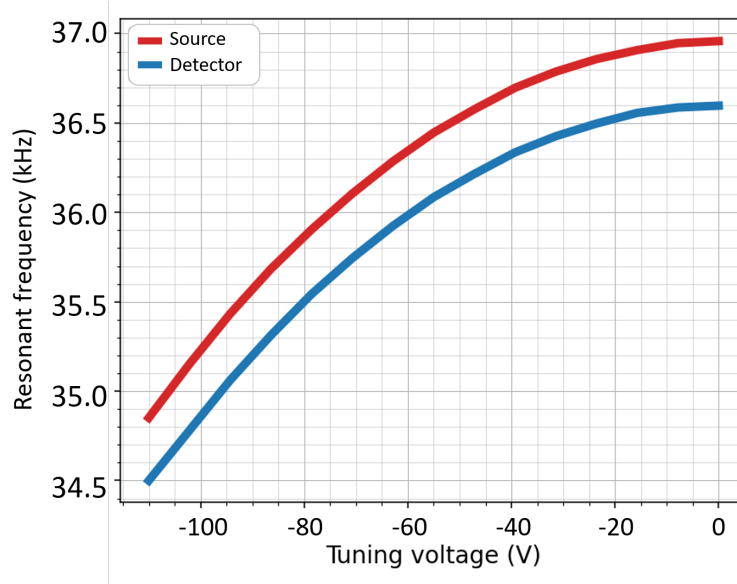


Figure 5.3: Tuning curve of N4P1 resonators, showing the

In addition, since N4P1 is the first die to be successfully fabricated and tested, the acoustic cavity response is tested manually. For this test, the plastic 3D

printed cavity is used since the silicon cavities were not available at the time. The cavity dimension is selected based on the tuning curve such that the cavity frequency lies in the middle of the tuning range. Based on this criterion, the best option is to use a 4.8mm cavity, with a calculated  $f_0 = 35938Hz$  (Table 3.1), assuming  $c_{gas} = 345m/s$ . The cavity is initially attached to the device and tuning voltages are manually adjusted until the strongest coupling is observed from the source resonator to the detector resonator. Figure 5.4 shows the frequency response of both resonators at this point. For this plot, both resonators are driven using their own drive actuators, and the coupling between resonators is not shown. The center frequency and the quality factor of the resonance is also calculated for each peak. When the maximum coupling is achieved, the frequency of the two resonators are spaced apart from one another, although there is still significant overlap due to the low Q factor of the resonance. This result was obtained with a more primitive version of the circuit shown in Chapter 4, therefore the peak coupling was likely affected by electrical response as well as mechanical response. For all subsequent tests the full circuit was used, taking care to ensure a flat frequency response.

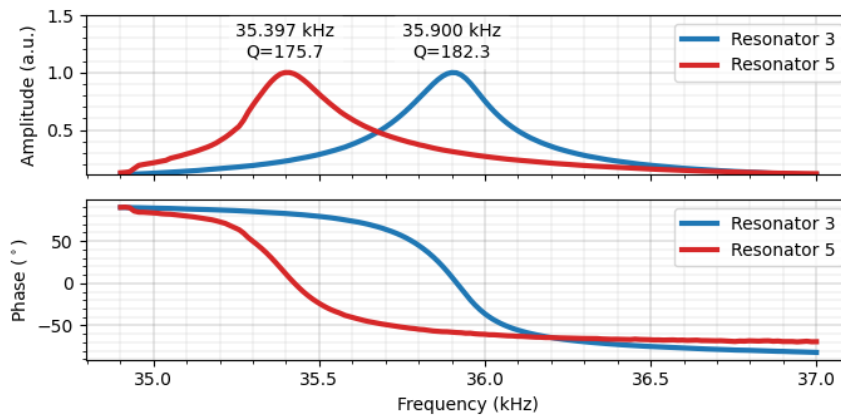


Figure 5.4: Individual frequency response of both resonators at the point of maximum coupling

In Figure 5.5, the source resonator is driven with different tuning voltages and the response obtained at the detector resonator is recorded, while the detector tuning remains constant. It can be seen that the peak amplitude is dropping as

the source tuning moves further away from the acoustic resonance peak. Therefore, it becomes more likely that the observed result is due to acoustic coupling and not any other effects. However, the definitive proof of whether this peak is due to the acoustic coupling or due to another resonant coupling is to observe the response without the acoustic cavity attached. Therefore, after taking one sweep with the cavity still attached, the cavity is then removed. Figure 5.6 shows the response in both cases. It can be seen that removing the acoustic cavity results in the resonant peak disappearing almost completely. Therefore, it is demonstrated that the acoustic coupling effect works.

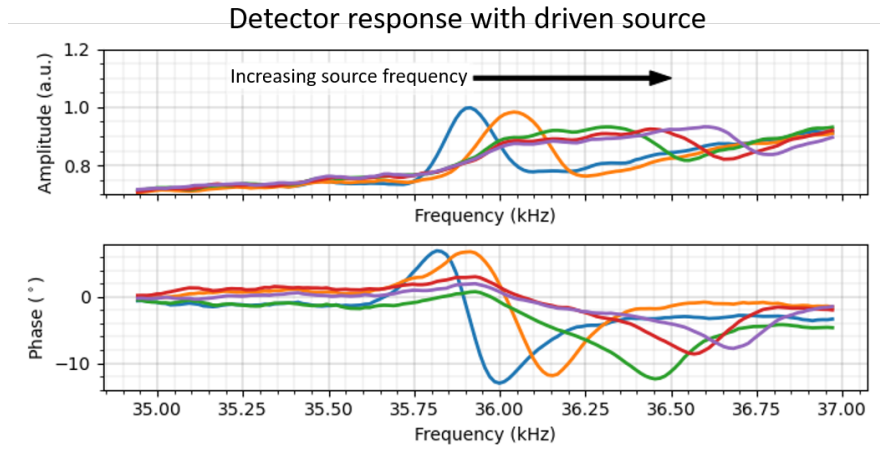


Figure 5.5: Overlaid plots of detector response while source tuning is varied shows coupling in more detail.

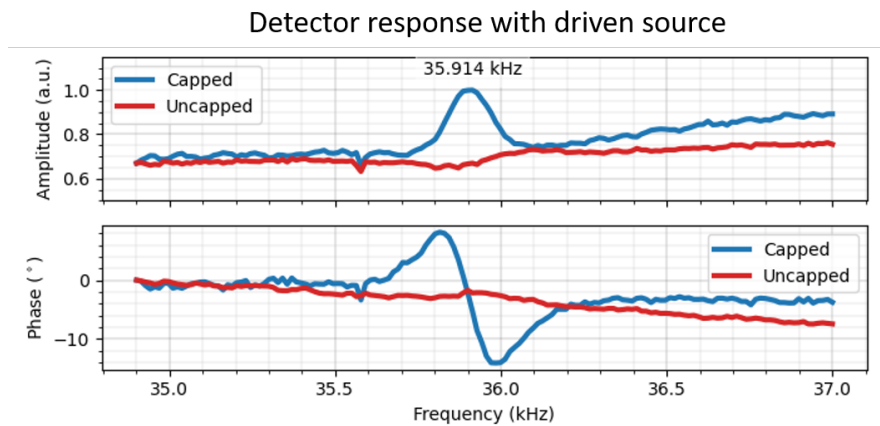


Figure 5.6: Response of detector resonator with source driven, with and without the acoustic cavity.

With these preliminary tests, the viability of the concept is shown, and the full test generating a family of curves is run on the device, using the main PCB shown in Chapter 4. The full graphs corresponding to these tests are given in Figure 5.10 and Figure 5.11. In Figure 5.7, an excerpt of these curves are shown. For each subplot, the tuning voltage of the source resonator is kept constant and the tuning voltage of the detector resonator is varied. It can be seen that the only signal observed in the detector is approximately  $20\mu V$  of white noise, with no readily apparent resonance peak. However, when the acoustic cavity is attached onto the sensor die, the result shown in Figure 5.8 are obtained. In this case, the resonance peak is clearly visible, with the strongest signal amplitude being measured as  $150\mu V$ . The resonance peak is affected by the tuning voltage of the detector resonator, getting weaker in amplitude as the resonant frequencies get further apart. Using the silicon acoustic cavity and the readout PCB, a cleaner result is obtained than the initial tests.

Based on the family of curves which are presented, it is possible to visualize the data in a clearer manner as well. Figure 5.9a shows a heatmap of the detector response in the case without an acoustic cavity, while Figure 5.9b shows a similar heatmap of the detector response when the acoustic cavity is attached. These heatmaps are generated from the family of curves by taking each individual sweep result and recording the peak magnitude in a new matrix. The magnitude is determined by subtracting the maximum voltage from the minimum voltage within the sweep. Afterwards, this matrix can be plotted as a 2D heatmap. From this heatmap, it can be seen that there is a strong coupling encountered whenever the source and detector electrodes are tuned to each other's resonance frequency. However, more importantly, the acoustic cavity response can be seen visually as some points along the diagonal have a stronger amplitude than others. For N4P1, the acoustic cavity response is not calculated, however this result is presented for N1N1.

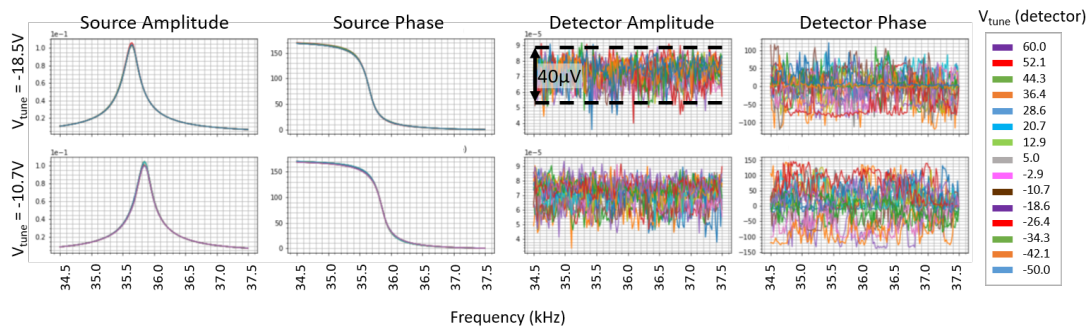


Figure 5.7: Excerpt of family of curves for N4P1 with no acoustic cavity.

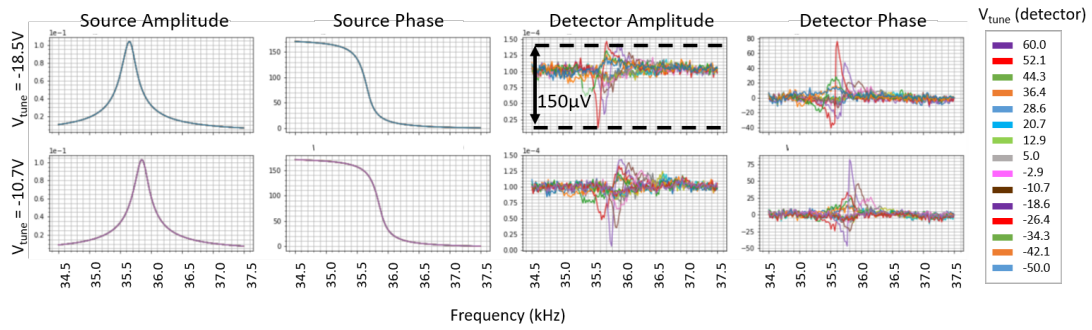
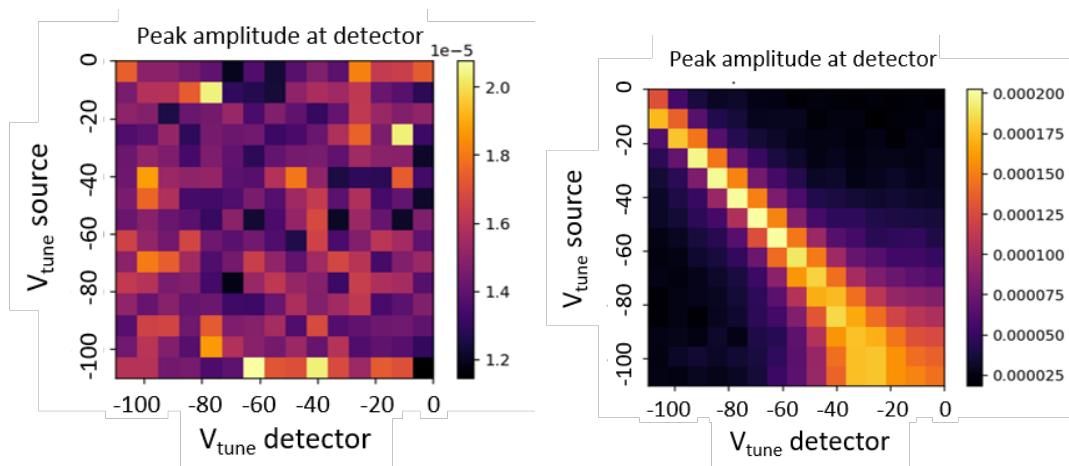


Figure 5.8: Excerpt of family of curves for N4P1 with acoustic cavity attached.



(a) Peak response for each tune voltage (b) Peak response for each tune voltage with acoustic cavity installed.

Figure 5.9: Heatmaps of N4P1 response.

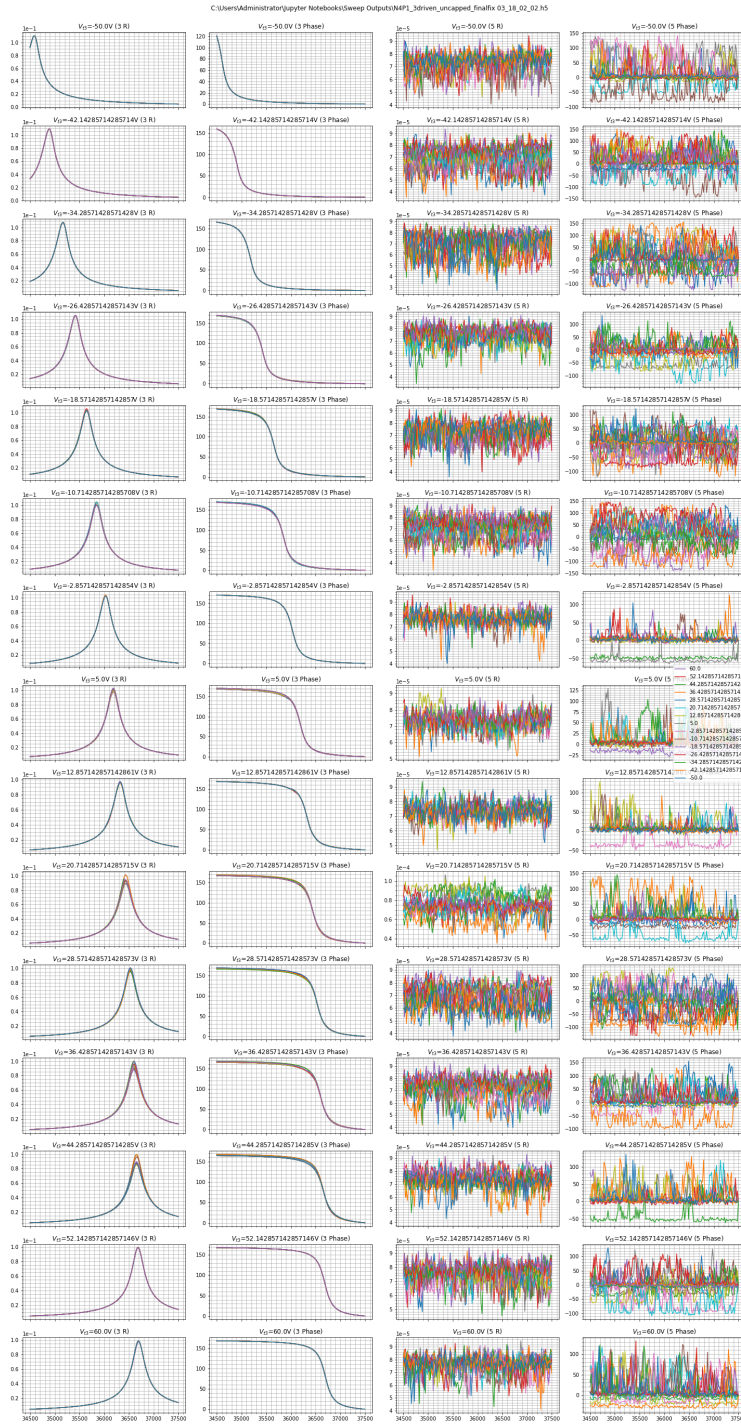


Figure 5.10: Family of curves showing full tuning range and uncapped response.

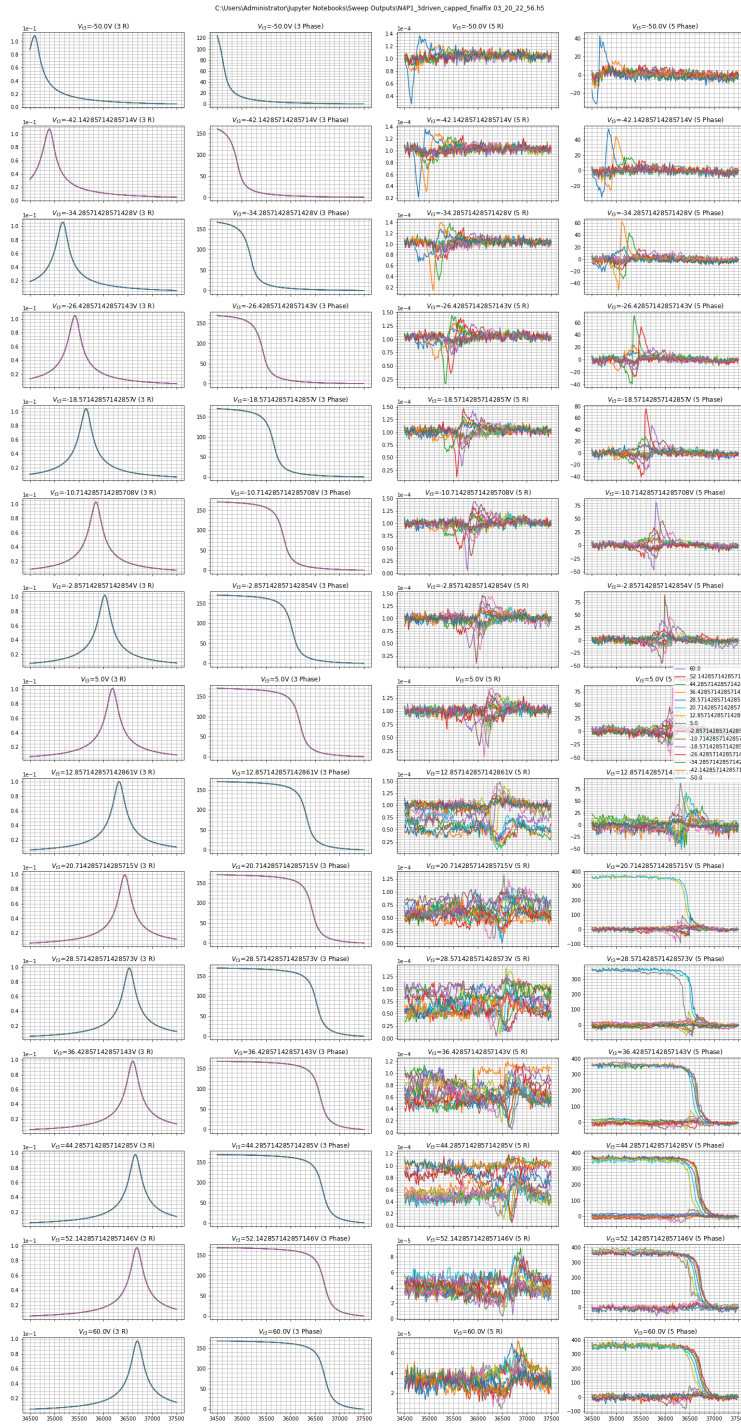


Figure 5.11: Family of curves showing full tuning range and capped response.

## 5.2 N1N1

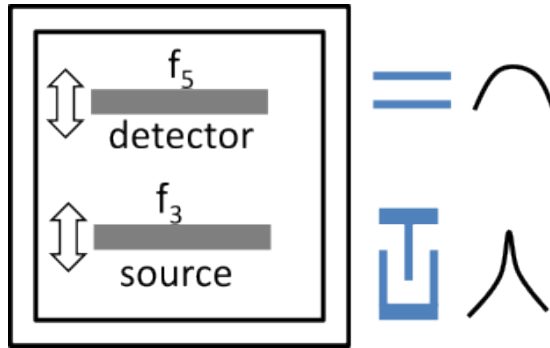


Figure 5.12: Diagram of N1N1 die showing the two resonator types.

N1N1 is the second die that is tested in this thesis. For this device,  $V_{pm} = 45V$  is set based on the encountered leakage currents during testing. Using the same testing procedure as N4P1, resonators 3 and 5 are selected as a pair for testing. In Figure 5.13, the tuning curve of the source resonator is shown. Only resonator 3 is measured in order to select an appropriate cavity. Using the tuning curve, a cavity size of 3.9 mm is selected to place the acoustic resonance frequency around 44200 Hz. Unlike N4P1, this die is of the parallel plate type. As shown qualitatively in Figure 5.12, the parallel plate based resonators have a lower quality factor compared to the comb drive based resonators due to the different electrode geometry. This is a desirable feature in the detector electrodes, easing the requirement to tune both resonators to the same frequency. With this die, the family of curves experiment is applied only for the acoustic cavity test, and the full data for this experiment is also given in Appendix 5.19. For the no acoustic cavity case shown in Figure 5.14, the experiment is run manually since not as many data points are deemed necessary. Figure 5.15 shows an excerpt of the family of curves for the acoustic cavity attached case, which is considered more important. The increased sensitivity of the parallel plate transducers, as well as an increase in amplifier gain added to both channels, means that some coupling is now observed even with no cavity attached. This coupling can be attributed to mechanical feedthrough from the substrate, as well as electrical feedthrough on the PCB; its magnitude was previously below the noise floor and it could thus

not be observed. When the acoustic cavity is added, the peak amplitude observed through the tuning range increases from approximately  $150\mu\text{V}$  to  $1.8\text{mV}$ .

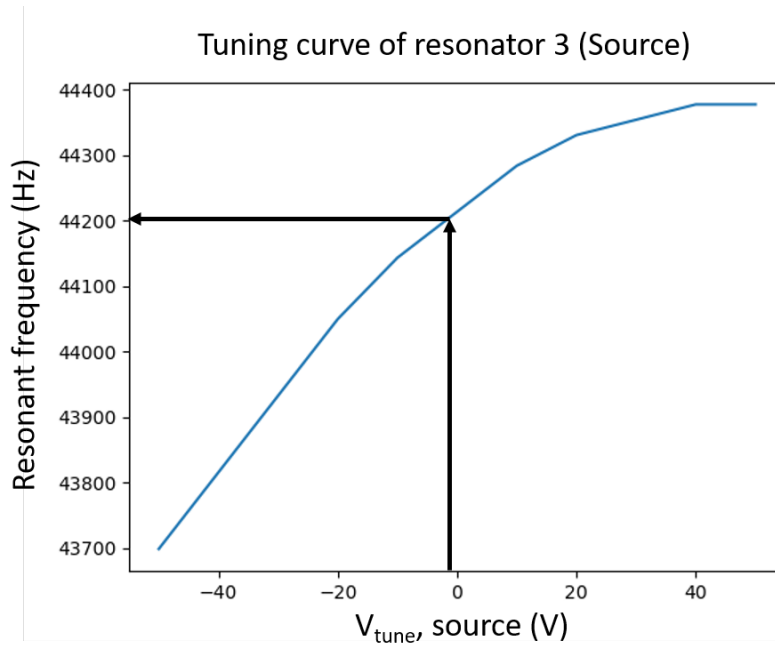


Figure 5.13: Tuning curve of N1N1’s source transducer showing cavity selection.

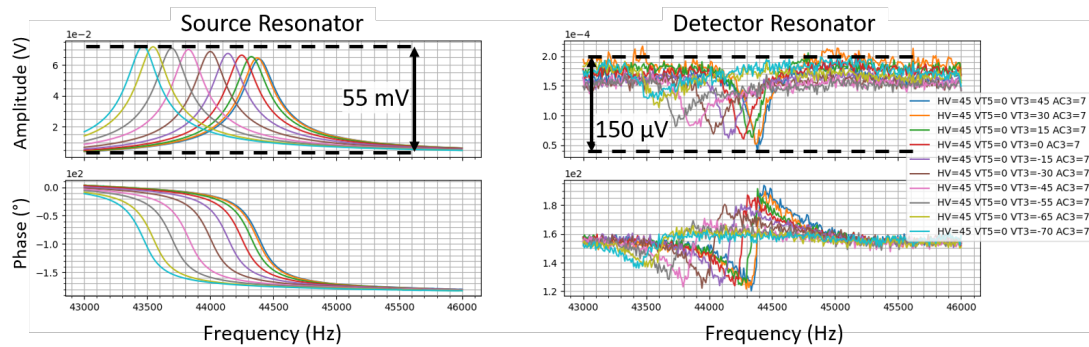


Figure 5.14: Excerpt of measured response with no acoustic cavity.

Based on the family of curves obtained from N1N1, it is also possible to infer the tuning curves of both resonators without testing them individually. For each resonator, this is achieved by looking at either each row or each column of the data and finding the frequency where the strongest peak is achieved within that row or column. These calculated tuning curves are given in Figure 5.16. It can be seen that the source resonator matches the manually measured tuning curve,

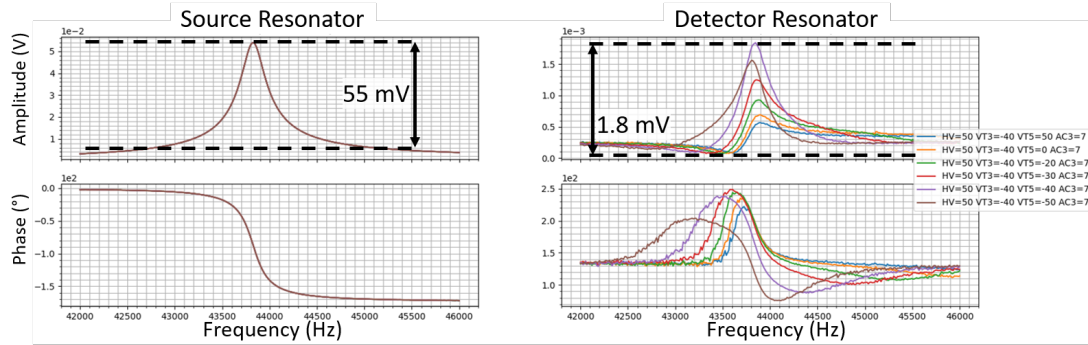


Figure 5.15: Excerpt of measured response with acoustic cavity.

while for the detector the wider tuning range of the parallel plate electrodes are made apparent, verifying the theoretical calculations in Section 2.2.4.

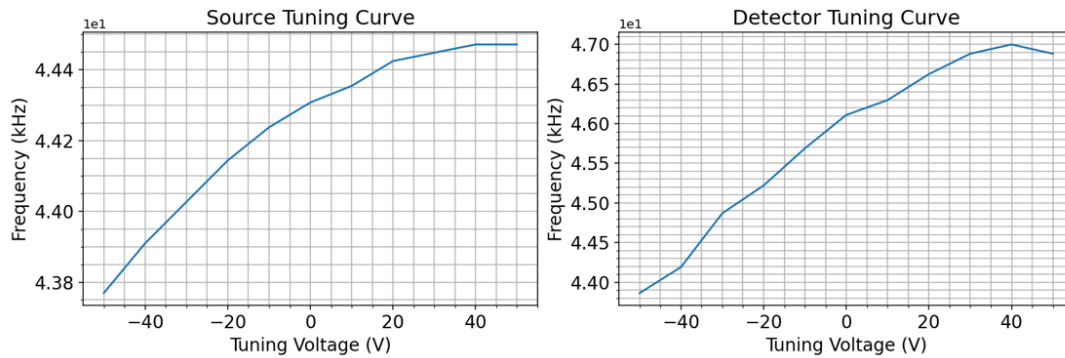


Figure 5.16: Inferred tuning curves for both resonators within N1N1.

Using the family of curves, a heatmap of the peak detector amplitude for each sweep point is drawn again. This heatmap is shown in 5.17. The slope of the diagonal line here shows a similar result to the inferred tuning curves: the detector's tuning is much more sensitive, so a small change in applied voltage is enough to track the source tuning.

A more important result that can be derived from the diagonal line is an estimate of the acoustic frequency response. This is extracted by looking at each row of the heatmap and recording the peak amplitude encountered within that row (doing this column-wise is also possible). Then, the amplitudes are divided by the peak source amplitude, in order to compensate for changes in its Q through the tuning range (based on Equation 2.5). The result is shown in

Figure 5.18. The center frequency for the cavity is determined as 43.8 kHz. For the previously set cavity length of 3.9 mm, 2.1 can be used to calculate  $c_{gas}$ . The speed of sound is determined using this method to be approximately 341m/s. With the Arduino based setup shown in Figure 4.13, the speed of sound was measured during this test as 343m/s. Even taking into account the uncertainty of the external measurement, this shows that the speed of sound can be measured accurately with this sensor. In addition, the acoustic cavity quality factor can also be measured. The 3 dB point is found from the graph as 44.0 kHz, giving a 3 dB bandwidth of 400 Hz. Based on this, the quality factor is measured as  $43800/400 = 109.5$ .

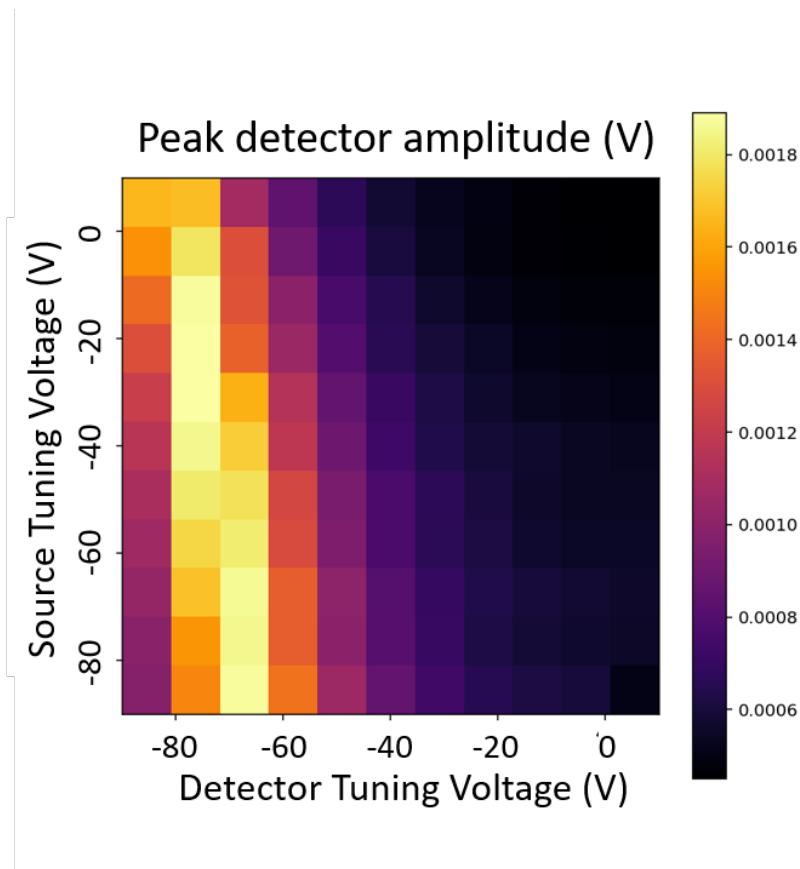


Figure 5.17: Heatmap of peak detector amplitudes within N1N1.

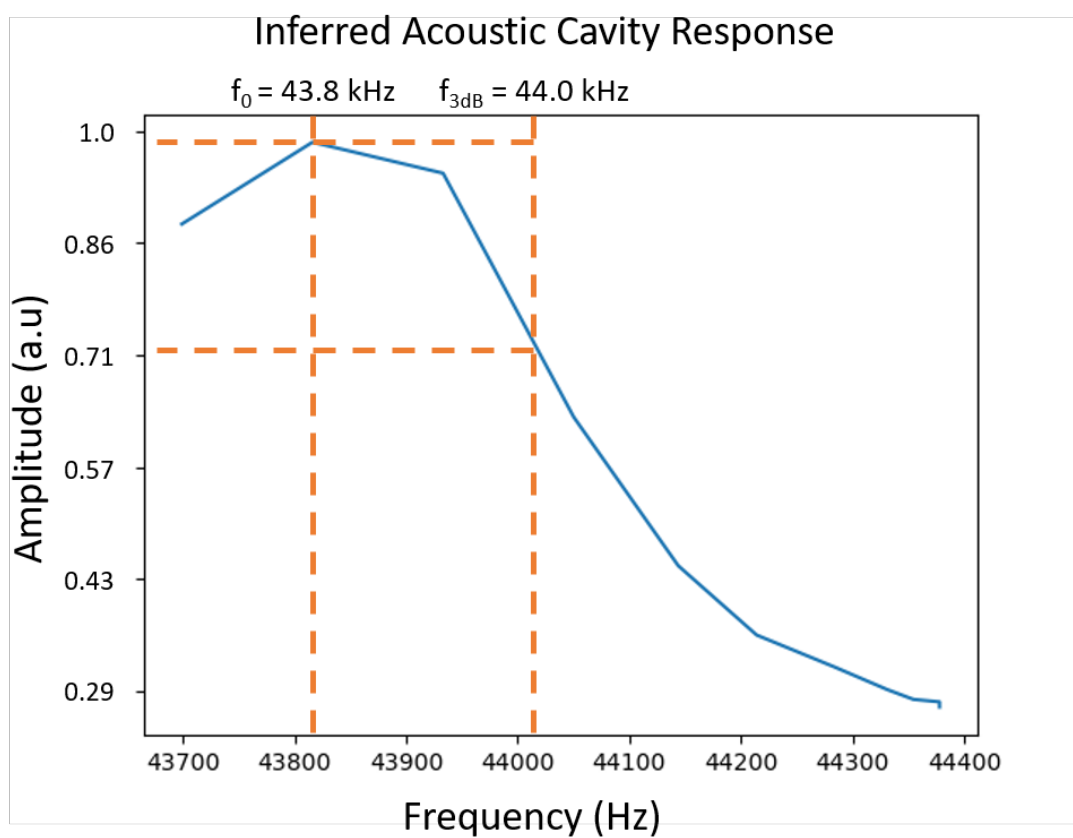


Figure 5.18: Inferred acoustic cavity frequency response based on N1N1 response.

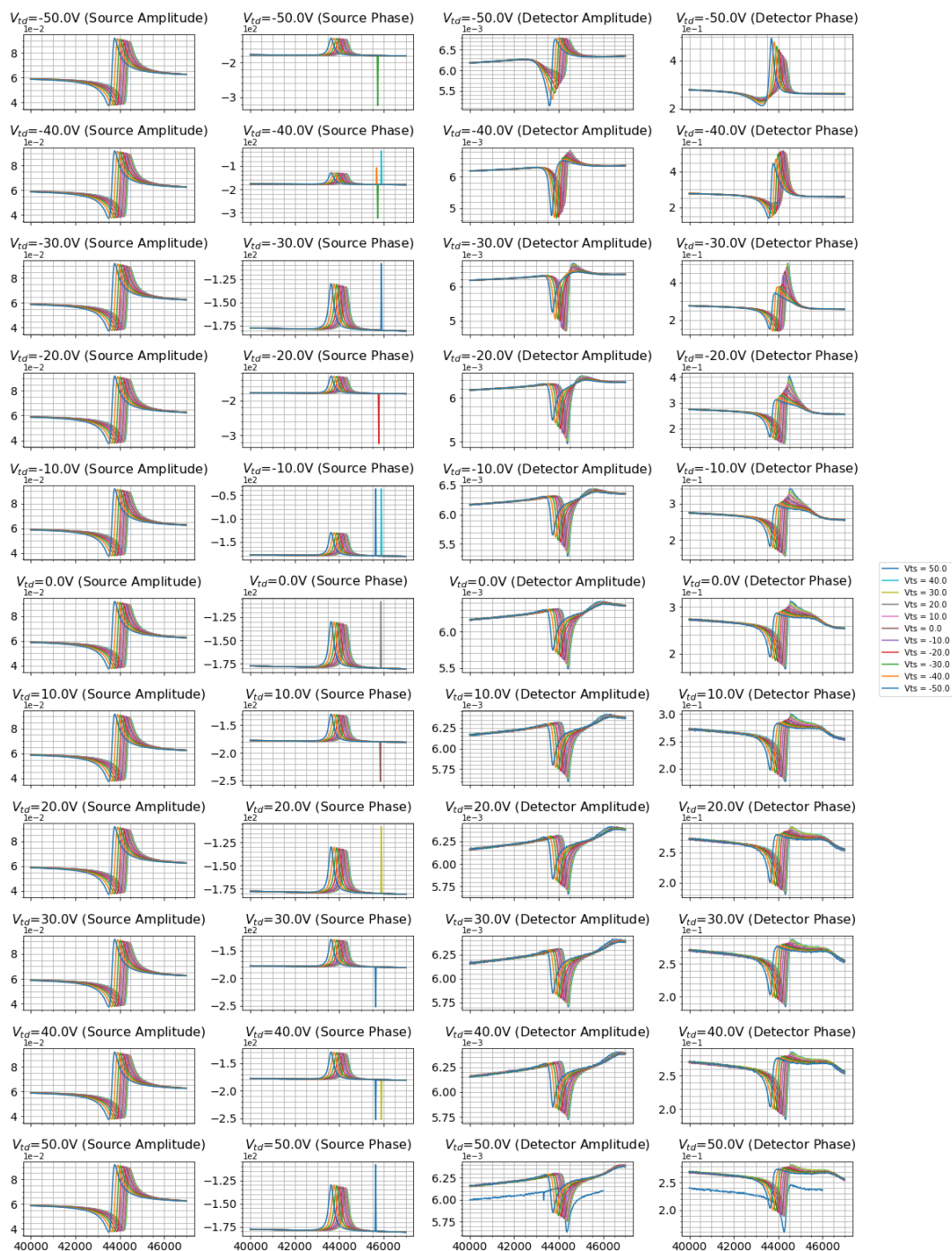


Figure 5.19: Family of curves showing full tuning range and capped response.

## 5.3 Conclusion

In conclusion, the proposed sensor is successfully fabricated using the developed recipe and the conducted tests reveal that the proof of concept devices are able to measure the speed of sound of the gas in the acoustic cavity. The results indicate that the concept of weak acoustic coupling into and out of the cavity is viable, and that there are no significant mechanical feedthrough effects through the substrate that can cause erroneous readings. Only the electrical feedthrough affects the result in a significant manner, however it is trivial to compensate the measurements to remove this effect. The potential of parallel plate based actuators are demonstrated by increased measurement SNR (electrical noise is constant, however mechanical amplitude increases significantly), and using this sensor die the frequency response of the acoustic cavity can be determined. Finally, using the parallel plate sensor die, a successful measurement of the speed of sound within the medium, and the quality factor of the acoustic resonance have been measured. In theory, this is sufficient to identify other gas types with sufficient calibration.

## 5.4 Future Work

In this work, a proof of concept MEMS gas sensor is demonstrated, however in the future the next logical step is to demonstrate actual gas detection. This can be accomplished by placing the complete PCB and sensor into a test chamber, where constituent gases can be introduced at controlled flow rates. By this method, the gas mixture inside the chamber can be precisely adjusted, allowing for measurements of each gas mixture to be made. An important detail in this procedure is that in order to simplify the construction of the test chamber, only gases such as oxygen, nitrogen or carbon dioxide, which are encountered in air, should be used. The current extent of the available equipment means that it is impractical to test with other gases which may pose a safety hazard, although

in theory it is possible to detect these gases as well. Water vapor can also be introduced with a separate controller to test the humidity response of the sensor.

Although the current process of characterizing the sensor system using frequency sweeps provides a definitive measure of the cavity response, it is also slow and impractical for measuring changing gas content. An entire family of curves is obtained typically in the span of multiple hours in order to get an accurate measurement. In order to improve the speed of the measurement, an algorithm can be written to constantly stay near the resonant peak and track the resonance in real time. For such an algorithm, the two PLLs available within the HF2LI can be used to track the peak of the two resonators, while the tuning voltages are manipulated with an external algorithm to track the acoustic cavity resonance. In addition, the sensitivity of the result can be further improved by not just looking at the sense amplitude, but also comparing the drive pick-off amplitude. In theory, the ratio between these two amplitudes is equal to the coupling coefficients between resonator and cavity multiplied by the cavity response, which is the desired parameter that is measured.

As described in Section 1.4, the measurement of the acoustic cavity's quality factor is also another aspect of this sensor design that can be investigated further to improve the sensor's accuracy. When only the resonant frequency is measured, the estimate of the gas content is made with only one independent variable. This means that there can exist mixtures of more than 2 gases where multiple different blends will result in the same  $c_{gas}$ , making it difficult to distinguish between them. By adding the quality factor as another independent variable, the accuracy of any estimation algorithm can be improved.

One potential source of error in the gas measurement process is the temperature dependence of  $c_{gas}$ . Currently, the daughterboard PCB includes a heater resistance and a footprint to solder in a temperature sensor. Using the temperature sensor, either closed loop control of the die temperature can be attempted, or an external calibration of the sensor against changing temperature can be implemented. Another potential solution that can be explored is to place two gas sensors onto the same package, where one sensor is hermetically sealed with a

known gas inside the cavity. This way, both cavities will be affected identically by temperature, and the resonant frequency of the hermetically sealed cavity can be used as a data point to calibrate the sensing cavity.

# Bibliography

- [1] M. R. Moldover, J. B. Mehl, and M. Greenspan, “Gas-filled spherical resonators: Theory and experiment,” *The Journal of the Acoustical Society of America*, vol. 79, pp. 253–272, 2 1986.
- [2] P. J. Koppinen, T. Sillanpaa, A. Karkkainen, J. Saarilahti, and H. Seppa, “A novel MEMS gas sensor based on ultrasonic resonance cavity,” in *2014 IEEE International Ultrasonics Symposium*, pp. 655–658, IEEE, 9 2014.
- [3] H. Davy, “I. On the fire-damp of coal mines, and on methods of lighting the mines so as to prevent its explosion,” *Philosophical Transactions of the Royal Society of London*, vol. 106, pp. 1–22, 12 1816.
- [4] A. Pastor-Fernández, A. Cerezo-Narváez, P. Montero-Gutiérrez, P. Ballesteros-Pérez, and M. Otero-Mateo, “Use of Low-Cost Devices for the Control and Monitoring of CO<sub>2</sub> Concentration in Existing Buildings after the COVID Era,” *Applied Sciences*, vol. 12, p. 3927, 4 2022.
- [5] R. Bogue, “Detecting gases with light: a review of optical gas sensor technologies,” *Sensor Review*, vol. 35, pp. 133–140, 3 2015.
- [6] H. Liu, Y. Shi, and T. Wang, “Design of a six-gas NDIR gas sensor using an integrated optical gas chamber,” *Optics Express*, vol. 28, p. 11451, 4 2020.
- [7] N. Yamazoe and K. Shimano, “New perspectives of gas sensor technology,” *Sensors and Actuators B: Chemical*, vol. 138, pp. 100–107, 4 2009.

- [8] U. Guth and J. Zosel, “Electrochemical solid electrolyte gas sensors — hydrocarbon and NO<sub>x</sub> analysis in exhaust gases,” *Ionics*, vol. 10, pp. 366–377, 9 2004.
- [9] K. Kaneyasu, K. Otsuka, Y. Setoguchi, S. Sonoda, T. Nakahara, I. Aso, and N. Nakagaichi, “A carbon dioxide gas sensor based on solid electrolyte for air quality control,” *Sensors and Actuators B: Chemical*, vol. 66, pp. 56–58, 7 2000.
- [10] B. Wang, X.-S. Dong, Z. Wang, Y.-F. Wang, and Z.-Y. Hou, “MEMS-Based Ionization Gas Sensors for VOCs with Array of Nanostructured Silicon Needles,” *ACS Sensors*, vol. 5, pp. 994–1001, 4 2020.
- [11] T.-J. Hsueh and S.-S. Wu, “Highly sensitive Co<sub>3</sub>O<sub>4</sub> nanoparticles/MEMS NO<sub>2</sub> gas sensor with the adsorption of the Au nanoparticles,” *Sensors and Actuators B: Chemical*, vol. 329, p. 129201, 2 2021.
- [12] B.-J. Kim and J.-S. Kim, “Gas sensing characteristics of MEMS gas sensor arrays in binary mixed-gas system,” *Materials Chemistry and Physics*, vol. 138, pp. 366–374, 2 2013.
- [13] K. Gillis and M. Moldover, *Experimental Thermodynamics Vol.IX: Advances in transport properties of fluids*. 2014.
- [14] J. Wilhelm, “An Improved Greenspan Acoustic Viscometer,” *International Journal of Thermophysics*, vol. 21, no. 5, pp. 983–997, 2000.
- [15] K. A. Gillis, J. B. Mehl, and M. R. Moldover, “Theory of the Greenspan viscometer,” *The Journal of the Acoustical Society of America*, vol. 114, pp. 166–173, 7 2003.
- [16] J. J. Hurly, K. A. Gillis, J. B. Mehl, and M. R. Moldover, “The Viscosity of Seven Gases Measured with a Greenspan Viscometer,” *International Journal of Thermophysics*, vol. 24, pp. 1441–1474, 11 2003.
- [17] N. Jaber, S. Ilyas, O. Shekhah, M. Eddaoudi, and M. I. Younis, “Resonant Gas Sensor and Switch Operating in Air With Metal-Organic Frameworks

- Coating,” *Journal of Microelectromechanical Systems*, vol. 27, pp. 156–163, 4 2018.
- [18] H. M. Ouakad, “The response of a micro-electro-mechanical system (MEMS) cantilever-paddle gas sensor to mechanical shock loads,” *Journal of Vibration and Control*, vol. 21, pp. 2739–2754, 10 2015.
- [19] A. H. Nayfeh, H. M. Ouakad, F. Najjar, S. Choura, and E. M. Abdel-Rahman, “Nonlinear dynamics of a resonant gas sensor,” *Nonlinear Dynamics*, vol. 59, pp. 607–618, 3 2010.
- [20] M. Yue, H. Lin, D. Dedrick, S. Satyanarayana, A. Majumdar, A. Bedekar, J. Jenkins, and S. Sundaram, “A 2-D Microcantilever Array for Multiplexed Biomolecular Analysis,” *Journal of Microelectromechanical Systems*, vol. 13, pp. 290–299, 4 2004.
- [21] J. Saarilahti, M. Blomberg, A. Haard, and H. Kattelus, “A novel method for processing capacitive micromechanical ultrasonic transducers (cMUT),” in *2002 IEEE Ultrasonics Symposium, 2002. Proceedings.*, pp. 1071–1074, IEEE.
- [22] I. Ladabaum, Xuecheng Jin, H. Soh, A. Atalar, and B. Khuri-Yakub, “Surface micromachined capacitive ultrasonic transducers,” *IEEE Transactions on Ultrasonics, Ferroelectrics and Frequency Control*, vol. 45, pp. 678–690, 5 1998.
- [23] A. Rona, “The Acoustic Resonance of Rectangular and Cylindrical Cavities,” *Journal of Algorithms & Computational Technology*, vol. 1, pp. 329–356, 10 2007.
- [24] J. Hilsenrath, W. S. Benedict, L. Fano, H. J. Hoge, J. F. masa, R. L. Nuttall, Y. S. Touloukian, and H. W. Woolley, “Circular of the Bureau of Standards no. 564,” tech. rep., National Bureau of Standards, Gaithersburg, MD, 1955.
- [25] Q. Li, J. Goosen, F. van Keulen, and J. van Beek, “Gas ambient dependence of quality factor in MEMS resonators,” in *2009 IEEE Sensors*, pp. 1040–1043, IEEE, 10 2009.

- [26] B. E. Uzunoglu, D. Erkan, and E. Tatar, “A Ring Gyroscope With On-Chip Capacitive Stress Compensation,” *Journal of Microelectromechanical Systems*, vol. 31, pp. 741–752, 10 2022.
- [27] J. E.-Y. Lee, J. Yan, and A. A. Seshia, “Study of lateral mode SOI-MEMS resonators for reduced anchor loss,” *Journal of Micromechanics and Microengineering*, vol. 21, p. 045010, 4 2011.
- [28] S. J. Kim, R. Dean, R. L. Jackson, and G. T. Flowers, “An investigation of the damping effects of various gas environments on a vibratory MEMS device,” *Tribology International*, vol. 44, pp. 125–133, 2 2011.
- [29] C. Liu, J. Froemel, J. Chen, T. Tsukamoto, and S. Tanaka, “Laterally vibrating MEMS resonant vacuum sensor based on cavity-SOI process for evaluation of wide range of sealed cavity pressure,” *Microsystem Technologies*, vol. 25, pp. 487–497, 2 2019.
- [30] S. Shmulevich, I. Hotzen, and D. Elata, “A perfect electrostatic anti-spring,” in *2013 IEEE SENSORS*, pp. 1–4, IEEE, 11 2013.
- [31] K. Williams, K. Gupta, and M. Wasilik, “Etch rates for micromachining processing-part II,” *Journal of Microelectromechanical Systems*, vol. 12, pp. 761–778, 12 2003.
- [32] “AZ 4500 Series Thick Film Photoresists,” 3 2021.
- [33] A. Bagolini, P. Scauso, S. Sanguinetti, and P. Bellutti, “Silicon Deep Reactive Ion Etching with aluminum hard mask,” *Materials Research Express*, vol. 6, p. 085913, 5 2019.
- [34] “OPAx322x 20-MHz, Low-Noise, 1.8-V, RRI/O, CMOS Operational Amplifier With Shutdown,” 2016.

# Appendix A

## DRIE Process Parameters

Table A.1: Process parameters used in the DRIE processing step

Parameter	Etch Cycle Value	Deposition Cycle Value
Cycle duration	12 seconds	10 seconds
Pressure	21 mTorr	12 mTorr
$SF_6$ flow rate	130 sccm	0 sccm
$O_2$ flow rate	13 sccm	0 sccm
$C_4F_8$ flow rate	0 sccm	85 sccm
Coil power (13.56 MHz)	600W	600W
Platen power (13.56 MHz)	12W	0W
Platen power (380 kHz)	35W at 50% duty cycle	0W
Platen temperature	15 °C	15 °C

# Appendix B

## Acoustic Cavity Resist Coating Procedure

1. Spin coat HMDS at 3000 rpm for 60 seconds
2. Spin coat Microchemicals AZ 4533 photoresist at 3000 rpm for 60 seconds
3. Soft bake for 60 seconds at 80 °C
4. Spin coat AZ 4533 at 3000 rpm for 60 seconds
5. Air dry for 15 minutes
6. Soft bake for 60 seconds at 110 °C

# Appendix C

## Family of Curves Code

```
%matplotlib widget
import zhinst.core
import time
import ipywidgets
import matplotlib.pyplot as plt
import numpy as np
import pyvisa
from ipyfilechooser import FileChooser
import h5py
import os
hostname = "localhost"
device = "dev1658"

daq = zhinst.core.ziDAQServer(hostname,8005,1)
daq.connectDevice(device, "usb")

rm = pyvisa.ResourceManager()
psu = rm.open_resource("GPIB0::6::INSTR")
smu = rm.open_resource("GPIB0::5::INSTR")

#Copied from API Log
sweeper = daq.sweep()
sweeper.set("device", "dev1658")
sweeper.set('historylength', 100)
sweeper.set('averaging/sample', 4)
sweeper.set('bandwidth', 10)
sweeper.set('omegasuppression', 40)
sweeper.set('order', 4)
sweeper.set('gridnode', '/dev1658/oscs/0/freq')
sweeper.set('save/directory', 'C:\\Users\\Administrator\\Documents\\Zurich_Instruments\\LabOne\\WebServer')
sweeper.set('averaging/tc', 0)
sweeper.set('averaging/time', 0.05)
sweeper.set('bandwidth', 10)
sweeper.set('settling/inaccuracy', 0.0001)
sweeper.set('start', 40000)
sweeper.set('stop', 50000)
sweeper.set('samplecount', 300)
sweeper.set('xmapping', 0)
sweeper.set('endless', 0)
sweeper.set('device', 'dev1658')
sweeper.subscribe('/dev1658/demods/0/sample')
sweeper.subscribe("/dev1658/demods/1/sample")
```

```

def setVoltage(chan, voltage):
    current_polarity = psu.query(f"outp:rel:pol?_{chan}").strip("\r\n")
    #print(current_polarity)

    if voltage >= 0 and current_polarity == "REV":
        psu.write(f"sour:volt_{chan}")
        time.sleep(0.2)
        psu.write(f"outp:rel:pol_norm,{chan}")
        time.sleep(0.2)

    if voltage < 0 and current_polarity == "NORM":
        psu.write(f"sour:volt_{chan}")
        time.sleep(0.2)
        psu.write(f"outp:rel:pol_rev,{chan}")
        time.sleep(0.2)

    psu.write(f"sour:volt_{abs(voltage)},{chan}")

def setTuneVoltage(vt3, vt5):
    setVoltage(1, vt5)
    setVoltage(4, vt3)

def readErrors(instrument):
    err = "99999"
    errors = list()
    while int(err.split(",")[0]) != 0:
        err = instrument.query("syst:err?")
        errors.append(err)
    return errors[-1] if len(errors) > 1 else None

def stop_all():
    psu.write("outp_off,{1,3,4}")
    smu.write("outp_off")
    daq.setInt('/dev1658/sigouts/0/on', 0)
    daq.setInt('/dev1658/sigouts/1/on', 0)

def tunePath(bounds_3, bounds_5, step_size):
    steps_3 = np.linspace(max(bounds_3), min(bounds_3), step_size)
    steps_5 = np.linspace(max(bounds_5), min(bounds_5), step_size)

    tune_path_3 = np.zeros(step_size**2)
    tune_path_5 = np.zeros(step_size**2)

    for i, vt3 in zip(range(step_size), steps_3):
        tune_path_3[i*step_size:(i+1)*step_size] = vt3
        if i % 2 == 0: #even
            tune_path_5[i*step_size:(i+1)*step_size] = steps_5
        else: #odd
            tune_path_5[i*step_size:(i+1)*step_size] = steps_5[:-1]
    return (tune_path_3, tune_path_5)

volt_3_slider = ipywidgets.IntRangeSlider(
    value = [-60, 70],
    min = -60,
    max = 70,
    step = 1,
    description = "Tune_3_voltage_range",
    orientation='horizontal',
    readout=True)

volt_5_slider = ipywidgets.IntRangeSlider(
    value = [-60, 70],
    min = -60,
    max = 70,
    step = 1,
    description = "Tune_5_voltage_range",
    orientation='horizontal',

```

```

        readout=True)

freq_slider = ipywidgets.IntRangeSlider(value=[40000,50000],min=25000,max=55000,step=50,description="Frequency_range_for_sweep",readout=True)
sweep_step_slider = ipywidgets.IntSlider(value=300,min=0,max=500,step=25,description="Zurich_step_size",readout=True)

step_size_slider = ipywidgets.IntSlider(value=21,min=1,max=50,step=1,description="Number_of_steps_in_each_dimension")

filename_text = ipywidgets.Text(value=time.strftime("%Y-%m-%d-%H-%M-%S.h5"),description="Filename:")

display(freq_slider)
display(sweep_step_slider)
display(volt_3_slider)
display(volt_5_slider)
display(step_size_slider)
display(filename_text)

path_3,path_5 = tunePath(volt_3_slider.value,volt_5_slider.value,step_size_slider.value)
demo_fig, demo_ax = plt.subplots()
demo_ax.plot(path_3,path_5,marker="o")
demo_ax.set_title(f"Start:_{path_3[0]},_{path_5[0]};_End:_{path_3[-1]},_{path_5[-1]}")

sweeper.set('start', freq_slider.value[0])
sweeper.set('stop', freq_slider.value[1])
sweeper.set("samplecount",sweep_step_slider.value)

sweep_progress_bar = ipywidgets.FloatProgress(value=0,min=0,max=1.0,description="Current_sweep_progress")
path_progress_bar = ipywidgets.IntProgress(value=0,min=0,max=len(path_3),description="Overall_progress")
hv_current_bar = ipywidgets.FloatProgress(value=0,min=0,max=1e-6,description="HV_current",readout=True)

display(sweep_progress_bar)
display(path_progress_bar)
display(hv_current_bar)

sweep_results = list()
start_time = time.perf_counter()

for i in range(len(path_3)):
    setTuneVoltage(path_3[i],path_5[i])
    time.sleep(5)
    current_acq = False
    while not current_acq:
        try:
            hv_current = float(smu.query("read?").split(",")[1])
            current_acq = True
        except pyvisa.errors.VisaIOError:
            print(readErrors(smu))
    if hv_current > 1e-6:
        stop_all()
        break
    hv_current_bar.value = hv_current
    sweeper.execute()
    while not sweeper.finished():
        sweep_progress_bar.value = sweeper.progress()
    path_progress_bar.value = i

    sweep_results.append([(path_3[i],path_5[i],50,hv_current),sweeper.read(flat=True)])

#Get the feedthrough as well
setTuneVoltage(0,0)
smu.write("sour:volt_0")
print("Taking_feedthrough_measurement...")
time.sleep(60) #Wait a minute for voltages to settle
sweeper.execute()
while not sweeper.finished():
    sweep_progress_bar.value = sweeper.progress()
sweep_results.append([(0,0,0,0),sweeper.read(flat=True)])

stop_time = time.perf_counter()

```

```

print(f"Elapsed_time: {stop_time-start_time}seconds")
smu.write("syst:beep:imm_440,2")

with h5py.File(os.path.join("Sweep_Outputs",filename_text.value + time.strftime("%m%d%H%M") + ".h5"), "w") as f:
    for i, idx in zip(sweep_results, range(len(sweep_results))):
        header = i[0]
        sample_0 = i[1]["/dev1658/demods/0/sample"][0][0]
        sample_1 = i[1]["/dev1658/demods/1/sample"][0][0]

        sweep_group = f.create_group(str(idx))
        sample_0_group = sweep_group.create_group("demod_0")
        sample_1_group = sweep_group.create_group("demod_1")

        sweep_group.attrs["demod_0_transducer"] = 3
        sweep_group.attrs["demod_1_transducer"] = 5
        sweep_group.attrs["vtune_0"] = header[0]
        sweep_group.attrs["vtune_1"] = header[1]
        sweep_group.attrs["hv_voltage"] = header[2]
        sweep_group.attrs["hv_current"] = header[3]
        sweep_group.attrs["saved_on"] = time.time()

    for key, value in sample_0.items():
        try:
            sample_0_group.create_dataset(key, data=value)
        except TypeError:
            if key != "header": print(f"{key}_was_not_saved")
    for key, value in sample_1.items():
        try:
            sample_1_group.create_dataset(key, data=value)
        except TypeError:
            if key != "header": print(f"{key}_was_not_saved")

```